The Dissertation Committee for Chunlou Li
certifies that this is the approved version of the following dissertation:

FINE SCALE SANDSTONE ACIDIZING COREFLOOD SIMULATION

Committee:

A. Daniel Hill, Supervisor

Ding Zhu

Larry W. Lake

William W. Rossen

Mary F. Wheeler

FINE SCALE SANDSTONE ACIDIZING COREFLOOD SIMULATION

by

Chunlou Li, B.S., M.S.

Dissertation

Presented to the Faculty of the Graduate School of

the University of Texas at Austin

in Partial Fulfillment

of the Requirements

for the Degree of

Doctor of Philosophy

The University of Texas at Austin

August, 2004

Dedication

To my parents, for their persistent love and spiritual support in my life.

Acknowledgements

First of all, I want to express my gratitude to Dr. Hill and Dr. Zhu for their invaluable guidance and support during my Ph.D study. I thank them for the patience and encouragement they showed to me from time to time. Being their student for three years, they always teach me the true attitude to research and how to work efficiently. That's an everlasting gift from them.

I also want to thank Dr. Lake for his good advices to my project and being my committee member. He also has taught me a lot about how to write a good thesis. That's really helpful. My sincere appreciation also goes to Dr. Rossen and Dr. Wheeler for being my committee members and taking time to read my thesis. Their suggestions are very valuable.

This project cannot finish so well without the help and cooperation from my fellow students, Tao Xie, Maysam Pournik, Kenji Furui, and Naga Potluri. That's a great experience working with them.

My special thanks extend to my husband, Hongbo, who always support me and encourage me. Without him and my two lovely boys, John and Henry, my effort will not be meaningful.

FINE SCALE SANDSTONE ACIDIZING COREFLOOD SIMULATION

Publication No. ______________

Chunlou Li, Ph.D.

The University of Texas at Austin, 2004

Supervisor: A. Daniel Hill

Contrary to the traditional understanding of matrix acidizing of sandstone that the acid front propagates in the formation with a piston-like style, some wormhole like structures were observed in lab tests under certain conditions. Most current models treat the rock as a homogeneous porous medium to describe the matrix acidizing in sandstone. The most sophisticated design models divide the formation into a series of layers with constant properties (minerals, permeability, etc.) in each layer. However, sandstones invariably have small – scale heterogeneities in minerals and flow properties that may cause the effects of injected acids to differ greatly from what is predicted by a model based on a homogeneous formation.

A fine-scale model of the sandstone core acid flooding is developed based on mass balance and the chemical reactions between acids and minerals that occur during sandstone acidizing. This mathematical model is numerically solved to predict the permeability response and demonstrate the distributions of acids, precipitates, flow velocity and porosity in the core during acidizing. Cores are divided into 8000 grid blocks to simulate the fine-scale structure of sandstone. Using standard geostatistical techniques at the beginning of simulations can generate heterogeneous porosity or/and minerals. The permeability response to acidizing is predicted using a model in which not only the porosity, but also the minerals, tortuosity, and statistical parameters of the particle size are considered.

Application of the new model to typical acidizing conditions shows that acid tends to channel through a heterogeneous sandstone, with the most efficient acidizing occurring when the rock has a layered structure. A layered structure is simulated by assuming a correlated permeability field in the main flow direction, as occurs in sandstones having horizontal laminations. The model shows that acid can stimulate the matrix permeability two to three times farther into the rock than would be predicted with a standard acidizing model, which takes the rock as homogeneous porous medium.

TABLE OF CONTENTS

LIST OF FIGURES XI

LIST OF TABLES XVIII

CHAPTER 1 INTRODUCTION 1

1.1 Matrix Acidizing in Sandstone 1
  1.1.1 Acid selection in sandstone matrix acidizing..1
  1.1.2 Wormhole generation in acidizing..2
  1.1.3 Fine scale simulation of sandstone acidizing..3

1.2 Objectives 4

CHAPTER 2 MATHEMATICAL MODEL FOR SANDSTONE MATRIX ACIDIZING 6

2.1 Mathematical Model Development...6
  2.1.1 Chemical reaction model 6
  2.1.2 Mass Conservation Equation for Acid Solution 7
  2.1.3 The Material Balance For Each Component In The Control Volume .10
  2.1.4 Initial and Boundary Conditions..16

2.2 Dimensionless Mathematical Model Development 17
  2.2.1 Dimensionless HF transport equation..17
  2.2.2 Dimensionless H_2SiF_6 balance equation..20
  2.2.3 Dimensionless mineral balance equations 21
  2.2.4 Dimensionless initial and boundary conditions 25

CHAPTER 3 NUMERICAL SOLUTION OF THE ACIDIZING MODEL 27

3.1 Gridding Method...27

3.2 Development of Finite Difference Form of Equations 27
  3.2.1 Finite Difference Form of Equation 2.12..27
  3.2.2 Finite Difference Form of Eq. 2.24...30

3.2.3 Finite Difference Form of Eq. 2.25 31
3.2.4 Finite Difference Form of Eq. 2.26 31
3.2.4 Initial and Boundary Conditions 32

3.3 Implementation 33
3.3.1 Calculation of Pressure Distribution 33
3.3.2 Calculation of HF Concentration Distribution 42
3.3.3 Calculation of H_2SiF_6 Concentration Distribution 46
3.3.4 Update of Permeability 46

CHAPTER 4 GENERATING HETEROGENEOUS INITIAL POROSITY AND MINERALS 49

4.1 Generation of Completely Random Porosity Field 50

4.2 Generation Of Correlated Porosity Distribution 55
4.2.1 Generation of Correlated Random Numbers 56
4.2.2 Converting Correlated Random number to correlated porosity distribution 58

4.3 Generation of Random Mineral Distribution 65

4.4 Generation of correlated mineral distribution 65

CHAPTER 5 RESULTS AND DISCUSSION 68

5.1 Influence of Heterogeneous and/or Correlated Distribution of Rock Properties 71
5.1.1 Homogeneous Porosity And Mineral Distribution 71
5.1.2 Heterogeneous Porosity And Homogeneous Minerals 78
5.1.3 Correlated Porosity Distribution And Homogeneous Mineral Distribution 88
5.1.4 Heterogeneous Mineral And Homogeneous Porosity 95
5.1.5 Correlated Mineral Distribution And Homogeneous Porosity Distribution 98
5.1.6 Heterogeneous Porosity and Minerals 103

5.2 Effect of Fast Reacting Mineral Content on Matrix Flow Pattern.............108

5.3 Effect of Acid Concentration on Matrix Flow Pattern...............................113

CHAPTER 6 SUMMARY AND CONCLUSIONS **116**

APPENDIX A THE INTERFACE PROGRAM **119**

A.1 Interface 119
    A.1.1 Core information...121
    A.1.2 Kinetic Parameters 121
    A.1.3 Simulation Parameters 122
    A.1.4 Porosity Distribution...123
    A.1.5 Mineral Distribution...124
    A.1.6 Mass Dissolving Power...124
    A.1.7 Mineral Information..125
    A.1.8 Commend Buttons..125

A.2 Output..125

A.3 3D Visualization of Simulation Results..126

APPENDIX B VALIDATION OF THE MODEL **127**

APPENDIX C NOMENCLATURE **131**

REFERENCES **134**

VITA **138**

LIST OF FIGURES

Figure 2.1: The control volume of the model. 8

Figure 3.1: The gridding method of a core. 28

Figure 3.2: Finite difference domain. 28

Figure 3.3: The general coefficient matrix to solve the pressure equation. 35

Figure 3.4: The vector of the RS to solve the pressure equation. 42

Figure 3.5: The vector of the RS to solve the pressure equation. 45

Figure 4.1: Histogram of porosity distributed (*N* is the number of grid blocks in each bin) (λ_x/L=0, λ_y/L=0, λ_z/L=0). 52

Figure 4.2: Semi-variogram of porosity distribution in the *x* direction (λ_x/L=0, λ_y/L=0, λ_z/L=0). 53

Figure 4.3: Semi-variogram of porosity distribution in the *y* direction (λ_x/L=0, λ_y/L=0, λ_z/L=0). 54

Figure 4.4: Semi-variogram of porosity distribution in the *z* direction (λ_x/L=0, λ_y/L=0, λ_z/L=0). 54

Figure 4.5: Completely random porosity distribution (λ_x/L=0, λ_y/L=0, λ_z/L=0). 55

Figure 4.6: Histogram of porosity distribution (λ_x/L=10, λ_y/L=0.025, λ_z/L=0.5). 60

Figure 4.7: Semi-variogram of porosity distribution in the *x* direction (λ_x/L=10, λ_y/L=0.025, λ_z/L=0.5). 61

Figure 4.8: Semi-variogram of porosity distribution in the *y* direction (λ_x/L=10, λ_y/L=0.025, λ_z/L=0.5)... 61

Figure 4.9: Semi-variogram of porosity distribution in the *z* direction (λ_x/L=10, λ_y/L=0.025, λ_z/L=0.5)... 62

Figure 4.10: Porosity distribution (λ_x/L=10, λ_y/L=0.025, λ_z/L=0.5)........................... 62

Figure 4.11: Porosity distribution (λ_x/L=10, λ_y/L=0.025, λ_z/L=0.025)....................... 64

Figure 4.12: Porosity distribution (λ_x/L=1, λ_y/L=0.025, λ_z/L=0.025)......................... 64

Figure 4.13: Histogram of the fast reacting mineral distribution (λ_x/L=0, λ_y/L=00, λ_z/L=00). 66

Figure 4.14: Fast reacting mineral distribution in a core (λ_x/L=0, λ_y/L=0, λ_z/L=0).... 66

Figure 4.15: Fast-reacting mineral distribution (λ_x/L=10, λ_y/L=0.025, λ_z/L=0.5). 67

Figure 5.1: Pressure response during acid core flooding in simulation. (PVbt is the pore volume at which acid breaks through).. 72

Figure 5.2: $\Delta\phi$ distribution for the homogeneous case after 5 PV of acid injection... 72

Figure 5.3: $\Delta\phi$ distribution for the homogeneous case after 15 PV of acid injection. 73

Figure 5.4: $\Delta\phi$distribution for the homogeneous case after 25 PV of acid injection. 73

Figure 5.5: $\Delta\phi$distribution for the homogeneous case after 35 PV of acid injection. 74

Figure 5.6: HF dimensionless concentration at 35 PV for the homogeneous case..... 75

Figure 5.7: Permeability distribution for the homogeneous case after 5 PV of acid injection... 76

Figure 5.8: Permeability distribution for the homogeneous case after 15 PV of acid injection... 76

Figure 5.9: Permeability distribution for the homogeneous case after 25 PV of acid injection... 77

Figure 5.10: Permeability distribution for the homogeneous case after 35 PV of acid injection... 77

Figure 5.11: Δϕ distribution (Δϕ>0.02) for heterogeneous porosity (σ=0.05) and homogeneous minerals case (5 PV)... 79

Figure 5.12: Δϕ distribution (Δϕ>0.02) for heterogeneous porosity (σ=0.05) and homogeneous minerals case (15 PV)... 79

Figure 5.13: Δϕ distribution (Δϕ>0.02) for heterogeneous porosity (σ=0.05) and homogeneous minerals case (25 PV)... 80

Figure 5.14: Δϕ distribution (Δϕ>0.02) for heterogeneous porosity (σ=0.05) and homogeneous minerals case (35 PV)... 80

Figure 5.15: Δϕ distribution (without cutoff) for heterogeneous porosity (σ=0.05) and homogeneous minerals case (15 PV)... 81

Figure 5.16: Dimensionless HF concentration distribution for heterogeneous porosity (σ=0.05) and homogeneous minerals case (5 PV).. 81

Figure 5.17: Dimensionless HF concentration distribution for heterogeneous porosity (σ=0.05) and homogeneous minerals case (15 PV).. 82

Figure 5.18: Dimensionless HF concentration distribution for heterogeneous porosity (σ=0.05) and homogeneous minerals case (25 PV).. 82

Figure 5.19: Dimensionless HF concentration distribution for heterogeneous porosity (σ=0.05) and homogeneous minerals case (35 PV). 83

Figure 5.20: Distribution of dimensionless concentration of fast reacting mineral after 15 PV of acid injection. (σ=0.01). 84

Figure 5.21: Distribution of dimensionless concentration of fast reacting mineral after 15 PV of acid injection. (σ=0.03). 84

Figure 5.22: Distribution of dimensionless concentration of fast reacting mineral after 15 PV of acid injection. (σ=0.05). 85

Figure 5.23: Distribution of dimensionless concentration of fast reacting mineral after 15 PV of acid injection. (σ=0.07). 85

Figure 5.24: Dimensionless velocity distribution (higher than 4) of acid in the core after 35-PV of acid injection (σ=0.05). 86

Figure 5.25: Permeability evolution for random porosity cases and homogeneous porosity case 87

Figure 5.26: Acid breakthrough volume for random porosity cases and homogeneous porosity case 88

Figure 5.27: Initial porosity distribution in a core. (Case 6: λ_x/L=10, λ_y/L=0.025, λ_z/L=0.5). 89

Figure 5.28: Initial porosity distribution in a core. (Case 9: λ_x/L=1, λ_y/L=0.025, λ_z/L=0.5). 90

Figure 5.29: Permeability evolution for correlated porosity cases and completely random porosity case. 92

Figure 5.30: Acid breakthrough volume for correlated porosity cases....................... 92

Figure 5.31: $\Delta\phi$ for correlated porosity case after 5 PV of acid injection in Case 6 ($\Delta\phi$>0.02) (λ_x/L=10, λ_y/L=0.025, λ_z/L=0.5).. 93

Figure 5.32: $\Delta\phi$ for correlated porosity case after 15 PV of acid injection in Case 6 ($\Delta\phi$>0.02) (λ_x/L=10, λ_y/L=0.025, λ_z/L=0.5).. 93

Figure 5.33: $\Delta\phi$ for correlated porosity case after 25 PV of acid injection in Case 6 ($\Delta\phi$>0.02) (λ_x/L=10, λ_y/L=0.025, λ_z/L=0.5).. 94

Figure 5.34: $\Delta\phi$ for correlated porosity case after 35 PV of acid injection in Case 6 ($\Delta\phi$>0.02) (λ_x/L=10, λ_y/L=0.025, λ_z/L=0.5).. 94

Figure 5.35: Permeability distribution after 5 PV of acid injection (λ_x/L=10, λ_y/L=0.025, λ_z/L=0.5)... 95

Figure 5.36: Initial distribution of fast reacting mineral (volume fraction). (Average: 0.04) 96

Figure 5.37: HF concentration (>0.1) distribution after 5 PV of acid injection. 97

Figure 5.38: HF concentration (>0.1) after 25 PV of acid injection.......................... 97

Figure 5.39: Dimensionless velocity distribution (>1.5) after 5 PV of acid injection.98

Figure 5.40: Initial fast reacting mineral distribution (λ_x/L=10, λ_y/L=0.025, λ_z/L=0.5). 100

Figure 5.41: Permeability distribution after 5 PV of acid injection (λ_x/L=10, λ_y/L=0.025, λ_z/L=0.5)... 100

Figure 5.42: Permeability distribution after 35 PV of acid injection (λ_x/L=10, λ_y/L=0.025, λ_z/L=0.5).. 101

Figure 5.43: Precipitate distribution after 5 PV of acid injection............................ 101

Figure 5.44: Precipitate distribution after 35 PV of acid injection.......................... 102

Figure 5.45: Pressure response to acidizing for the correlated porosity case and the correlated minerals case... 103

Figure 5.46: Dimensionless HF concentration distribution (5PV). 104

Figure 5.47: Dimensionless HF concentration distribution (15PV). 104

Figure 5.48: Dimensionless HF concentration distribution (25PV). 105

Figure 5.49: Dimensionless HF concentration distribution (35PV). 105

Figure 5.50: Dimensionless velocity distribution (5PV). 106

Figure 5.51: Dimensionless velocity distribution (15PV). 107

Figure 5.52: Dimensionless velocity distribution (25PV). 107

Figure 5.53: Dimensionless velocity distribution (35PV). 108

Figure 5.54: Porosity (ϕ>0.08) distribution (5 PV). 109

Figure 5.55: Porosity (ϕ>0.08) distribution (15 PV). 110

Figure 5.56: Porosity (ϕ>0.08) distribution (25 PV). 110

Figure 5.57: Porosity (ϕ>0.08) distribution (35 PV). 111

Figure 5.58: Permeability distribution (5 PV). 111

Figure 5.59: Permeability distribution (15 PV). 112

Figure 5.60: Permeability distribution (25 PV). 112

Figure 5.61: Permeability distribution (35 PV). 113

Figure 5.62: Pressure drop response during core acid flooding................................ 114

Figure 5.63: HF distribution after 5 PV of acid injection. 115

Figure A.1: The input panel of the simulator... 120

Figure B.1: Differential pressure plot of core 1122 during treatment with 12wt% HCl – 3 wt% HF 128

Figure B.2: Pressure response during simulation of core 1122 test.......................... 129

Figure B.3: Permeability distribution after 3 PV of acid injection. 130

Figure B.4: Permeability (>350md) distribution after 3 PV of acid injection. 130

LIST OF TABLES

Table 4.1: Input parameters for generating a correlated porosity field....................... 59

Table 5.1: Parameters used in simulation 69

Table 5.2: Summary of simulation cases 70

Table B.1: Parameters for coreflood test of core 1122 127

CHAPTER 1 INTRODUCTION

1.1 Matrix Acidizing in Sandstone

Matrix acidizing is a stimulation method commonly used to remove near well bore damage and restore original formation permeability. During acidizing, acid is injected into the reservoir under pressure below the fracture pressure to dissolve minerals present in the rock and increase permeability. Because of different mineral composition in carbonate and sandstone, different types of acid are used to treat these two kinds of reservoirs. Reactions in carbonate acidizing are usually simple and the techniques applied are relatively mature. However, since reactions occurring in sandstone acidizing are much more complicated, no uniform rule has been found to serve as the guideline for all sandstone acidizing. Numerous work has been done and considerable progress has been made in this area.

1.1.1 ACID SELECTION IN SANDSTONE MATRIX ACIDIZING

In sandstone acidizing, a mixture of HF and HCl is usually used to dissolve siliceous minerals like feldspar, clay, and quartz present in the porous media. Based on original formation permeability and mineral composition, McLeod presented a guideline for acid selection [McLeod, 1984]. Acid type and concentration are often selected according to this guideline.

Since the reaction rates between HF and minerals are proportional to the acid concentration, to prevent additional damage caused by precipitate and rock unconsolidation during acidizing treatment, small concentrations of HF was recommended by some study [Brannon et al., 1987], especially in weaker formation that is easy to unconsolidate. The use of HF/HCl at a weight ratio of 1/9 has been extensively applied in field operations to minimize precipitation during sandstone acidizing. Recently, some experimental studies found that the HCl/HF ratio is an important factor that affects the amount of precipitate and the overall stimulation efficiency [Thomas et al., 2002[a]]. Kalfayan and Metcalf conducted core acid flooding experiments using up to 9% wt. HF [Kalfayan and Metcalf, 2000]. The results suggest that flowing channels are created when a large concentration of HF (6% or higher) is used, resulting in greater permeability increase.

1.1.2 WORMHOLE GENERATION IN ACIDIZING

The acidizing in carbonate formations is different than in sandstones. In carbonate acidizing, HCl dissolves formation minerals around the pore space, and creates large flow paths, which are called wormholes, resulting in considerable acidizing efficiency increase. Schechter [1992] described the mechanism behind wormhole generation as follows:

> *"Wormholes form in a dissolution when the large pores grow at a rate substantially higher rate than the rate at which smaller pores grow, so that large pores receive an increasingly larger proportion of the dissolving fluid, eventually becoming wormholes. This occurs when the reactions are mass transfer limited or mixed kinetics prevails."*

Contrary to carbonate acidizing, reactions in sandstone acidizing are relatively slow and are surface reaction rate limited. Therefore it was usually thought that it is impossible to create wormholes in sandstone acidizing. In most models developed to simulate sandstone acidizing, it is assumed that the acid front moves uniformly like a piston. However, several authors reported wormhole-like structures in sandstone acidizing experiments. Wehunt et al. observed that acid channeling occurred at high temperature because of the heterogeneity of the cores [Wehunt et al., 1993]. Experimental observations show that the channel generation in sandstones is fundamentally different from wormhole formation in carbonates [Thomas et al., 2002]. Some heterogeneity in matrix properties is required for any channeling behavior to be predicted by the standard models of the sandstone acidizing. If the acid is channeling through the matrix along high permeability pathways that then progressively increase in permeability in response to the dissolution of mineral particles along the pathway, it is possible for acid to penetrate much farther into a sandstone formation than is predicted by the usual models.

1.1.3 FINE SCALE SIMULATION OF SANDSTONE ACIDIZING

The current state of the art of sandstone acidizing modeling considers heterogeneities only in a very gross manner. The most sophisticated design models treat the formation as a series of layers with constant properties (minerals, permeability, etc.) in each layer. Radial variations in formation properties may be considered as a method of simulating the damaged region, but there is typically only two discrete regions considered – the damaged zone extending to some assumed radial distance, and the unaltered formation beyond this distance. However, sandstones invariably have small – scale heterogeneities in minerals and flow properties that may cause the effects of injected acids to differ greatly from what is predicted by a model based on a homogeneous formation.

Matrix acidizing of sandstone is thought to be influenced by very small- scale variations in the permeability field. Preferential flow of the acid through higher permeability pathways in the matrix allows much deeper acid penetration and better overall permeability response than is predicted by any current model of sandstone acidizing. This may be particularly important for high concentration HF treatments that are currently being applied, where channeling of the acid may create wormhole-like structures. In addition to variations in the permeability field, variations in the mineral distribution affect the stimulation achieved with acid. For example, sandstone containing clay-rich streaks may experience a large permeability increase as the clay is dissolved by acid.

1.2 Objectives

The objectives of this project are to develop a fine-scale three-dimension (3D) model for sandstone acid core flooding, to investigate the effect of local heterogeneity of rock properties on acid flowing pattern by generating heterogeneous original porosity and mineral distributions using standard geostatistic techniques, and to identify the dominant parameters that affect flow channel creation by simulation.

Chapter 2 demonstrates the development of the mathematical model for sandstone acidizing according to chemical reactions, an overall mass balance, and the mass balance of each component.

Chapter 3 first discusses the gridding method of the core. Then the mathematical model in finite difference form is developed, which is numerically solved to predict the overall permeability response and local distributions of acids, minerals, and porosity in the core during acidizing. The algorithm and implementation of the simulation is addressed as the last part of this chapter.

Chapter 4 covers the generation of initial porosity and mineral distributions using geostatistic techniques. Using different methods, both porosity and minerals can be initialized as completely random distribution or spatially correlated distribution with user specified correlation strength in different directions.

Chapter 5 summarizes the results of a series of simulation cases with various conditions. By graphically analyzing the results, some parameters are identified as the main factors that affect acid flowing patterns.

Chapter 6 summarizes the main points achieved in this project.

Appendix A serves as a help document of this numerical simulator. In Appendix A, the graphical user interface, the input files required, and the output files are introduced.

Appendix B validates this model by comparing the simulation results to the experiment results.

CHAPTER 2 MATHEMATICAL MODEL FOR SANDSTONE MATRIX ACIDIZING

Based on mass balances on acids, minerals, an overall mass balance, and Darcy's law, a three-dimensional numerical model was developed to describe the acid core flooding. To simplify the description of acidizing, the model is developed based on the following assumptions:

1. Single phase flow;
2. Only liquid phase and solid phase exist;
3. No sorption on solid phase
4. No dispersion;
5. Incompressible fluid and rock;
6. No gravity effects.

2.1 Mathematical Model Development

2.1.1 CHEMICAL REACTION MODEL

In former models, the reacting minerals are lumped into fast-reacting mineral and slow-reacting mineral [Schechter, 1992] according to their reaction rate. These models found broad application and gained great success in sandstone acidizing. However, these models become inadequate to describe the acid and mineral interactions under some conditions. A so-called two-acid three-mineral model was proposed to simulate sandstone acidizing at higher temperature [da Motta et al., 1992;

Bryant, 1991], which also took into account the precipitation of amorphous silica. It was found that the simulation results by this model agreed very well with Lindsay's experiments at high temperature [Lindsay, 1976].

The chemical reactions considered in this work are the same as the ones in the two-acid three-mineral acidizing model [da Motta et al., 1992; Bryant, 1991]. The reactions are:

ν_1 HF + mineral 1 → ν_5 H_2SiF_6 + fluorides of Al

ν_2 HF + mineral 2 → ν_6 H_2SiF_6 + fluorides of Al

ν_3 HF + mineral 3 → ν_7 H_2SiF_6 + fluorides of Al

ν_4 H_2SiF_6 + mineral 1 → ν_8 mineral 3 + fluorides of Al

Where the ν_i are the stoichiometric coefficients. Mineral 1 is a group of fast-reacting minerals, including feldspars, authogenic clays and amorphous silica; Mineral 2 is the slow-reacting mineral including detrital clay and quartz; and Mineral 3 is silica gel ($Si(OH)_4$). We assume the solubility product of silica gel, $K_{Si(OH)_4}^{SP}$, is zero, and fluorides of Al can completely dissolve in acid solution. We presume that an HCl preflush has already dissolved all carbonate minerals when HF is injected into the rock.

2.1.2 MASS CONSERVATION EQUATION FOR ACID SOLUTION

The control volume used to formulate the model is defined as the cubic volume shown in Figure 2.1. Acid solution is a mixture of acids and water. We assume that acid solution in sandstone acidizing obeys the mass conservation law. The mass balance equation for the acid solution is

$$\text{Acid in} - \text{Acid out} + \text{Source} = \text{Accumulation} \qquad (2.1)$$

It is assumed that there is no source of acid solution in cores during acid injection.

The mass of acid solution flowing into the control volume is

$$\Delta t\left(\left.(\rho u_x \Delta y \Delta z)\right|_x + \left.(\rho u_y \Delta x \Delta z)\right|_y + \left.(\rho u_z \Delta y \Delta x)\right|_z\right) \qquad (2.2)$$

where u_x, u_y, and u_z are the average Darcy velocities across the *y-z* plane, the *x-z* plane, and the *x-y* plane respectively, and ρ is the density of the acid solution.

The mass of acid solution flowing out of the control volume is

$$\Delta t\left(\left.(\rho u_x \Delta y \Delta z)\right|_{x+\Delta x} + \left.(\rho u_y \Delta x \Delta z)\right|_{y+\Delta y} + \left.(\rho u_z \Delta y \Delta x)\right|_{z+\Delta z}\right) \qquad (2.3)$$

Assuming the acid solution is the only phase in the pore space, the mass change in the control volume during time period Δt is

$$\Delta x \Delta y \Delta z\left((\rho\phi)^{t+\Delta t} - (\rho\phi)^{t}\right) \qquad (2.4)$$

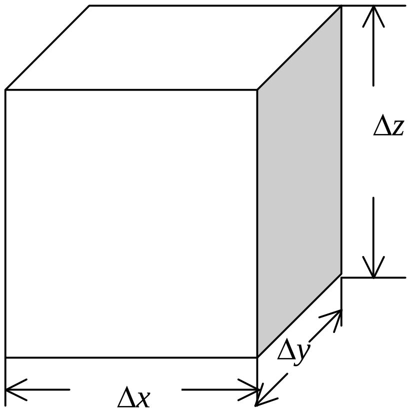

Figure 2.1: The control volume of the model.

Because there is no source in the control volume, the accumulation of the acid solution in the control volume equals the net inflow of the acid fluid. The mass conservation equation for the acid solution can be expressed as

$$\begin{aligned}\Delta x\Delta y\Delta z\left((\rho\phi)^{t+\Delta t}-(\rho\phi)^{t}\right)= \\ \Delta t\left((\rho u_x\Delta y\Delta z)\big|_x+(\rho u_y\Delta x\Delta z)\big|_y+(\rho u_z\Delta y\Delta x)\big|_z\right) \\ -\Delta t\left((\rho u_x\Delta y\Delta z)\big|_{x+\Delta x}+(\rho u_y\Delta x\Delta z)\big|_{y+\Delta y}+(\rho u_z\Delta y\Delta x)\big|_{z+\Delta z}\right)\end{aligned} \qquad (2.5)$$

Dividing Eq. 2.5 by $\Delta x\Delta y\Delta z\Delta t$, it becomes

$$\begin{aligned}\frac{(\rho\phi)^{t+\Delta t}-(\rho\phi)^{t}}{\Delta t}=\frac{(\rho u_x)_x-(\rho u_x)_{x+\Delta x}}{\Delta x}+\frac{(\rho u_y)_y-(\rho u_y)_{y+\Delta y}}{\Delta y} \\ +\frac{(\rho u_z)_z-(\rho u_z)_{z+\Delta z}}{\Delta z}\end{aligned} \qquad (2.6)$$

Taking the limits as Δx→0, Δy→0, Δz→0, and Δt→0, and ρ is constant because we assume acid solution is incompressible, Eq. 2.6 becomes

$$\frac{\partial\phi}{\partial t}=\frac{\partial u_x}{\partial x}+\frac{\partial u_y}{\partial y}+\frac{\partial u_z}{\partial z} \qquad (2.7)$$

It can be written as a vector as

$$\frac{\partial\phi}{\partial t}=\overline{\nabla}\cdot\overline{u} \qquad (2.8)$$

Where $\overline{u}$ = velocity vector $\{u_x, u_y, u_z\}$, defined as the Darcy velocity

$$\bar{u} = -\frac{\bar{\bar{k}}}{\mu} \cdot \left(\bar{\nabla} P + \gamma \bar{\nabla} z\right) \tag{2.9}$$

Where γ is gravity ratio. Ignoring gravity effects, Eq. 2.9 becomes

$$\bar{u} = -\frac{\bar{\bar{k}}}{\mu} \cdot \bar{\nabla} P \tag{2.10}$$

Substituting Eq. 2.10 into Eq. 2.8 yields

$$\frac{\partial \phi}{\partial t} = \bar{\nabla} \cdot \left(-\frac{\bar{\bar{k}}}{\mu} \cdot \bar{\nabla} P \right) = -\frac{1}{\mu}\frac{\partial}{\partial x}\left(k_x \frac{\partial P}{\partial x}\right) - \frac{1}{\mu}\frac{\partial}{\partial y}\left(k_y \frac{\partial P}{\partial y}\right) - \frac{1}{\mu}\frac{\partial}{\partial z}\left(k_z \frac{\partial P}{\partial z}\right) \tag{2.11}$$

Since porosity is treated as constant in each time step when the above equation is solved, the equation becomes

$$\frac{1}{\mu}\frac{\partial}{\partial x}\left(k_x \frac{\partial P}{\partial x}\right) + \frac{1}{\mu}\frac{\partial}{\partial y}\left(k_y \frac{\partial P}{\partial y}\right) + \frac{1}{\mu}\frac{\partial}{\partial z}\left(k_z \frac{\partial P}{\partial z}\right) = 0 \tag{2.12}$$

2.1.3 THE MATERIAL BALANCE FOR EACH COMPONENT IN THE CONTROL VOLUME

2.1.3.1 General Equation

The general equation to describe material balance is as the following [Lake, 1989]:

$$\frac{\partial W_i}{\partial t} + \bar{\nabla} \cdot \bar{N}_i = R_i \tag{2.13}$$

Where

$$W_i = \phi \sum_{j=1}^{N_p} \rho_j St_j \omega_{i,j} + (1-\phi)\rho_s \omega_{i,s} \tag{2.14}$$

$$\overline{N}_i = \sum_{j=1}^{N_p} u_j \rho_j \omega_{i,j} - \phi \sum St_j \rho_j \overline{\overline{k}}_{i,j} \cdot \overline{\nabla} \omega_{i,j} \tag{2.15}$$

W_i = Overall mass of component *i* in the control volume, [=] g_i/bulk vol;

$\omega_{i,j}$= Mass fraction of component *i* in phase *j*, [=] $g_i/g_{\text{phase j}}$

$\omega_{i,s}$=Mass fraction of component *i* in solid phase, [=] g_i/g_{solid};

ϕ = Porosity, [=] pore vol/bulk vol;

St_j = Saturation of phase *j*, [=] $\text{vol}_{\text{phase j}}$/pore vol;

ρ_j = Density of phase *j*, [=] $g_{\text{phase j}}/\text{vol}_{\text{phase j}}$;

ρ_s = Density of solid, [=] $g_{\text{solid}}/\text{vol}_{\text{solid}}$;

N_i = Flux of component *i*, [=] g_i/L^2-t;

u_j = Darcy velocity of phase *j*, [=] L/t;

$K_{i,j}$ = Dispersion coefficient of component *i* in phase *j*;

R_i = Sources of component *i*, [=] g_i/bulk vol-t.

i = Component index;

j = Phase index;

2.1.3.2 Material Balance for Acid Components

The first term on the right side of Eq. 2.14 represents the mass of component *i* in the liquid phase and the second term is the mass of component *i* in the solid phase. By assuming single-phase flow, both N_p and *St* equal to 1, and the subscript, *j*, can be dropped. Because of the assumption of no sorption on the solid phase, the second term on right side of Eq. 2.14 disappears. Then Eq. 2.14 is simplified to

$$W_i = \phi\rho\omega_i \tag{2.16}$$

In this particular problem, the mass of acid *i* in a control volume is expressed by its concentration, C_i. So $\rho\omega_i$ is replaced by C_i as the following

$$W_i = \phi C_i \tag{2.17}$$

Where

C_i = Concentration of acid *i*, [=] mol *i*/m^3 acid solution.

The first term on the right side of Eq. 2.15 represents the transport of component *i* by convection and the second term represents the transport of component *i* by dispersion. Compared to the spread of acid front caused by chemical reactions, the effects of dispersion can be ignored here. With the assumption of no dispersion, the second term of Eq. 2.15 drops off and this equation is simplified to

$$\overline{N}_i = \overline{u}\rho\omega_i \tag{2.18}$$

In this work, for mass balance of acid *i*, $\rho\omega_i$ is replaced by C_i. So Eq. 2.18 becomes

$$\overline{N}_i = \overline{u}C_i \tag{2.19}$$

For the mass balance of acid *i* in this work, the source term on the right side of Eq. 2.13 is the reaction rate of acid *i*. After simplifying the general equation, Eq. 2.13, the mass conservation equation for the acid solution can be expressed as

$$\frac{\partial\left(C_i\phi\right)}{\partial t} + \overline{\nabla}\cdot(\overline{u}C_i) = R_i \tag{2.20}$$

where

R_i = the rate of appearance of acid i in the solution, [=] g_i/L^3-t;

R_i on the right side of Eq. 2.20 is different with that of Eq. 2.13, which is the source in a general meaning. R_i represents the reaction rate of acid *i* here.

The overall rate of acid consumption or mineral dissolution depends on two parameters, the rate of transport of acid to the mineral surface and the actual reaction rate on the mineral surface. The slower one controls the overall reaction rate. In sandstone acidizing, the HF-mineral reactions are slow compared to the acid transport rate, so the overall rate is controlled by the surface reaction rate.

A reaction rate is generally defined as the rate of appearance in the solution of the species of interest in a particular time period [Economides et al., 1994]. It can be expressed as followings

$$R_i = r_i S_j \tag{2.21}$$

where

r_i = the surface area-specific reaction rate of *i*, [=] mol/s-m^2;

S_j = the surface area of mineral *j* in a unit of bulk volume, [=] m^2/bulk vol..

Because R_i usually depends on the concentration of the reacting species, it can be written as

$$-R_i = E_{f,i,j} C_i^{\alpha} S_j \tag{2.22}$$

where

$E_{f,i,j}$ = the reaction rate constant between acid *i* and mineral *j*, [=] mol A/[m^2-s-(mol A/m^3)$^{\alpha}$.

Because the acid is usually consumed during the reaction, the rate of the disappearance of acid i in the solution is

$$R_i = -\sum_{j=1}^{N_m} E_{f,i,j} S_j^* V_j (1-\phi) C_i^\alpha \tag{2.23}$$

where

N_m = the number of minerals reacting with acid i;

S_j^* = the specific surface area per unit volume of solid, [=] m^2/m^3;

V_j = the volume fraction for mineral j, [=] m^3 mineral j/ m^3 solid volume.

Substituting Eq. 2.23 to Eq. 2.20 yields

$$\frac{\partial (C_i \phi)}{\partial t} + \overline{\nabla} \cdot (\overline{u} C_i) = -\sum_{j=1}^{N_m} E_{f,i,j} S_j^* V_j (1-\phi) C_i^\alpha \tag{2.24}$$

2.1.3.3 Material Balance for Minerals

For the material balance of minerals in sandstone acidizing, it is more convenient to express the amount of mineral in terms of volume fraction. In this case, all the mineral j is in the solid phase. Accordingly, the first term on the right side of Eq. 2.14 drops off and the amount of mineral j in the solid phase can be represented by $(1-\phi)V_j$. Since there is no transport of solid phase, the second term on the left side of Eq. 2.13 disappears. The source term of Eq. 2.13 is the reaction rate of mineral j in this work, which is determined by the acid reaction rate and dissolving power. The dissolving power is the amount of mineral that can be consumed by a given amount of acid [Economides, 1994]. On a mass basis, it is defined as

$$\beta = \frac{\nu_{\min eral} MW_{\min eral}}{\nu_{acid} MW_{acid}} \tag{2.25}$$

So the material balances for all the minerals are expressed as

$$\frac{\partial\left(\left(1-\phi\right)V_j\right)}{\partial t} = -\sum_{i=1}^{N_{a,j}} \frac{MW_i S_j^* V_j \left(1-\phi\right)\beta_{i,j} E_{f,i,j} C_i^{\alpha}}{\rho_j} \qquad j\text{=1,3} \qquad (2.26)$$

where

$N_{a,j}$ = the number of acids reacting with mineral *j*;

$\beta_{i,j}$ = dissolving power of mineral *j* by acid *i*, [=] kg mineral *j*/kg acid *i*;

MW_i = molecular weight of acid *i*, [=] kg/kgmol;

ρ_j = density of mineral *j*, [=] kg/m^3.

Based on the mass balance of the total minerals, the volume of pore space created in the control volume by dissolving minerals can be calculated. So, the net porosity increase during a time period equals the total volume of mineral dissolution minus the volume of precipitate created in this period of time, being

$$\frac{\partial\phi}{\partial t} = -\sum_{j=1}^{N_m}\sum_{i=1}^{N_{a,j}} \frac{MW_i S_j^* V_j \beta_{i,j} E_{f,i,j} C_i}{\rho_j} \qquad (2.27)$$

The final equation system describing the sandstone Acidizing can be expressed as

$$\frac{1}{\mu}\frac{\partial}{\partial x}\left(k_x \frac{\partial P}{\partial x}\right) + \frac{1}{\mu}\frac{\partial}{\partial y}\left(k_y \frac{\partial P}{\partial y}\right) + \frac{1}{\mu}\frac{\partial}{\partial z}\left(k_z \frac{\partial P}{\partial z}\right) = 0 \qquad (2.12)$$

$$\overline{u} = -\frac{\overline{\overline{k}}}{\mu}\cdot\overline{\nabla}P \qquad (2.10)$$

$$\frac{\partial\left(C_i\phi\right)}{\partial t} + \overline{\nabla}\cdot(\overline{u}C_i) = -\sum_{j=1}^{N_m} E_{f,i,j} S_j^* V_j (1-\phi) C_i^{\alpha} \qquad i = 1,\ 2 \qquad (2.24)$$

$$\frac{\partial\left(\left(1-\phi\right)V_j\right)}{\partial t} = -\sum_{i=1}^{N_{a,j}} \frac{MW_i S_j^* V_j \left(1-\phi\right)\beta_{i,j} E_{f,i,j} C_i^{\alpha}}{\rho_j} \qquad j=1,\ 3 \qquad (2.26)$$

$$\frac{\partial \phi}{\partial t} = -\sum_{j=1}^{N_m} \sum_{i=1}^{N_{a,j}} \frac{MW_i S_j^* V_j \beta_{i,j} E_{f,i,j} C_i}{\rho_j} \qquad (2.27)$$

2.1.4 INITIAL AND BOUNDARY CONDITIONS

It is assumed that there is no acid in the system before acid injection. The initial conditions are

$$\left.\begin{aligned} C_{HF} &= C_{H_2SiF_6} = 0 \\ V_1 &= V_1^0 \\ V_2 &= V_2^0 \\ V_3 &= 0 \\ \phi &= \phi^0 \end{aligned}\right\} \quad \text{at } t=0 \qquad (2.28)$$

Where V_1, V_2, V_3, V_1^0, V_2^0, and ϕ^0 are respectively the volume fraction of mineral 1, mineral 2, and mineral 3, original volume fraction of mineral 1 and mineral 2, and original porosity of the core.

During the period of acidizing, acid is injected into the core from the inlet at a constant rate. So, the acid concentration at the inlet equals to the injected concentration, C^0_i. Constant pressure is kept at the outlet of the core. There is no flow on the boundary except at the two ends of the core. Therefore the boundary conditions are

$$C_{HF} = C^0_i \qquad \text{at } x=0 \qquad (2.29)$$

$$Q = \text{Constant} \qquad \text{at } x=0 \qquad (2.30)$$

$$P = P_{out} \qquad \text{at } x = L \tag{2.31}$$

$$\frac{\partial P}{\partial r} = 0 \qquad \text{at } r = r_c \tag{2.32}$$

Where

Q = injection rate

P_{out} = the back pressure applied at the outlet of the core

L = core length

r_c = core radius

The radial coordinate is used here to specify the boundary condition surrounding a core for understanding purpose. It is not applied in simulations.

2.2 Dimensionless Mathematical Model Development

The dimensionless material balance equations of HF, H_2SiF_6, and the three kinds of reactive minerals are developed as follows.

2.2.1 DIMENSIONLESS HF TRANSPORT EQUATION

Based on the material balance equation, for acid HF, i =1, Eq. 2.24 becomes

$$\frac{\partial (C_1 \phi)}{\partial t} + \overline{\nabla} \cdot (\overline{u} C_1) = -\sum_{j=1}^{N_m} E_{f,1,j} S_j^* V_j (1-\phi) C_1^{\alpha} \tag{2.33}$$

Since HF reacts with all of the three minerals present in sandstone acidizing, N_m=3 and Eq. 2.33 can be expanded to

$$\frac{\partial (C_1 \phi)}{\partial t} + \overline{\nabla} \cdot (\overline{u} C_1) =$$

$$-\left(E_{f,1,1}S_1^*V_1(1-\phi)+E_{f,1,2}S_2^*V_2(1-\phi)+E_{f,1,3}S_3^*V_3(1-\phi)\right)C_1^\alpha$$

(2.34)

Let $C_{D1}=\frac{C_1}{C_1^0}$ and $t_D=\frac{ut}{\phi L}$, where C_1^0 is the injected HF concentration, ϕ is the original porosity and u is the injection velocity. ϕ is assumed to be constant when solve acid concentration equations. Because of the assumption of constant injection rate, u is constant here. Therefore,

$$\frac{\phi C_1^0\partial C_{D1}}{\frac{\phi L}{u}\partial t_D}+\overline{\nabla}\cdot(\overline{u}C_{D1}C_1^0)=$$

$$-\left(E_{f,1,1}S_1^*V_1(1-\phi)+E_{f,1,2}S_2^*V_2(1-\phi)+E_{f,1,3}S_3^*V_3(1-\phi)\right)C_1^\alpha$$

(2.35)

Assuming α equals to 1, Eq. 2.35 becomes

$$\frac{\partial C_{D1}}{\partial t_D}+\overline{\nabla}\cdot\left(\frac{\overline{u}}{u}LC_{D1}\right)=$$

$$-\left(E_{f,1,1}S_1^*V_1+E_{f,1,2}S_2^*V_2+E_{f,1,3}S_3^*V_1^0\frac{V_3}{V_1^0}\right)C_{D1}\frac{L}{u}(1-\phi)$$

(2.36)

Let $\overline{u}_D=\frac{\overline{u}}{u}$ and $\overline{\nabla}_D=L\cdot\overline{\nabla}=\frac{\partial}{\partial x_D}+\frac{\partial}{\partial y_D}+\frac{\partial}{\partial z_D}$

$$\frac{\partial C_{D1}}{\partial t_D}+\overline{\nabla}_D\cdot\left(\overline{u}_DC_{D1}\right)=$$

$$-\left(E_{f,1,1}S_1^*V_1^0\frac{V}{V_1^0} + E_{f,1,2}S_2^*V_2^0\frac{V_2}{V_2^0} + E_{f,1,3}S_3^*V_1^0\frac{V_3}{V_1^0}\right)C_{D1}\frac{L}{u}(1-\phi) \tag{2.37}$$

Finally, the dimensionless form of the HF transport equation becomes

$$\frac{\partial C_{D1}}{\partial t_D} + \overline{\nabla}_D \cdot \left(\bar{u}_D C_{D1}\right) = -\left(N_{Da,1}\Lambda_1 + N_{Da,2}\Lambda_2 + N_{Da,3}\Lambda_3\right)C_{D1} \tag{2.38}$$

Where N_{Da} is called Damkohler number. It is the ratio of the rate of acid consumption to the rate of acid convection. We assume the specific surface area of mineral is constant during sandstone acidizing. The Damkohler numbers for the first three reactions listed in the chemical reaction model are then defined as

$$N_{Da,1} = \frac{E_{f,1,1}S_1^*V_1^0(1-\phi)L}{u} \tag{2.39}$$

$$N_{Da,2} = \frac{E_{f,1,2}S_2^*V_2^0(1-\phi)L}{u} \tag{2.40}$$

$$N_{Da,3} = \frac{E_{f,1,3}S_3^*V_1^0(1-\phi)L}{u} \tag{2.41}$$

Λ is dimensionless mineral composition. The dimensionless volume fractions of the three kinds of mineral are defined as

$$\Lambda_1 = \frac{V_1}{V_1^0} \tag{2.42}$$

$$\Lambda_2 = \frac{V_2}{V_2^0} \tag{2.43}$$

$$\Lambda_3 = \frac{V_3}{V_1^0} \tag{2.44}$$

2.2.2 DIMENSIONLESS H_2SiF_6 BALANCE EQUATION

In acid solution, other forms of fluosilicic acid than H_2SiF_6 are neglected. Acid H_2SiF_6 is consumed only by reacting with fast reacting mineral and produces silica gel. However it is also a product of the reactions between HF and all the three reactive minerals. So the material balance equation of H_2SiF_6 is

$$\frac{\partial(C_2\phi)}{\partial t} + \overline{\nabla} \cdot (\overline{u} C_2) = -E_{f,2,1} S_1^* V_1 (1-\phi) C_2^\alpha$$

$$+ \left(\frac{v_5}{v_1} E_{f,1,1} S_1^* V_1 (1-\phi) + \frac{v_6}{v_2} E_{f,1,2} S_2^* V_2 (1-\phi) + \frac{v_7}{v_3} E_{f,1,3} S_3^* V_3 (1-\phi) \right) C_1^\alpha \tag{2.45}$$

where ν_i are the stoichiometric coefficients mentioned in the chemical reaction model section at the beginning of this chapter. They are usually determined by experiments.

Let $C_{D2} = \frac{C_2}{C_1^0}$ and $t_D = \frac{ut}{\phi L}$, Eq. 2.45 becomes

$$\frac{\phi C_1^0 \partial C_{D2}}{\frac{\phi L}{u} \partial t_D} + \overline{\nabla} \cdot (\overline{u} C_{D2} C_1^0) = -\left(E_{f,2,1} S_1^* V_1 (1-\phi)\right) C_2^\alpha$$

$$+ \left(\frac{v_5}{v_1} E_{f,1,1} S_1^* V_1 (1-\phi) + \frac{v_6}{v_2} E_{f,1,2} S_2^* V_2 (1-\phi) + \frac{v_7}{v_3} E_{f,1,3} S_3^* V_3 (1-\phi) \right) C_1^\alpha \tag{2.46}$$

$$\frac{\partial C_{D2}}{\partial t_D} + \overline{\nabla}_D \cdot (\frac{\overline{u}}{u} C_{D2}) = -\left(E_{f,2,1_6} S_1^* V_1^0 (1-\phi)\right) C_{D2} \frac{V_1}{V_1^0} \frac{L}{u}$$

$$+(\frac{v_5}{v_1}E_{f,1,1}S_1^*V_1^0(1-\phi)\frac{V_1}{V_1^0}+\frac{v_6}{v_2}E_{f,1,2}S_2^*V_2^0(1-\phi)\frac{V_2}{V_2^0}$$

$$+\frac{v_7}{v_3}E_{f,1,3}V_1^0S_3^*(1-\phi)\frac{V_3}{V_1^0})C_{D1}\frac{L}{u} \tag{2.47}$$

$$\frac{\partial C_{D2}}{\partial t_D}+\overline{\nabla}_D\cdot(\overline{u}_DC_{D2})=$$

$$-N_{Da,4}C_{D2}\Lambda_1+\left(\frac{v_5}{v_1}N_{Da,1}\Lambda_1+\frac{v_6}{v_2}N_{Da,2}\Lambda_2+\frac{v_7}{v_3}N_{Da,3}\Lambda_3\right)C_{D1} \tag{2.48}$$

The Damkohler number for the fourth reaction, $N_{Da,4}$, is defined as

$$N_{Da,4}=\frac{E_{f,2,1_6}S_1^*V_1^0\left(1-\phi\right)L}{u} \tag{2.49}$$

2.2.3 DIMENSIONLESS MINERAL BALANCE EQUATIONS

According to the material balance equation for minerals, Eq. 2.26, we can develop the dimensionless form for each of the three minerals as following.

Fast reacting mineral reacts with both of the two acids, HF and H_2SiF_6. So the material balance equation for fast reacting mineral becomes

$$\frac{\partial\left(\left(1-\phi\right)V_1\right)}{\partial t}=-\frac{MW_{HF}S_1^*V_1\left(1-\phi\right)\beta_{HF,1}E_{f,HF,1}C_{HF}}{\rho_1}$$

$$-\frac{MW_{H_2SiF_6}S_1^*V_1\left(1-\phi\right)\beta_{H_2SiF_6,1}E_{f,H_2SiF_6,1}C_{H_2SiF_6}}{\rho_1} \tag{2.50}$$

Taking porosity as a constant in this equation, then

$$\frac{\partial V_1}{\partial t} = -\left(MW_{HF}\beta_{HF,1}E_{f,HF,1}C_{HF} + MW_{H_2SiF_6\,1}\beta_{H_2SiF_6,1}E_{f,H_2SiF_6,1}C_{H_2SiF_6} \right)\frac{S_1^* V_1}{\rho_1} \tag{2.51}$$

Substituting the definition of dimensionless fast reacting volume fraction, Eq. 2.42, and dimensionless time into above equation, it becomes

$$\begin{aligned}\frac{\partial \Lambda_1}{\partial t_D} &= -\left(MW_{HF}\beta_{HF,1}E_{f,HF,1}C_{HF} + MW_{H_2SiF_6\,1}\beta_{H_2SiF_6,1}E_{f,H_2SiF_6,1}C_{H_2SiF_6} \right)\frac{S_1^* V_1 \phi L}{\rho_1 u V_1^0} \\ &= -\Big(\frac{(1-\phi)V_1^0 E_{f,HF,1}S_1^* L}{u}\cdot\frac{1}{(1-\phi)V_1^0}\cdot\frac{\phi MW_{HF}C_{HF}^0\beta_{HF,1}}{\rho_1}\frac{C_{HF}}{C_{HF}^0} \\ &\quad + \frac{(1-\phi)V_1^0 E_{f,H_2SiF_6,1}S_1^* L}{u}\cdot\frac{1}{(1-\phi)V_1^0}\cdot\frac{\phi C_{HF}^0 MW_{H_2SiF_6}\beta_{H_2SiF_6,1}}{\rho_1}\frac{C_{H_2SiF_6}}{C_{HF}^0}\Big)\frac{V_1}{V_1^0}\end{aligned} \tag{2.52}$$

Simplifying the above equation according to equations 2.39-2.42, it becomes

$$\frac{\partial \Lambda_1}{\partial t_D} = -\left(N_{Da,1}\cdot N_{Ac,1}\cdot C_{D1} + N_{Da,4}\cdot N_{Ac,4}\cdot C_{D2} \right)\cdot \Lambda_1 \tag{2.53}$$

N_{Ac} is a dimensionless number called acid capacity number. It is the ratio of the amount of mineral dissolved by the acid occupying a unit volume of rock pore space to the amount of mineral present in the unit volume of rock. The acid capacity number for the first and the last reactions mentioned at the beginning of this chapter are defined as

$$N_{AC,1} = \frac{\phi C_{HF}^0 MW_{HF}\beta_{HF,1}}{(1-\phi)V_1^0\rho_1} \tag{2.54}$$

$$N_{AC,4} = \frac{\phi C_{HF}^{0} MW_{H_2SiF_6} \beta_{H_2SiF_6,1}}{(1-\phi)V_1^{0} \rho_1} \tag{2.55}$$

Slow reacting mineral reacts only with HF, so its material balance is described by the following equation,

$$\frac{\partial((1-\phi)V_2)}{\partial t} = -\frac{MW_{HF} S_2^{*} V_2 (1-\phi)\beta_{HF,2} E_{f,HF,2} C_{HF}}{\rho_2} \tag{2.56}$$

Introducing those dimensionless numbers into Eq. 2.56, one gets

$$\frac{\partial \Lambda_2}{\partial t_D} = -\frac{MW_{HF} S_2^{*} V_2 \beta_{HF,2} E_{f,HF,2} C_{HF}}{\rho_2} \frac{\phi L}{V_2^{0} u}$$

$$= -\frac{(1-\phi)S_2^{*} E_{f,HF,2} V_2^{0} L}{u} \frac{1}{(1-\phi)V_2^{0}} \frac{\phi MW_{HF} \beta_{HF,2} C_{HF}^{0}}{\rho_2} \frac{V_2}{V_2^{0}} \frac{C_{HF}}{C_{HF}^{0}} \tag{2.57}$$

$$\frac{\partial \Lambda_2}{\partial t_D} = N_{Da,2} N_{Ac,2} \Lambda_2 C_{D1} \tag{2.58}$$

The acid capacity number for HF dissolving slow reacting mineral is defined as

$$N_{AC,2} = \frac{\phi C_{HF}^{0} MW_{HF} \beta_{HF,2}}{(1-\phi)V_2^{0} \rho_2} \tag{2.59}$$

The precipitate is referred as mineral 3 in this work. It is consumed by reacting with HF but is produced by the reaction between H_2SiF_6 and fast-reacting mineral. One can determine how much mineral 3 is produced based on the amount of dissolved fast reacting mineral and the reaction stoichiometry.

$$\frac{\partial((1-\phi)V_3)}{\partial t} = -(MW_{HF} \beta_{HF,3} E_{f,HF,3} C_{HF} \frac{S_3^{*} V_3}{\rho_3}$$

$$- MW_{H_2SiF_6 1}\beta_{H_2SiF_6,1}E_{f,H_2SiF_6,1}C_{H_2SiF_6}S_1^*V_1\frac{v_8 MW_3}{MW_1\rho_3})(1-\phi) \tag{2.60}$$

In the above equation, $C_{H_2SiF_6}(1-\phi)E_{f,H_2SiF_6,1}S_1^*V_1$ is the amount of moles of the consumed H_2SiF_6, $(1-\phi)MW_{H_2SiF_6 1}\beta_{H_2SiF_6,1}E_{f,H_2SiF_6,1}C_{H_2SiF_6}S_1^*V_1$ is the mass of fast-reacting mineral that is dissolved by H_2SiF_6 per unit volume, and $\frac{v_8 MW_3}{MW_1\rho_3}(1-\phi)MW_{H_2SiF_6 1}\beta_{H_2SiF_6,1}E_{f,H_2SiF_6,1}C_{H_2SiF_6}S_1^*V_1$ is the volume of mineral 3 that produced corresponding to the reaction of H_2SiF_6 with fast-reacting mineral.

Introducing these dimensionless numbers into Eq. 2.60, it becomes

$$\begin{aligned}\frac{\partial\Lambda_3}{\partial t_D} &= -(MW_{HF}\beta_{HF,3}E_{f,HF,3}C_{HF}\frac{S_3^*V_3}{\rho_3} \\ &\quad - MW_{H_2SiF_6 1}\beta_{H_2SiF_6,1}E_{f,H_2SiF_6,1}C_{H_2SiF_6}S_1^*V_1\frac{v_8 MW_3}{MW_1\rho_3})\frac{\phi L}{V_1^0 u} \\ &= -\frac{(1-\phi)S_3^*E_{f,HF,3}V_1^0 L}{u}\frac{MW_{HF}\beta_{HF,3}C_{HF}^0\phi}{(1-\phi)V_1^0\rho_3}\frac{V_3}{V_1^0}\frac{C_{HF}}{C_{HF}^0} \\ &\quad + \frac{\phi MW_{H_2SiF_6 1}\beta_{H_2SiF_6,1}C_{HF}^0}{(1-\phi)V_1^0\rho_1}\frac{(1-\phi)S_1^*E_{f,H_2SiF_6,1}V_1^0 L}{u}\frac{V_1}{V_1^0}\frac{C_{H_2SiF_6}}{C_{HF}^0}\frac{v_8 MW_3}{MW_1}\frac{\rho_1}{\rho_3}\end{aligned} \tag{2.61}$$

$$\frac{\partial\Lambda_3}{\partial t_D} = -\left(N_{Da,3}N_{Ac,3}\Lambda_3 C_{D1} - N_{Da,4}N_{Ac,4}\Lambda_1 C_{D2}\frac{v_8 MW_3}{MW_1}\frac{\rho_1}{\rho_3}\right) \tag{2.62}$$

And the acid capacity number for the third reaction is defined as

$$N_{Ac,3} = \frac{\phi MW_{HF}\beta_{HF,3}C_{HF}^0}{(1-\phi)V_1^0\rho_3} \tag{2.63}$$

2.2.4 DIMENSIONLESS INITIAL AND BOUNDARY CONDITIONS

The initial conditions to solve the equations are expressed as follows,

$$\left.\begin{array}{l} C_{D,1} = C_{D,2} = 0 \\ \Lambda_1 = \Lambda_2 = 1 \\ \Lambda_3 = 0 \\ \phi = \phi^0 \end{array}\right. \qquad t_D = 0 \tag{2.64}$$

The boundary conditions applied here are

$$C_{D,1} = 1 \qquad x_D = 0 \tag{2.65}$$

$$Q = \text{Constant} \qquad x_D = 0 \tag{2.66}$$

$$P = P_{out} \qquad x_D = 1 \tag{2.67}$$

$$\frac{\partial P}{\partial r} = 0 \qquad r = r_c \tag{2.68}$$

The last boundary condition is also presented in radial coordinates just for understanding purpose.

The equations along with boundary and initial conditions that are solved for acid concentration, mineral concentration, and pressure field can be summarized as follows,

$$\frac{1}{\mu}\frac{\partial}{\partial x}\left(k_x \frac{\partial P}{\partial x}\right) + \frac{1}{\mu}\frac{\partial}{\partial y}\left(k_y \frac{\partial P}{\partial y}\right) + \frac{1}{\mu}\frac{\partial}{\partial z}\left(k_z \frac{\partial P}{\partial z}\right) = 0 \tag{2.12}$$

$$\frac{\partial C_{D1}}{\partial t_D} + \overline{\nabla}_D \cdot \left(u_D C_{D1}\right) = -\left(N_{Da,1}\Lambda_1 + N_{Da,2}\Lambda_2 + N_{Da,3}\Lambda_3\right) C_{D1} \tag{2.38}$$

$$\frac{\partial C_{D2}}{\partial t_D} + \overline{\nabla}_D \cdot (\overline{u}_D C_{D2}) =$$

$$-N_{Da,4} C_{D2} \Lambda_1 + \left(\frac{v_5}{v_1} N_{Da,1} \Lambda_1 + \frac{v_6}{v_2} N_{Da,2} \Lambda_2 + \frac{v_7}{v_3} N_{Da,3} \Lambda_3 \right) C_{D1}$$

(2.48)

$$\frac{\partial \Lambda_1}{\partial t_D} = -\left(N_{Da,1} \cdot N_{Ac,1} \cdot C_{D1} + N_{Da,4} \cdot N_{Ac,4} \cdot C_{D2} \right) \cdot \Lambda_1 \qquad (2.53)$$

$$\frac{\partial \Lambda_2}{\partial t_D} = N_{Da,2} N_{Ac,2} \Lambda_2 C_{D1} \qquad (2.58)$$

$$\frac{\partial \Lambda_3}{\partial t_D} = -\left(N_{Da,3} N_{Ac,3} \Lambda_3 C_{D1} - N_{Da,4} N_{Ac,4} \Lambda_1 C_{D2} \frac{v_8 MW_3}{MW_1} \frac{\rho_1}{\rho_3} \right) \qquad (2.62)$$

$$\left.\begin{array}{l} C_{D,1} = C_{D,2} = 0 \\ \Lambda_1 = \Lambda_2 = 1 \\ \Lambda_3 = 0 \\ \phi = \phi^0 \end{array}\right. \qquad t = 0 \qquad (2.64)$$

$$C_{D,1} = 1 \qquad x_D = 0 \qquad (2.65)$$

$$Q = \text{Constant} \qquad x_D = 0 \qquad (2.66)$$

$$P = P_{out} \qquad x_D = 1 \qquad (2.67)$$

$$\frac{\partial P}{\partial r} = 0 \qquad r = r_c \qquad (2.68)$$

CHAPTER 3 NUMERICAL SOLUTION OF THE ACIDIZING MODEL

3.1 Gridding Method

To show the effect of rock property heterogeneity on sandstone acidizing in a fine scale, a typical core with dimensions of 1-inch diameter and 2-inch length is divided into 8000 grid blocks. Because acid flows in three dimensions with different velocities, different spatial intervals in different directions are adopted in the simulation. In the main acid flow direction, velocity is much higher than the other two dimensions and therefore smaller spatial steps are used to minimize numerical errors. The core is divided into 100 grid blocks in the acid main flow direction. A total of 80 grid blocks on each cross section are used to approximate the cross section of cylindrical cores. Figure 3.1 shows the gridding schematic of the core, in which *x* represents the main flow direction and a *y*-*z* plane represents cross section of a core. With sand grain diameter of 0.1 mm, there are more than 6000 sand grains in each grid block, so the size of grid block meet the requirement of continues properties.

3.2 Development of Finite Difference Form of Equations

3.2.1 FINITE DIFFERENCE FORM OF EQUATION 2.12

Using the seven-point finite difference scheme in each plane, the grids involved to solve the equations at a grid with indices *i*, *j*, *k* in *x*, *y*, and *z* direction respectively can be represented by Figure 3.2.

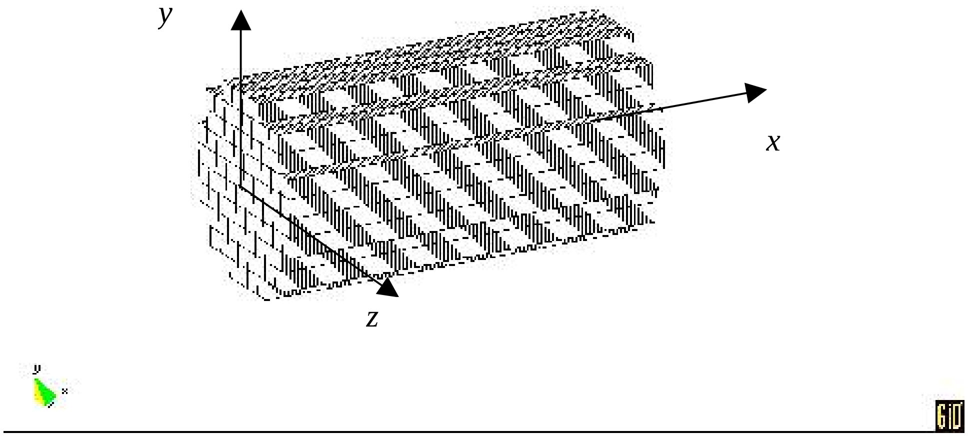

Figure 3.1: The gridding method of a core.

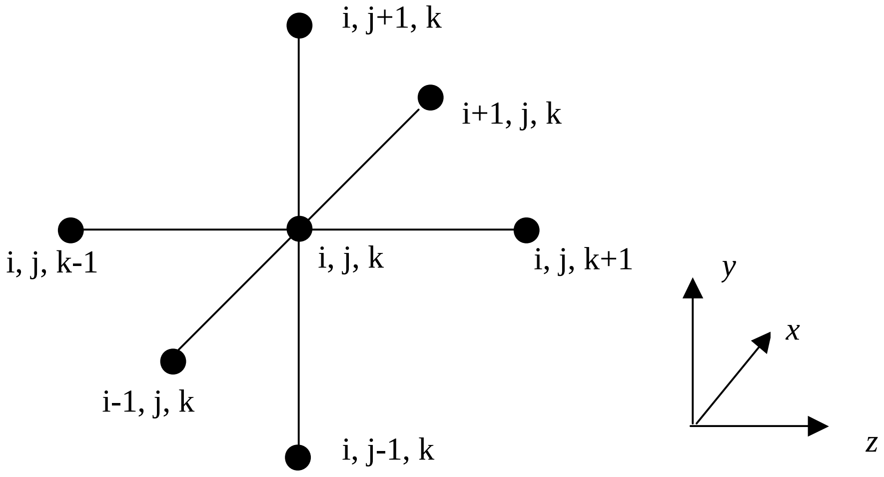

Figure 3.2: Finite difference domain.

The first term in Eq. 2.12 can be expressed as

$$\frac{1}{\mu}\frac{\partial}{\partial x}\left(k_x\frac{\partial P}{\partial x}\right)\bigg|_{i,j,k}=\frac{1}{\mu}\frac{k_x\dfrac{\partial P}{\partial x}\bigg|_{i+1/2,j,k}-k_x\dfrac{\partial P}{\partial x}\bigg|_{i-1/2,j,k}}{x_{i+1/2,j,k}-x_{i-1/2,j,k}}$$

$$=\frac{1}{\mu}\frac{k_x\big|_{i+1/2,j,k}\left(\dfrac{P_{i+1,j,k}-P_{i,j,k}}{\Delta x_{i+1,j,k}}\right)-k_x\big|_{i-1/2,j,k}\left(\dfrac{P_{i,j,k}-P_{i-1,j,k}}{\Delta x_{i,j,k}}\right)}{\dfrac{1}{2}\left(\Delta x_{i+1,j,k}+\Delta x_{i,j,k}\right)} \qquad (3.1)$$

When the space step is uniform, Δx is constant for each grid. The above equation becomes

$$\frac{1}{\mu}\frac{\partial}{\partial x}\left(k_x\frac{\partial P}{\partial x}\right)\bigg|_{i,j,k}=\frac{1}{\mu}\frac{k_x\big|_{i+1/2,j,k}\left(P_{i+1,j,k}-P_{i,j,k}\right)-k_x\big|_{i-1/2,j,k}\left(P_{i,j,k}-P_{i-1,j,k}\right)}{\Delta x^2}$$

(3.2)

Similarly, assuming the spatial intervals in *y* and *z* direction are also uniform for the whole domain, the second order pressure derivatives with respect to *y* and *z* at point (*i*,*j*,*k*) can be expressed by the following finite difference forms,

$$\frac{1}{\mu}\frac{\partial}{\partial y}\left(k_y\frac{\partial P}{\partial y}\right)\bigg|_{i,j,k}=\frac{1}{\mu}\frac{k_y\big|_{i,j+1/2,k}\left(P_{i,j+1,k}-P_{i,j,k}\right)-k_y\big|_{i,j-1/2,k}\left(P_{i,j,k}-P_{i,j-1,k}\right)}{\Delta y^2}$$

(3.3)

$$\frac{1}{\mu}\frac{\partial}{\partial z}\left(k_z\frac{\partial P}{\partial z}\right)\bigg|_{i,j,k}=\frac{1}{\mu}\frac{k_z\big|_{i,j,k+1/2}\left(P_{i,j,k+1}-P_{i,j,k}\right)-k_z\big|_{i,j,k-1/2}\left(P_{i,j,k}-P_{i,j,k-1}\right)}{\Delta z^2}$$

(3.4)

Substitute Eq. 3.2 ~ Eq. 3.4 into Eq. 2.12 the finite difference form for Eq. 2.12 becomes

$$\frac{1}{\mu}\frac{k_x\big|_{i+1/2,j,k}\left(P_{i+1,j,k}-P_{i,j,k}\right)-k_x\big|_{i-1/2,j,k}\left(P_{i,j,k}-P_{i-1,j,k}\right)}{\Delta x^2}$$

$$+\frac{1}{\mu}\frac{k_y\big|_{i,j+1/2,k}\left(P_{i,j+1,k}-P_{i,j,k}\right)-k_y\big|_{i,j-1/2,k}\left(P_{i,j,k}-P_{i,j-1,k}\right)}{\Delta y^2}$$

$$+\frac{1}{\mu}\frac{k_z\big|_{i,j,k+1/2}\left(P_{i,j,k+1}-P_{i,j,k}\right)-k_z\big|_{i,j,k-1/2}\left(P_{i,j,k}-P_{i,j,k-1}\right)}{\Delta z^2}=0 \qquad (3.5)$$

with the permeability at boundaries among grid blocks defined as

$$k_x\bigg|_{i+1/2,j,k}=2\frac{k_{xi,j,k}\cdot k_{xi+1,j,k}}{k_{xi,j,k}+k_{xi+1,j,k}} \qquad (3.6)$$

3.2.2 FINITE DIFFERENCE FORM OF EQ. 2.24

The time derivative in Eq. 2.24 can be expressed as

$$\phi_{i,j,k}\frac{\partial\left(C_i\right)_{i,j,k}}{\partial t}=\phi_{i,j,k}\left(\frac{\left(C_i\right)_{i,j,k}^{n+1}-\left(C_i\right)_{i,j,k}^{n}}{\Delta t}\right) \qquad (3.7)$$

Assuming uniform spatial step in each direction, the second term on the left side of Eq. 2.24 can be differenced at point (i, j, k) as follows

$$\nabla\cdot\left(\bar{u}C_i\right)_{i,j,k}=\frac{\partial\left(u_xC_i\right)_{i,j,k}}{\partial x}+\frac{\partial\left(u_yC_i\right)_{i,j,k}}{\partial y}+\frac{\partial\left(u_zC_i\right)_{i,j,k}}{\partial z}$$

$$=\frac{1}{\Delta x}\left(\left(u_xC_i\right)_{i,j,k}-\left(u_xC_i\right)_{i-1,j,k}\right)+\frac{1}{\Delta y}\left(\left(u_yC_i\right)_{i,j,k}-\left(u_yC_i\right)_{i,j-1,k}\right)$$

$$+\frac{1}{\Delta z}\left(\left(u_zC_i\right)_{i,j,k}-\left(u_zC_i\right)_{i,j,k-1}\right) \qquad (3.8)$$

The Darcy velocity in the above equation can be calculated by Darcy's Law. For instance,

$$u_x\big|_{i,j,k} = \frac{k_x\big|_{i,j,k}}{\mu}\frac{P_{i+1,j,k} - P_{i-1,j,k}}{2\Delta x} \tag{3.9}$$

So the finite difference form for Eq. 2.24 becomes

$$\begin{aligned}
&\phi_{i,j,k}\left(\frac{(C_i)^{n+1}_{i,j,k} - (C_i)^{n}_{i,j,k}}{\Delta t}\right) + \frac{1}{\Delta x}\Big((u_x C_i)_{i,j,k} - (u_x C_i)_{i-1,j,k}\Big) \\
&\quad + \frac{1}{\Delta y}\Big((u_y C_i)_{i,j,k} - (u_y C_i)_{i,j-1,k}\Big) + \frac{1}{\Delta z}\Big((u_z C_i)_{i,j,k} - (u_z C_i)_{i,j,k-1}\Big) \\
&\quad = \left(-(1-\phi)\sum_{j=1}^{N_m} E_{f,j} S_j^* V_j C_i^{\alpha}\right)_{i,j,k}
\end{aligned} \tag{3.10}$$

3.2.3 FINITE DIFFERENCE FORM OF EQ. 2.25

The finite difference form for Eq. 2.25 is

$$\left(1-\phi_{i,j,k}\right)\frac{V_j^{n+1}\big|_{i,j,k} - V_j^{n}\big|_{i,j,k}}{\Delta t} = \left(-\sum_{i=1}^{N_{a,j}} \frac{MW_i S_j^* V_j (1-\phi)\beta_{i,j} E_{i,j} C_i^{\alpha}}{\rho_j}\right)\Bigg\|_{i,j,k} \quad j=1,3 \tag{3.11}$$

3.2.4 FINITE DIFFERENCE FORM OF EQ. 2.26

The finite difference form for Eq. 2.26 is also very simple because it only involves the porosity derivative with respect to time. It can be differenced as

$$\frac{\phi_{i,j,k}^{n+1} - \phi_{i,j,k}^{n}}{\Delta t} = \left(-\sum_{i1=1}^{N_a} \sum_{j1=1}^{N_m} \frac{MW_{i1} S_{j1}^{*} V_{j1} \beta_{i1,j1} E_{i1,j1} C_{1i}}{\rho_{j1}} \right)_{i,j,k} \tag{3.12}$$

Equations 3.5, 3.10, 3.11 and 3.12 are the finite difference equations solved in the simulator. They are discussed in detail later in this chapter. The initial porosity, concentrations of the two acids and mineral compositions are taken as input data to the simulator.

3.2.4 INITIAL AND BOUNDARY CONDITIONS

At the beginning of acid core flooding simulation, the pressure in each grid block equals to the original pressure, HF concentration for each cell of the core sample is 0, and the porosity is the original porosity. They can be represented as follows,

$$\left.\begin{aligned} C_{HF,i,j,k} &= C_{H_2SiF_6,i,j,k} = 0 \\ V_{1,i,j,k} &= V_{1,i,jk}^{0} \\ V_{2,i,j,k} &= V_{2,i,j,k}^{0} \\ V_{3,i,j,k} &= 0 \\ \phi_{i,j,k} &= \phi^{0} \end{aligned}\right\} \quad t = 0 \tag{3.13}$$

where *i*, *j*, *k* are indices in three directions.

During the period of acidizing, acid is injected into the core from the inlet at a constant rate. Constant pressure is kept at the outlet side of the core, and there is no flow on the boundary except at the two ends of the core.

$$C_{HF,i,j,k} = C_{HF,i}^{0} \qquad i=0 \tag{3.14}$$

$$\sum_{j=0}^{N_y} \sum_{k=0}^{N_z} q_{i,j,k} = Q \qquad i=0 \tag{3.15}$$

$$P_{i,j,k}=P_{out} \qquad i=N_x\text{-}1 \qquad (3.16)$$

where

q = injection rate for a grid block

N_x = number of grid blocks in x direction

N_y = number of grid blocks in y direction

N_z = number of grid blocks in z direction

3.3 Implementation

Next to be discussed is about the program implementation and the numerical realization used in developing the simulator, UT3DAcid.

3.3.1 CALCULATION OF PRESSURE DISTRIBUTION

Because of the heterogeneous distribution of porosity and minerals, acid flows not only along the main acid flow direction. A flux also exists between grid blocks with the same position in the x direction if there is a pressure gradient. To predict acid flow in sandstone core, it is necessary to update pressure for each time step.

3.3.1.1 Generation of Coefficient Matrix

Based on the dimensionless equations and their finite difference forms previously mentioned, a set of linear equations is solved to obtain the pressure distribution at each time step. The coefficient matrix for this problem is a sparse seven-banded matrix. However, it is not a regular banded matrix because the number of grid blocks in the *y* direction and the z direction varies. For example, referring to Figure 3.1, the top row of grids has 4 grid blocks in the *z* direction, while the next two rows each has 8 *z* direction grid blocks. The general form of the matrix is shown in Figure 3.3.

For the inner grids that are not on the boundary, or in other words, when $i \neq 0, \quad i \neq Nx-1, \quad j \neq 0, \quad j \neq Ny-1, \quad k \neq 0,$ and $k \neq Nz-1$, the corresponding elements in the matrix are calculated as the following,

$$
\left\{
\begin{array}{cccccccccccccccccccc}
A & B & . & . & . & D & . & . & . & F & & & & & & & & & & \\
C & A & B & & & & D & & & & F & & & & & & & & & \\
. & C & . & . & & & & . & & & & . & & & & & & & & \\
. & & . & . & . & & & & . & & & & . & & & & & & & \\
. & & & . & . & . & & & & 0 & & & & . & & & & & & \\
E & & & & . & A & 0 & & & & D & & & & . & & & & & \\
. & . & & & & 0 & A & B & & & & . & & & & . & & & & \\
. & & . & & & & C & . & . & & & & . & & & & 0 & & & \\
. & & & . & & & & . & A & . & & & & . & & & & F & & \\
G & & & & 0 & & & & . & . & . & & & & . & & & & F & \\
 & G & & & & E & & & & . & . & B & & & & D & & & & F \\
 & & . & & & & . & & & & C & . & . & & & & . & & & \\
 & & & . & & & & . & & & & . & . & . & & & & . & & \\
 & & & & . & & & & . & & & & . & . & . & & & & D & \\
 & & & & & 0 & & & & E & & & & . & . & B & & & & D \\
 & & & & & & G. & & & & . & & & & C & . & . & & & \\
 & & & & & & & . & & & & . & & & & . & . & . & & \\
 & & & & & & & & . & & & & . & & & & . & . & . & \\
 & & & & & & & & & . & & & & E & & & & . & A & B \\
 & & & & & & & & & & G & & & & E & & & & C & A
\end{array}
\right\}
$$

Figure 3.3: The general coefficient matrix to solve the pressure equation.

A is the diagonal of the matrix and represents the coefficient for the current grid block.

$$
A = -\frac{1}{\mu}\frac{k_x|_{i+1/2,j,k}}{\Delta x^2} - \frac{1}{\mu}\frac{k_x|_{i-1/2,j,k}}{\Delta x^2} - \frac{1}{\mu}\frac{k_y|_{i,j-1/2,k}}{\Delta y^2} - \frac{1}{\mu}\frac{k_y|_{i,j+1/2,k}}{\Delta y^2} - \frac{1}{\mu}\frac{k_z|_{i,j,k-1/2}}{\Delta z^2}
$$

$$
- \frac{1}{\mu}\frac{k_z|_{i,j,k+1/2}}{\Delta z^2} \tag{3.17}
$$

B is the coefficient for the next grid in *z* direction.

$$B = \frac{1}{\mu}\frac{k_z|_{i,j,k+1/2}}{\Delta z^2} \tag{3.18}$$

C represents the coefficient for the previous grid in the fastest changing direction, *z* direction.

$$C = \frac{1}{\mu}\frac{k_z|_{i,j,k-1/2}}{\Delta z^2} \tag{3.19}$$

D is the coefficient for the next grid in *y* direction.

$$D = \frac{1}{\mu}\frac{k_y|_{i,j+1/2,k}}{\Delta y^2} \tag{3.20}$$

E is the coefficient for the previous grid in the second slowest changing direction, *y* direction.

$$E = \frac{1}{\mu}\frac{k_y|_{i,j-1/2,k}}{\Delta y^2} \tag{3.21}$$

F is the coefficient for the next grid in the slowest changing direction, *x* direction.

$$F = \frac{1}{\mu}\frac{k_x|_{i+1/2,j,k}}{\Delta x^2} \tag{3.22}$$

G represents the coefficient for the previous grid in the slowest changing direction, *x* direction.

$$G = \frac{1}{\mu}\frac{k_x|_{i-1/2,j,k}}{\Delta x^2} \tag{3.23}$$

For grid blocks on the boundaries, boundary conditions should be taken into consideration when generating the coefficient matrix.

1. Constant pressure at outlet.

When *i* equals to *Nx*-1, the outlet boundary condition applies. In this case, the element F equals to 0, line 8 in the matrix for example. Other elements in that row except A are calculated the same way as the inner grid blocked mentioned above. The diagonal element is expressed as

$$A = -\frac{1}{\mu}\frac{2\cdot k_x\big|_{i+1/2,j,k}}{\Delta x^2} - \frac{1}{\mu}\frac{k_x\big|_{i-1/2,j,k}}{\Delta x^2} - \frac{1}{\mu}\frac{k_y\big|_{i,j-1/2,k}}{\Delta y^2} - \frac{1}{\mu}\frac{k_y\big|_{i,j+1/2,k}}{\Delta y^2}$$

$$-\frac{1}{\mu}\frac{k_z\big|_{i,j,k-1/2}}{\Delta z^2} - \frac{1}{\mu}\frac{k_z\big|_{i,j,k+1/2}}{\Delta z^2} \qquad (3.24)$$

2. Constant injection rate at inlet.

At the inlet, the total injection rate is constant during acidizing. However, the injection rate for each grid block changes with time because of the permeability update. Therefore this boundary condition cannot be applied directly to the numerical model. One simple way to solve this problem is to give an initial guess of the inlet pressure, P_{in}. Then in the calculation, the linear equations are solved by assuming that the pressure at the inlet is P_{in}. Once the pressure distribution is obtained, the injection rate for each grid block can be calculated using Darcy's law. The calculated injection rate is compared with the desired injection rate and then the initial pressure adjusted. The prediction of next P_{in} to try is based on the difference of the calculated injection rate and the given injection rate and the last P_{in} guess value. The following algorithm shows the procedure to test the guessed P_{in} right or not and that to seek for the right P_{in}.

Step 1: if $\left|Q - Q_c\right| < e$ or $Q_c < 0$ go to Step 2, otherwise go to Step 6.

Step 2: if it is not the first iteration to seek for the correct P_{in},

$$P_{in} = \frac{Q_{old} - Q}{Q_{old} - Q_c} \cdot P_{in} - \frac{Q_c - Q}{Q_{old} - Q_c} \cdot P_{old1} \tag{3.25}$$

then go to Step 4, otherwise go to Step 3.

Step 3: if $Q_c < 0$ then

$$P_{in} = P_{in} \cdot \left((1 - w) + w \cdot \frac{Q - Q_c}{\max(Q, Q_c)} \right) \tag{3.26}$$

otherwise,

$$P_{in} = P_{in} \cdot \left(w + (1 - w) \frac{Q}{Q_c} \right) \tag{3.27}$$

Step 4: increase n by 1, assign Q_{old} by the current calculated injection rate, Q_c, assign the value of P_{old} to P_{old1} and assign the value of current P_{in} to P_{old}. Then go to Step 5.

Step 5: Calculate pressure distribution using the predicted P_{in}, and calculate the injection rate, Q_c, go to Step 1.

Step 6: The right P_{in} has been obtained. Continue to calculate acid distributions.

Where Q = given injection rate

Q_c = calculated injection rate

e = error limit

n = number of iterations to predict pressure

Q_{old} = calculated injection rate in the last iteration

P_{old} = the predicted pressure for last iteration

P_{old1} = the predicted pressure for the iteration before the last

w = weight

max(Q, Q_c) = the bigger one between q and q_c

From above pseudo code, it can be seen that the next inlet pressure to try is actually predicted by the pressure and injection rate of the last two guesses. Simulations found that it took at most 3 times to find the right pressure input. w is an important parameter here. It determines how much the current pressure should change. A good choice of w results in fast convergence while a poor choice of w can lead to divergence of the problem.

Since the boundary condition at the inlet of a core changed from constant injection rate to given pressure, the finite difference form of Eq. 3.5 can be written as the following,

$$\begin{aligned}
&\frac{1}{\mu}\frac{k_x\big|_{i+1/2,j,k}\left(P_{i+1,j,k}-P_{i,j,k}\right)-2\cdot k_x\big|_{i-1/2,j,k}P_{i,j,k}}{\Delta x^2} \\
&+\frac{1}{\mu}\frac{k_y\big|_{i,j+1/2,k}\left(P_{i,j+1,k}-P_{i,j,k}\right)-k_y\big|_{i,j-1/2,k}\left(P_{i,j,k}-P_{i,j-1,k}\right)}{\Delta y^2} \\
&+\frac{1}{\mu}\frac{k_z\big|_{i,j,k+1/2}\left(P_{i,j,k+1}-P_{i,j,k}\right)-k_z\big|_{i,j,k-1/2}\left(P_{i,j,k}-P_{i,j,k-1}\right)}{\Delta z^2}=-\frac{1}{\mu}\frac{2\cdot k_x\big|_{i-1/2,j,k}P_{in}}{\Delta x^2}
\end{aligned} \tag{3.28}$$

Therefore, when *i* equals to 0, the corresponding elements in the matrix are the same as the inner grid blocks except G=0 and A is expressed as

$$A = -\frac{1}{\mu}\frac{2\cdot k_x\big|_{i-1/2,j,k}}{\Delta x^2} - \frac{1}{\mu}\frac{k_x\big|_{i-1/2,j,k}}{\Delta x^2} - \frac{1}{\mu}\frac{k_y\big|_{i,j-1/2,k}}{\Delta y^2} - \frac{1}{\mu}\frac{k_y\big|_{i,j+1/2,k}}{\Delta y^2} -$$

$$\frac{1}{\mu}\frac{k_z\big|_{i,j,k-1/2}}{\Delta z^2} - \frac{1}{\mu}\frac{k_z\big|_{i,j,k+1/2}}{\Delta z^2} \tag{3.29}$$

3. No flow exists on the side boundary.

When *j* equals to 0 or N_y-1, or *k* equals to 0 or N_z-1, it is considered to be on the side boundary. The matrix changes as follows. When *j* = 0, Eq. 3.5 is written as

$$\frac{1}{\mu}\frac{k_x\big|_{i+1/2,j,k}\left(P_{i+1,j,k}-P_{i,j,k}\right)-k_x\big|_{i-1/2,j,k}\left(P_{i,j,k}-P_{i-1,j,k}\right)}{\Delta x^2}$$

$$+\frac{1}{\mu}\frac{k_y\big|_{i,j+1/2,k}\left(P_{i,j+1,k}-P_{i,j,k}\right)}{\Delta y^2}$$

$$+\frac{1}{\mu}\frac{k_z\big|_{i,j,k+1/2}\left(P_{i,j,k+1}-P_{i,j,k}\right)-k_z\big|_{i,j,k-1/2}\left(P_{i,j,k}-P_{i,j,k-1}\right)}{\Delta z^2}=0 \tag{3.30}$$

and the corresponding elements in the coefficient matrix are calculated the same way as inner grid blocks except that E equals to 0 and the diagonal is expressed as

$$A = -\frac{1}{\mu}\frac{k_x\big|_{i+1/2,j,k}}{\Delta x^2} - \frac{1}{\mu}\frac{k_x\big|_{i-1/2,j,k}}{\Delta x^2} - \frac{1}{\mu}\frac{k_y\big|_{i,j-1/2,k}}{\Delta y^2} - \frac{1}{\mu}\frac{k_y\big|_{i,j+1/2,k}}{\Delta y^2} -$$

$$\frac{1}{\mu}\frac{k_z\big|_{i,j,k+1/2}}{\Delta z^2} \tag{3.31}$$

The coefficient elements for the other three side boundary cases are calculated similarly.

3.3.1.2 Generation of Right Side (RS)

According to the linear equations for determining pressure in each grid block, the RS is written as a vector shown in Figure 3.4.

The elements in the above vector are expressed as

$$B1 = \frac{1}{\mu}\frac{k_x\big|_{i-1/2,j,k}\left(-P_{in}\right)}{\Delta x^2} \tag{3.32}$$

the RS for grid blocks on the inlet boundary, and

$$B2 = \frac{1}{\mu}\frac{k_x\big|_{i+1/2,j,k}\left(-P\ \right)}{\Delta x^2} \tag{3.33}$$

represents the right side of the equations for grid blocks on the outlet boundary. All elements in the above vector corresponding to other grid blocks are 0.

A solver was developed for this linear equation system based on Gaussian elimination.

$$\begin{bmatrix} B1 \\ . \\ . \\ . \\ B1. \\ 0 \\ . \\ . \\ . \\ 0 \\ B2 \\ . \\ . \\ . \\ B2 \end{bmatrix}$$

Figure 3.4: The vector of the RS to solve the pressure equation.

3.3.2 CALCULATION OF HF CONCENTRATION DISTRIBUTION

There are two ways to solve Eq. 3.10 to obtain HF concentration distribution at each time step. One is an explicit form, in which HF concentration uses the value at time step *n* except in the time derivative. The other is an implicit form, in which all the acid concentrations in the equation use values at time step *n*+1. To make sure the calculation is stable, the implicit form is adopted here. It expressed as follows,

$$\left(\frac{\left(C_{D,1}\right)^{n+1}_{i,j,k} - \left(C_{D,1}\right)^{n}_{i,j,k}}{\Delta t_D}\right) + \frac{1}{\Delta x_D}\left(\left(u_{xD}\right)_{i+1/2,j,k}\left(C_{D,1}\right)^{n+1}_{i,j,k} - \left(u_{xD}\right)_{i-1/2,j,k}\left(C_{D,1}\right)^{n+1}_{i-1,j,k}\right)$$
$$+\frac{1}{\Delta y_D}\left(\left(u_{yD}\right)_{i,j+1/2,k}\left(C_{D,1}\right)^{n+1}_{i,j,k} - \left(u_{yD}\right)_{i,j-1/2,k}\left(C_{D,1}\right)^{n+1}_{i,j-1,k}\right)$$

$$+\frac{1}{\Delta z_D}\left(\left(u_{zD}\right)_{i,j,k+1/2}\left(C_{D,1}\right)_{i,j,k}^{n+1}-\left(u_{zD}\right)_{i,j,k-1/2}\left(C_{D,1}\right)_{i,j,k-1}^{n+1}\right)=\left(-\sum_{l=1}^{N_m}N_{Da,l}\Lambda_l C_{D,1}^{n+1}\right)_{i,j,k}$$

(3.34)

3.3.2.1 Generation of Coefficient Matrix

The coefficient matrix of Eq. 3.10 is also seven-band. It is generated the same way as calculating the pressure distribution. The general matrix can also be represented by Figure 3.3. However, the elements in this matrix are different from that for solving pressure.

For the inner grids, the corresponding elements in the matrix are

$$A=1+\frac{\Delta t_D}{\Delta x_D}\left(\frac{u_{xD}\big|_{i+1/2,j,k}}{2}-\frac{u_{xD}\big|_{i-1/2,j,k}}{2}\right)+\frac{\Delta t_D}{\Delta y_D}\left(\frac{u_{yD}\big|_{i,j+1/2,k}}{2}-\frac{u_{yD}\big|_{i,j-1/2,k}}{2}\right)$$

$$+\frac{\Delta t_D}{\Delta z_D}\left(\frac{u_{zD}\big|_{i,j,k+1/2}}{2}-\frac{u_{zD}\big|_{i,j,k-1/2}}{2}\right)+\left(\Delta t_D\sum_{l=1}^{N_m}N_{Da,l}\Lambda_l\right)_{i,j,k} \qquad (3.35)$$

$$B=\frac{\Delta t_D}{2\Delta z_D}u_{zD}\big|_{i,j,k+1/2} \qquad (3.36)$$

$$C=-\frac{\Delta t_D}{2\Delta z_D}u_{zD}\big|_{i,j,k-1/2} \qquad (3.37)$$

$$D=\frac{\Delta t_D}{2\Delta y_D}u_{yD}\big|_{i,j+1/2,k} \qquad (3.38)$$

$$E=-\frac{\Delta t_D}{2\Delta y_D}u_{yD}\big|_{i,j-1/2,k} \qquad (3.39)$$

$$F=\frac{\Delta t_D}{2\Delta x_D}u_{xD}\big|_{i+1/2,j,k} \qquad (3.40)$$

$$G = -\frac{\Delta t_D}{2\Delta x_D} u_{xD}\Big|_{i-1/2,j,k} \tag{3.41}$$

The dimensionless HF concentration is 1 at the inlet boundary. There is no element on the super-lower band for grid blocks on inlet boundary. In another word, G=0. The other items except A in the matrix are the same as in the inner grid blocks. A becomes

$$A = 1 + \frac{\Delta t_D}{\Delta x_D}\left(\frac{u_{xD}\big|_{i+1/2,j,k}}{2}\right) + \frac{\Delta t_D}{\Delta y_D}\left(\frac{u_{yD}\big|_{i,j+1/2,k}}{2} - \frac{u_{yD}\big|_{i,j-1/2,k}}{2}\right) +$$

$$\frac{\Delta t_D}{\Delta z_D}\left(\frac{u_{zD}\big|_{i,j,k+1/2}}{2} - \frac{u_{zD}\big|_{i,j,k-1/2}}{2}\right) + \left(\Delta t_D \sum_{l=1}^{N_m} N_{Da,l}\Lambda_l\right)_{i,j,k} \tag{3.42}$$

Assume there is no flow on the side boundary. For instance, if j = 0, Eq. 3.10 becomes:

$$\left(C_{D,1}\right)_{i,j,k}^{n+1} + \frac{\Delta t_D}{\Delta x_D}\left(\left(u_{xD}\right)_{i+1/2,j,k}\frac{\left(C_{D,1}\right)_{i+1,j,k}^{n+1} + \left(C_{D,1}\right)_{i,j,k}^{n+1}}{2} - \left(u_{xD}\right)_{i-1/2,j,k}\frac{\left(C_{D,1}\right)_{i-1,j,k}^{n+1} + \left(C_{D,1}\right)_{i,j,k}^{n+1}}{2}\right)$$

$$+ \frac{\Delta t_D}{\Delta y_D}\left(\left(u_{yD}\right)_{i,j+1/2,k}\frac{\left(C_{D,1}\right)_{i,j+1,k}^{n+1} + \left(C_{D,1}\right)_{i,j,k}^{n+1}}{2}\right)$$

$$+ \frac{\Delta t_D}{\Delta z_D}\left(\left(u_{zD}\right)_{i,j,k+1/2}\frac{\left(C_{D,1}\right)_{i,j,k+1}^{n+1} + \left(C_{D,1}\right)_{i,j,k}^{n+1}}{2} - \left(u_{zD}\right)_{i,j,k-1/2}\frac{\left(C_{D,1}\right)_{i,j,k-1}^{n+1} + \left(C_{D,1}\right)_{i,j,k}^{n+1}}{2}\right)$$

$$= \left(-\Delta t_D \sum_{l=1}^{N_m} N_{Da,l}\Lambda_l C_{D,1}^{n+1}\right)_{i,j,k} \tag{3.43}$$

Element E equals 0 in the matrix for grid blocks on a side boundary. The other corresponding elements in the matrix are calculated the same way as the inner grid blocks mentioned above except A.

$$A = 1 + \frac{\Delta t_D}{\Delta x_D}\left(\frac{u_{xD}\big|_{i+1/2,j,k}}{2} - \frac{u_{xD}\big|_{i-1/2,j,k}}{2}\right) + \frac{\Delta t_D}{\Delta y_D}\frac{u_{yD}\big|_{i,j+1/2,k}}{2} +$$

$$\frac{\Delta t_D}{\Delta z_D}\left(\frac{u_{zD}\big|_{i,j,k+1/2}}{2} - \frac{u_{zD}\big|_{i,j,k-1/2}}{2}\right) + \left(\Delta t_D \sum_{l=1}^{N_m} N_{Da,l}\Lambda_l\right)_{i,j,k} \tag{3.44}$$

3.3.2.2 Generation of Right Side

With the boundary condition at the inlet, $C_{D,1}\big|_{0,j,k} = 1$, the RS for grid blocks at the inlet are $\left(C_{D,1}\right)^n_{1,j,k} + \frac{\Delta t_D}{2\Delta x_D} u_{xD}\big|_{1/2,j,k}$. And for other grid blocks, the RS is $\left(C_{D,1}\right)^n_{i,j,k}$. It is represented in vector form as Figure 3.5, with

$$\begin{bmatrix} B1 \\ . \\ . \\ . \\ B1 \\ B2 \\ . \\ . \\ . \\ B2 \end{bmatrix}$$

Figure 3.5: The vector of the RS to solve the pressure equation.

B1= $\left(C_{D,1}\right)^{n}_{1,j,k} + \frac{\Delta t_D}{2\Delta x_D} u_{xD}\Big|_{1/2,j,k}$ (3.45)

B2= $\left(C_{D,1}\right)^{n}_{i,j,k}$ (3.46)

This linear equation system is also solved by Gaussian elimination.

3.3.3 CALCULATION OF H_2SiF_6 CONCENTRATION DISTRIBUTION

The procedure of calculating H_2SiF_6 concentration at each time step is the same with calculating HF concentration. However, because no H_2SiF_6 is injected at the inlet, the inlet boundary condition for solving this equation system is different from that for solving the HF distribution. The elements in the RS vector in this case become

B1= $\left(C_{D,2}\right)^{n}_{i,j,k} + \Delta t_D \left(\frac{v_5}{v_1} N_{Da,1} \Lambda_{1i,j,k} + \frac{v_6}{v_2} N_{Da,2} \Lambda_{2i,j,k} + \frac{v_7}{v_3} N_{Da,3} \Lambda_{3i,j,k} \right) \left(C_{D1}\right)^{n+1}_{i,j,k}$

(3.47)

B2= $\left(C_{D,2}\right)^{n}_{i,j,k}$ (3.48)

3.3.4 UPDATE OF PERMEABILITY

After the pressure field and acid concentrations in the core are calculated, the volume change of minerals in the rock can be easily obtained. Then the porosity will be updated explicitly by the following equation

$\phi_{i,j,k} = \phi^{0}_{i,j,k} + V_S \left(\Delta\Lambda_1 \cdot V_1 + \Delta\Lambda_2 \cdot V_2 + \Delta\Lambda_3 \cdot V_1 \right)$ (3.49)

Where V_s= Solid volume = (1- $\phi^{0}_{i,j,k}$)

V_1 = volume fraction for fast reacting mineral

V_2 = volume fraction for slow reacting mineral

The permeability is updated at each time step according to the Panda-Lake model [Panda and Lake, 1994], which takes into account physical properties of the rock, the statistics of particle size distribution, and effects of cementing materials. It is expressed as

$$k = \frac{\overline{D}_p^2 \phi^3 \left(\gamma C_{Dp}^3 + 3C_{Dp}^2 + 1\right)^2}{2\tau_e (1-\phi)^2 \left[6\left(1 + C_{Dp}^2\right)\left(1-\phi_u\right)/\left(1-\phi\right) + \left(\sum_{i=1}^{j} a_{vi} n_i\right) \overline{D}_p \left(\gamma C_{Dp}^3 + 3C_{Dp}^2 + 1\right)\right]^2} \tag{3.50}$$

Where $\overline{D}_p$ = mean particle diameter

C_{Dp} = coefficient of variation of particle diameter

τ_e = effective tortuosity

ϕ_u = porosity of the unconsolidated sand

j = total number of cementing minerals

n_i = volume fraction of cement i

The effective tortuosity and unconsolidated sand porosity are calculated respectively by the following equations.

$$\tau_e = \tau\left(1 + C_{Dp}^2\right)\left(1 + \frac{Rm_1}{1-m_1}\right)^2 \left[1 + \frac{2m}{(1-m)\phi_u^{0.33}}\right]^2 \tag{3.51}$$

$$\phi_u = \phi + \sum_{i=1}^{j} n_i (1-\phi) \tag{3.52}$$

$$m = \frac{1-\phi_u}{\phi_u} P_f \tag{3.53}$$

$$m_1 = \frac{1-\phi_u}{\phi_u} P_b \tag{3.54}$$

Where

P_f = volume fraction of pore-filling cement

P_b = volume fraction of pore-bridging cement

CHAPTER 4 GENERATING HETEROGENEOUS INITIAL POROSITY AND MINERALS

In sandstone matrix acidizing, heterogeneity in the local permeability distribution is a critical factor that affects the acid flow pattern in acid core flooding [Thomas et al., 2002^b]. When permeability is highly heterogeneous, instead of moving as piston, the acid may tend to proceed following preferential paths and create tiny channels. However, most sandstone acidizing models were built based on the assumption of homogeneous rock properties. To investigate the effect of heterogeneity and correlation of permeability on sandstone acid treatments, one important task of this project is to generate an initial heterogeneous permeability field.

Since the permeability of porous media is correlated with porosity and minerals in some way, instead of directly generating a permeability profile, initial porosity and mineral distributions are generated in this work. The Panda-Lake model is used to calculate permeability from the generated porosity and minerals.

The following sections will demonstrate methods to generate completely random porosity distributions, correlated porosity distributions, completely random mineral distributions, and correlated mineral distributions.

4.1 Generation of Completely Random Porosity Field

A normal distribution is a common distribution of random variables. Mean and standard deviation are two parameters that define a particular normal distribution. A porosity distribution can be generated from a given mean and standard deviation. To characterize the local porosity distribution in a sandstone core in this simulation, the core is divided into 8000 grid blocks. Each grid block is assigned a porosity value at the beginning of the simulation. These values constitute a set of normally distributed random numbers.

The Box-Muller method [Dagpunar, 1988] is used to generate a set of normally distributed random numbers. In this method, two random numbers, x and y, which are uniformly distributed between 0 and 1, are generated first. A middle variable s is calculated by

$$s = (2x-1)^2 + (2y-1)^2 \tag{4.1}$$

If $s > 1$, s is discarded and x and y are regenerated by the same way until s is equal to or less than 1. Then two Gaussian random numbers, R_1 and R_2, are calculated by the following equations,

$$R_1 = \sqrt{\frac{-2\log(s)}{s}}\,(2x-1) \tag{4.2}$$

$$R_2 = \sqrt{\frac{-2\log(s)}{s}}\,(2y-1) \tag{4.3}$$

Given the average porosity, $\bar{\phi}$, and the standard deviation of the porosity distribution, σ, the group of generated random numbers are converted to porosity values by

$$\phi = \bar{\phi} + R\sigma \tag{4.4}$$

where R is the group of random number generated by Box-Muller method. Then this porosity value is assigned to a grid block.

Figure 4.1 shows the histogram of a generated random porosity distribution with mean and standard deviation being 0.18 and 0.03, respectively. A histogram is a graphical display showing the distribution of data values in a sample by dividing the range of the data into equally spaced intervals and counting the number of values that fall into each interval. For a normal distribution, the histogram forms a bell-shaped curve and is symmetrical with respect to the mean.

The porosity of rocks usually is not completely randomly distributed but is spatially correlated. The correlation strength can be defined by the correlation scale parameter (λ). The histogram provides no information of the spatial order for the random porosity distribution in the core. Measures like mean and standard deviation are not sufficient to describe a correlated porosity distribution. Some other statistical tools are also required to demonstrate the spatial order of those random porosity values. Covariance, semi-variogram, spectral analysis through Fourier transforms, and R/S analysis, are four commonly used measures for this purpose [Hardy and Beier, 1994]. A semi-variogram is an important tool in geostatistics describing spatial correlation. It shows the changing of semi-variance with changing space distance and gives more information about heterogeneity that is important for predicting fluid flow in heterogeneous media. The semi-variance for lag distance *h* is defined as the average squared difference of values in two positions separated by *h*. For example, the semi-variance of porosity for lag *h* is expressed as

$$\gamma(h) = \frac{1}{2N_p} \sum_N \left(\phi_i - \phi_{i+h}\right)^2 \qquad (4.5)$$

where N_p is the number of sample pairs for lag *h*.

For a "stable" semi-variogram model, there is no oscillation of semi-variogram with increasing lag. When a variable is spatially correlated and its semi-variogram follows a stable model, $\gamma(h_1)$ is higher than $\gamma(h_2)$ if h_1 is higher than h_2.

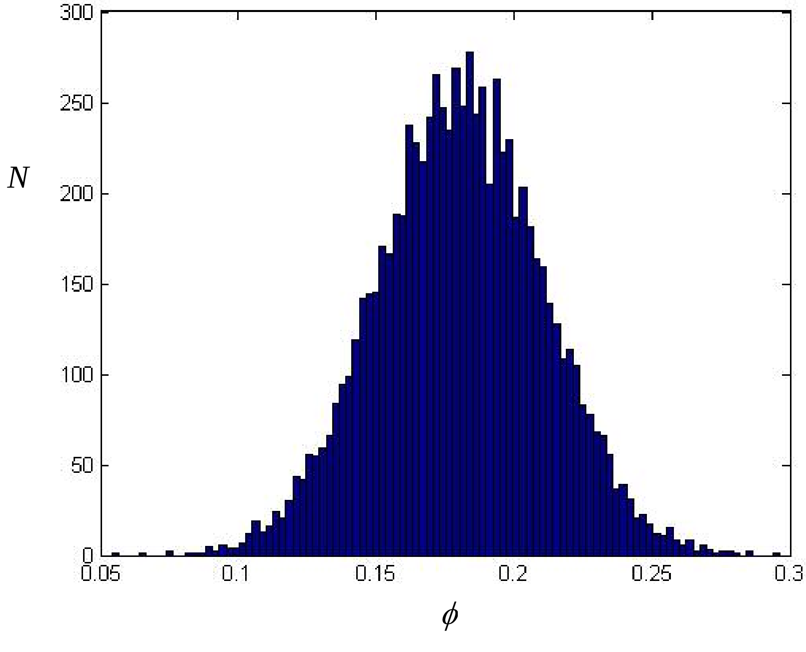

Figure 4.1: Histogram of porosity distributed (*N* is the number of grid blocks in each bin) (λ_x/L=0, λ_y/L=0, λ_z/L=0).

To compare with the correlated distribution that will be addressed later in this chapter, the semi-variogram for the sample illustrated in Figure 4.1 is also provided here. Since it varies in different directions, the semi-variograms of several porosity samples in the *x*, *y*, and *z* directions are plotted versus lag/L in Figures 4.2 - 4.4, respectively. It is apparent that the porosity semi-variance does not increase with lag distance in any direction, which indicates there is no correlation in any direction. A 3D visualization of the random porosity field is shown in Figure 4.5.

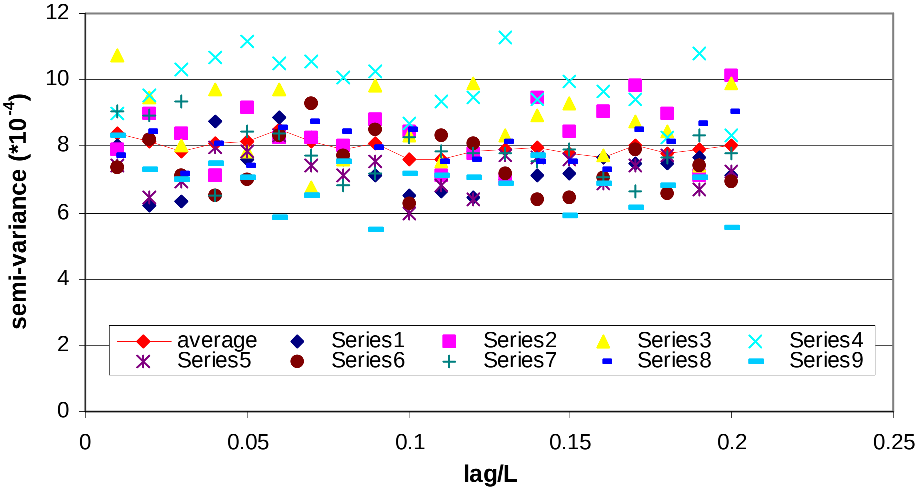

Figure 4.2: Semi-variogram of porosity distribution in the *x* direction (λ_x/L=0, λ_y/L=0, λ_z/L=0).

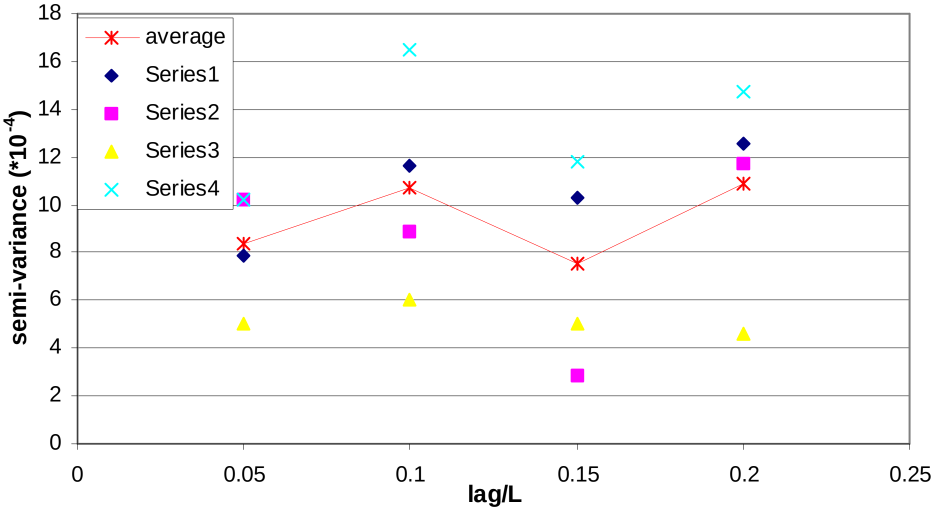

Figure 4.3: Semi-variogram of porosity distribution in the *y* direction (λ_x/L=0, λ_y/L=0, λ_z/L=0).

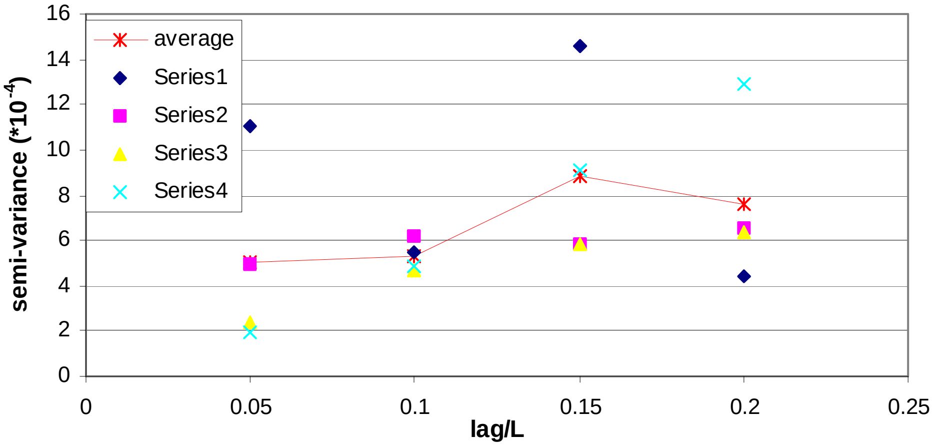

Figure 4.4: Semi-variogram of porosity distribution in the *z* direction (λ_x/L=0, λ_y/L=0, λ_z/L=0).

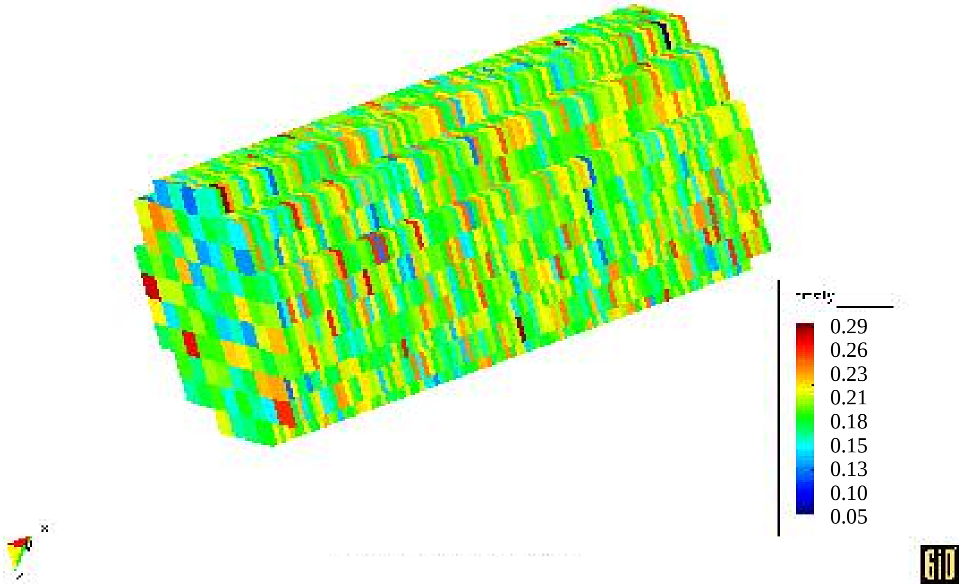

Figure 4.5: Completely random porosity distribution (λ_x/L=0, λ_y/L=0, λ_z/L=0).

4.2 Generation Of Correlated Porosity Distribution

In most reservoirs, permeability is not completely random. It usually is correlated to some degree in one or more directions. The correlated permeability has a great impact on the fluid flow in porous media. For example, a highly correlated permeability distribution in the main flow direction may result in flow channels where most fluid goes to high permeability layers but bypass the low permeability regions.

To simulate sandstone acidizing in spatially correlated cores, correlated porosity or mineral distribution were generated at the beginning of the simulations.

The permeability for each grid block is calculated according to the Panda-Lake model [Panda and Lake, 1994].

4.2.1 GENERATION OF CORRELATED RANDOM NUMBERS

In this work, the FFT (Fast Fourier Transform) simulator [Jennings, 2003] is adopted to generate correlated porosity distributions. It is a type of spectral method, which represents a synthetic field with a Fourier series. It generates a set of normally distributed random numbers with specified correlation strength. The mean of this group of random number is zero and its semi-variogram structure is specified in the input file.

In this work, a "stable" semi-variogram model is adopted, which is defined [Jennings, 2000] as

$$\gamma(h) = c\left\{1 - \exp\left[-(h/\lambda)^{\alpha}\right]\right\} \tag{4.6}$$

Where c is the sill, a constant maximum value beyond a certain lag that semi-variogram reaches; λ is the correlation scale parameter; and different α represents different semi-variogram type.

In the FFT input data file, the following parameters must be provided.

1. Run type. Run type being 1 should be specified to generate the group of random number, which forms a correlated distribution in three dimensions. Run types other than 1 produce no correlated random numbers but do some other tasks.

2. Seed. The built-in random number generator produces the same realization even when compiled on different computers. To obtain different distribution, the input value of the Seed should be changed in the input file.
3. Semi-variogram window. Use zero.
4. Size powers of arrays in x, y, and z direction. They are the powers to base 2 representing the number of grid blocks in x, y, and z direction, respectively.
5. Mesh spacing in x, y, and z direction.
6. Number of semi-variogram structures. Here 1 is used.
7. Semi-variogram type. Stable semi-variogram select 1, J-Bessel type semi-variogram selects 2, and k-Bessel type semi-variogram select 3.
8. Semi-variogram sill, c in Eq. 4.6
9. Coefficient α. α equals to 1 represents an exponential semi-variogram and equal to 2 represents a Gaussian semi-variogram.
10. Correlation scale parameter (λ in Eq. 4.6) in x, y, and z direction respectively. It can vary in different directions.

The simulator can be run with a Unix command like:*./fft_sim.exe < test.dat > test.out*, with *test.dat* being the input file and *test.out* being the output file containing the generated random numbers. The generated values are written to the output file in x, y, and z order. The output has a mean of zero and the variance that is specified in the input as sill.

For this particular project, the correlation scale parameters in the *x*, *y*, and *z* direction are the most important to generate the desired initial porosity distribution. They control the correlation strength in the three principle directions.

4.2.2 CONVERTING CORRELATED RANDOM NUMBER TO CORRELATED POROSITY DISTRIBUTION

The generated random numbers cannot be used directly to initialize the porosity distribution in the core. First of all, for a particular problem, the number of grid blocks in each direction may not be exactly a power of 2, which is required by FFT simulator. Secondly, the outputted data is in a single column. And thirdly, what FFT generated are just random numbers instead of porosity values. Therefore, to initialize the porosity distribution in a 3D core, several post processing steps are required to change this group of random numbers to porosity values and assign them to each grid block in the right order. A C++ program was developed to convert the random numbers to porosity distribution with specified mean and standard deviation, and then assign each grid block with the corresponding random number as its porosity.

Next, an example will be shown how to generate a correlated porosity field. First of all, use FFT to generate a group of correlated numbers for (128,16,16) grid blocks. The parameters in the input file are listed in Table 4.1, for a case that has the

Table 4.1: Input parameters for generating a correlated porosity field

Run Type	1	Semi-variogram window	0
Seed	1	Number of semi-variogram structure	1
Size power in x	7	Semi-variogram type	1
Size power in y	4	Semi-variogram sill	1
Size power in z	4	α	1
Mesh spacing in x (inches)	0.02	λ_x (inches)	20
Mesh spacing in y (inches)	0.1	λ_y (inches)	0.05
Mesh spacing in z (inches)	0.1	λ_z (inches)	1

strongest correlation in the *x* direction, then followed by the *y* direction. The *z* direction has the lowest correlation strength.

Figure 4.6 demonstrates the histogram of the generated correlated porosity distribution. Since some random numbers are discarded during post processing, it is not a perfect normal distribution but still can represent the porosity distribution in sandstone.

The porosity semi-variograms in different directions are usually not the same due to different correlation scale parameters. Figures 4.7 - 4.9 respectively show the semi-variograms of the above case in the *x*, *y*, and *z* direction. In each figure, the semi-variogram is the average of several porosity samples. Unlike the completely random distribution, the semi-variance of this case increases gradually with increasing lag in *x* direction because of the long-range correlation specified by the correlation scale parameter. Similarly, Figure 4.9 also displayed a steady increase of porosity semi-variance with increasing lag in *z* direction. In *y* direction, however, we cannot say that it is correlated even though the average semi-variance also increases with increasing lag (Figure 4.8). The reason is that there is no steady increasing of semi-variance and with only four points it is hard to determine if it is correlated or not. A 3D plot of the porosity distribution for this case is also provided in Figure 4.10. It clearly shows much stronger correlations in the *x* and the *z* direction than in the *y* direction. This kind of distribution can be used to simulate laminated cores.

According to the semi-variogram model (Eq. 4.6), the semi-variance with lags much higher than the correlation scale parameter in that direction should reach the input sill. For this case, we used very large correlation scale parameter compared to the core dimension. So in the semi-variogram plot, we cannot see the sill.

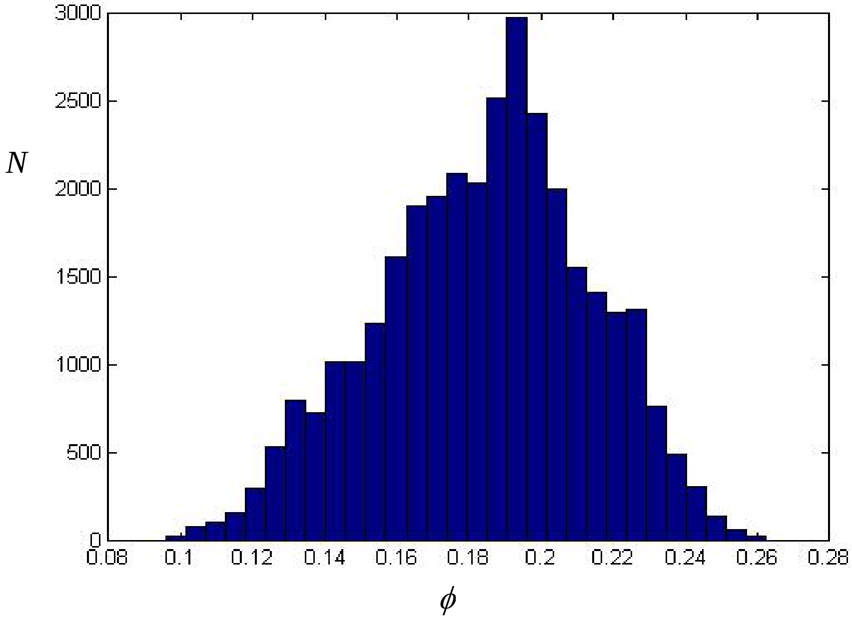

Figure 4.6: Histogram of porosity distribution (N is the number of grid blocks in each been) (λ_x/L=10, λ_y/L=0.025, λ_z/L=0.5).

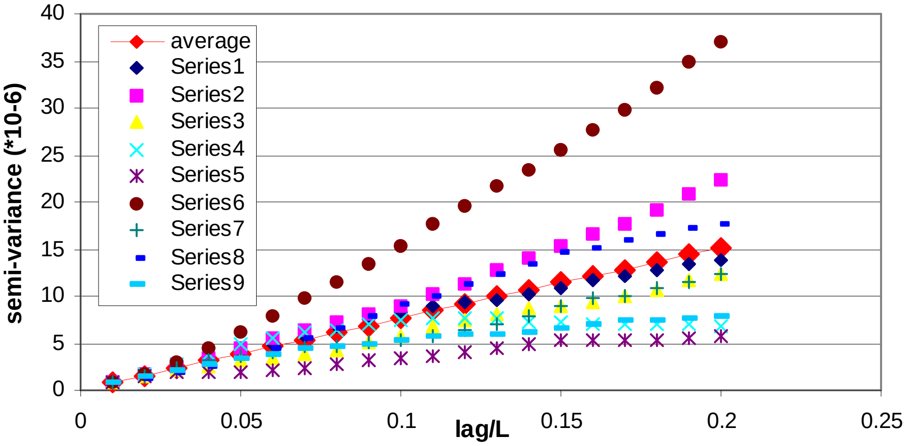

Figure 4.7: Semi-variogram of porosity distribution in the *x* direction (λ_x/L=10, λ_y/L=0.025, λ_z/L=0.5).

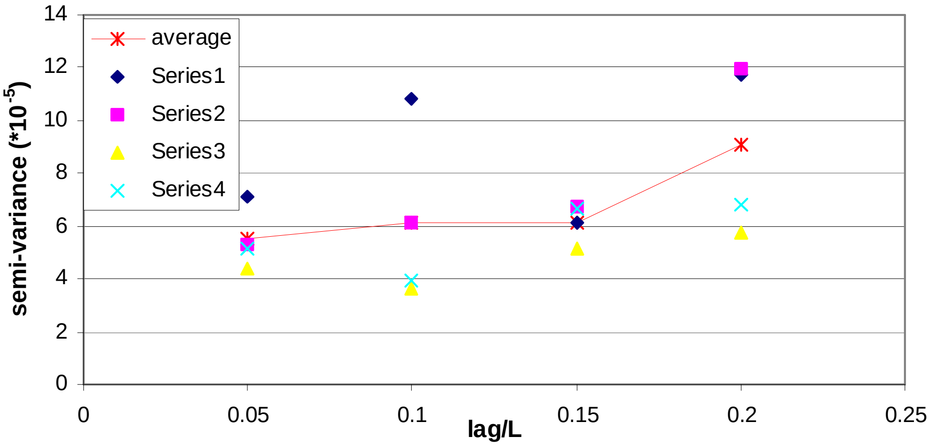

Figure 4.8: Semi-variogram of porosity distribution in the *y* direction (λ_x/L=10, λ_y/L=0.025, λ_z/L=0.5).

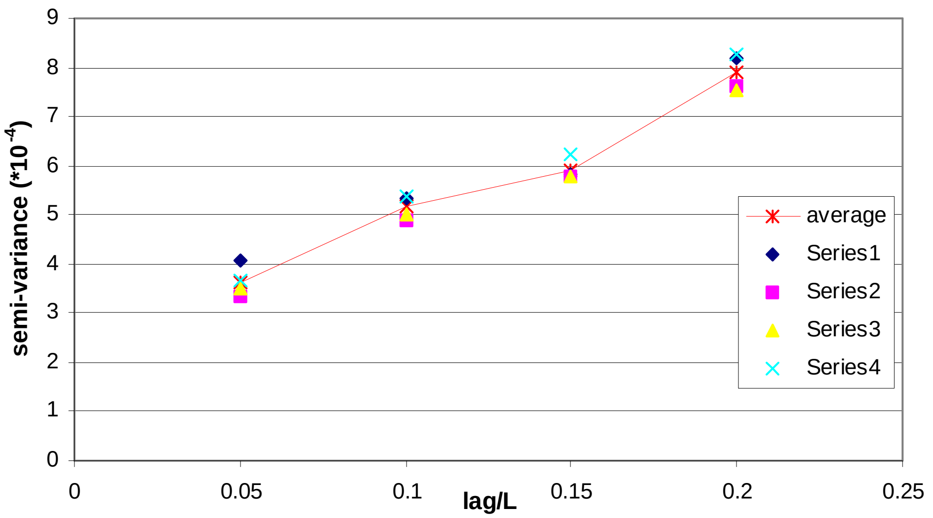

Figure 4.9: Semi-variogram of porosity distribution in the *z* direction (λ_x/L=10, λ_y/L=0.025, λ_z/L=0.5).

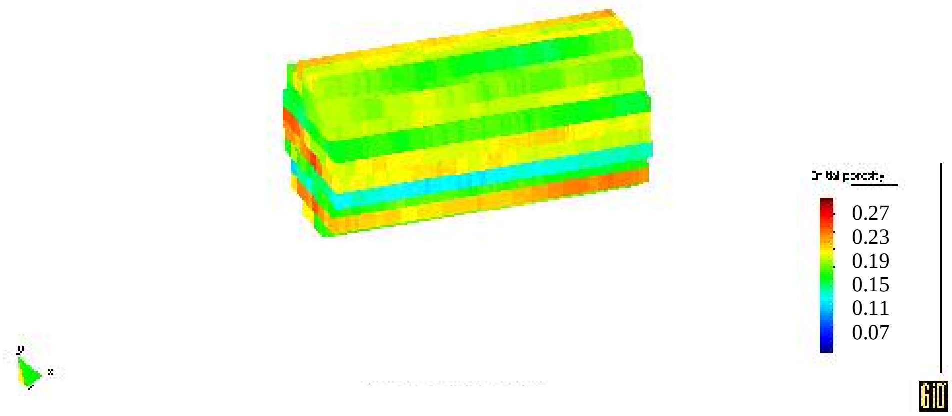

Figure 4.10: Porosity distribution (λ_x/L=10, λ_y/L=0.025, λ_z/L=0.5).

To get a better idea how the correlation scale parameter controls the correlation strength, two other correlated porosity realizations are generated to compare with the above one. One is to simulate a core with strong correlation in the *x* direction only. In this case, the correlation scale parameter in the *z* direction is set to 0.05 inch, the same as that in the *y* direction. To avoid a similar group of random numbers being generated, the seed is selected to be 2. Figure 4.11 shows the 3D plot for this case, which is made by a 3D visualization software, GID. It only differs from the previous realization in that it has no correlation in *z* direction. This kind of distribution is used to simulate cores with much stronger correlation in axial direction than in other two directions.

Another correlated porosity field is generated with weaker correlation in *x* direction by setting the correlation scale parameter to 1 inch. The Seed is set to 3 in this case. All other parameters are kept the same as the last case mentioned above. Figure 4.12 shows the 3D plot of this porosity distribution. The difference among these three cases can be clearly seen.

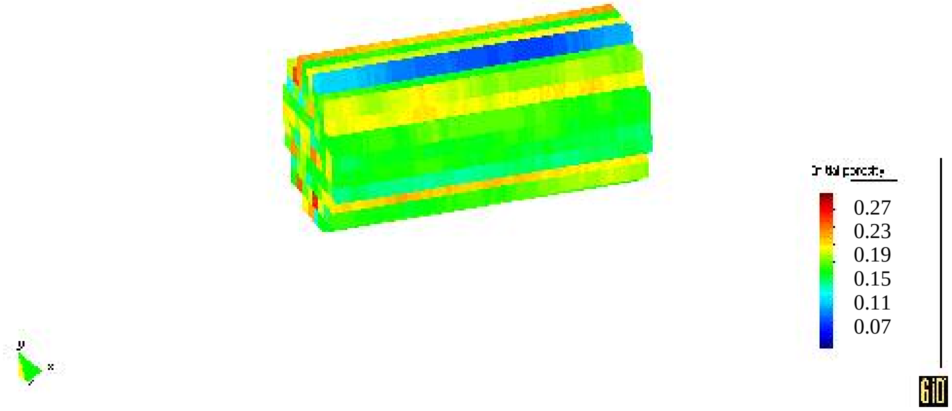

Figure 4.11: Porosity distribution (λ_x/L=10, λ_y/L=0.025, λ_z/L=0.025).

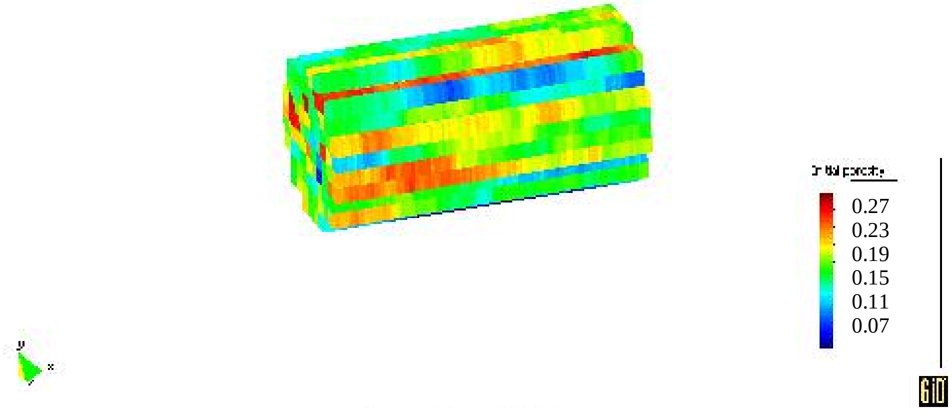

Figure 4.12: Porosity distribution (λ_x/L=1, λ_y/L=0.025, λ_z/L=0.025).

4.3 Generation of Random Mineral Distribution

In this work, the mineral is usually taken as having a uniform distribution [Lake, 2002]. A uniform distribution, or rectangular distribution, is a distribution that has constant probability. The probability density function, *P*, and cumulative distribution function, D, for a continuous uniform distribution on the interval [*a*, *b*] are:

$$P(x) = \begin{cases} 0 & x < a \\ 1/(b-a) & a < x < b \\ 0 & x > b \end{cases} \qquad (4.7)$$

$$D(x) = \begin{cases} 0 & x < a \\ (x-a)/(b-a) & a < x < b \\ 1 & x > b \end{cases} \qquad (4.8)$$

During the mineral initialization, the volume fraction of fast-reacting mineral is generated according to the above equations. Since carbonate is not the major component in sandstone, its volume fraction is taken as a constant everywhere in the core. Figure 4.13 is the histogram of a generated fast reacting mineral distribution in the core, in which *a* equals 0.09 and *b* equals 0.19. A 3D plot of the fast-reacting mineral distribution is shown in Figure 4.14.

4.4 Generation of correlated mineral distribution

The procedure to generate a correlated mineral distribution is the same as to generate a correlated porosity distribution using FFT. But the generated random

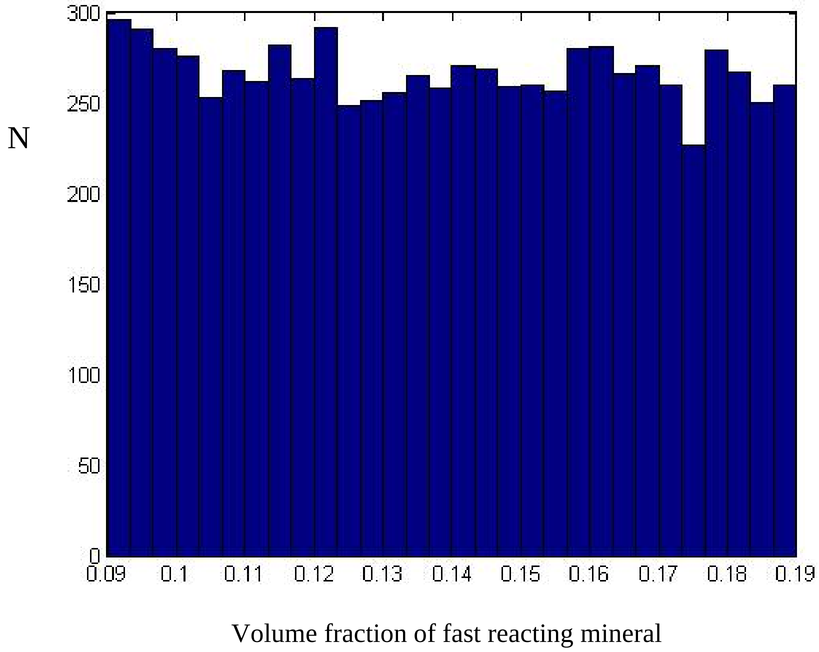

Figure 4.13: Histogram of the fast reacting mineral distribution (N is the number of grid blocks in each bin) (λ_x/L=0, λ_y/L=0, λ_z/L=0).

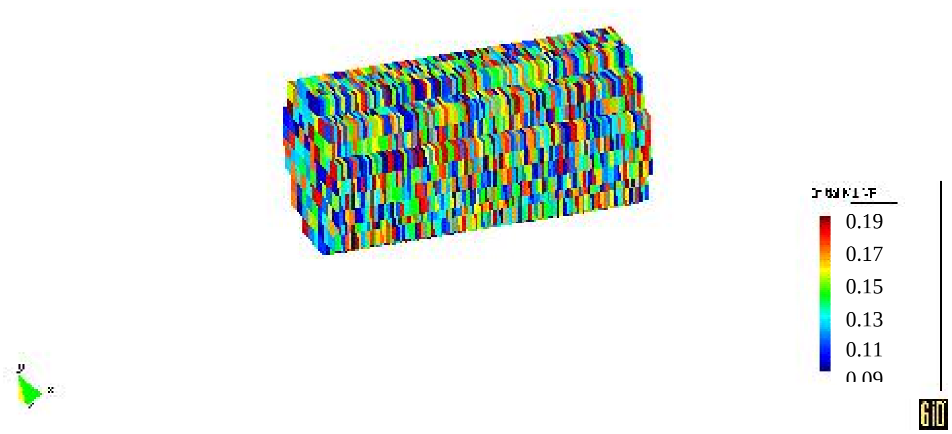

Figure 4.14: Fast reacting mineral distribution in a core (λ_x/L=0, λ_y/L=0, λ_z/L=0).

numbers are normally distributed. For this work, the goal to generate correlated mineral distribution is to study the effect of mineral correlation on acid flow pattern in sandstone acidizing. So it is convenient to use normally distributed mineral here since it can also achieve this purpose. Figure 4.15 is a 3D visualization of the fast-reacting mineral distribution generated by the simulator combined with FFT software.

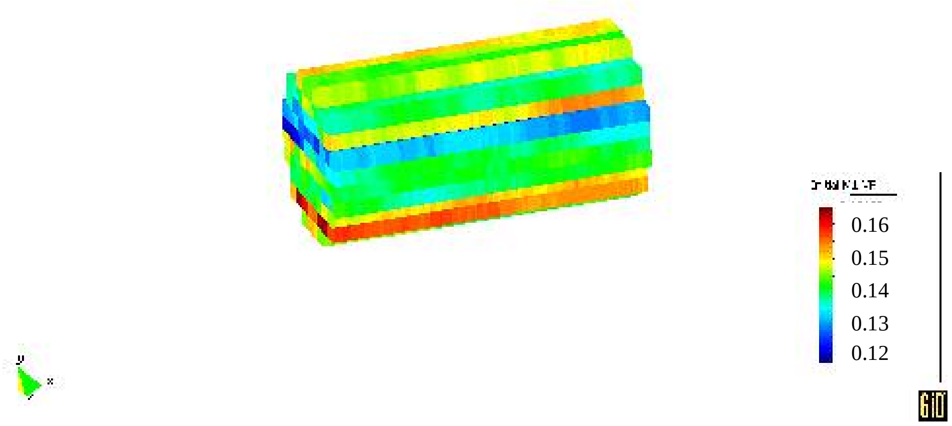

Figure 4.15: Fast-reacting mineral distribution (λ_x/L=10, λ_y/L=0.025, λ_z/L=0.5).

CHAPTER 5 RESULTS AND DISCUSSION

In this work, the fine-scale acidizing simulator was used to study the effects of heterogeneities in both the porosity/permeability field and in the distribution of minerals. The validation of this simulator is provided in Appendix B. We simulated a core flood experiment using a 1-inch diameter, 2-inch long core so that results could be compared with laboratory experiments. A series of simulations were also run to investigate the effects of fast reacting mineral content and acid concentration on sandstone acidizing. In the cases studied, the mean properties of the core and other acidizing conditions were identical and are given in Table 5.1. All the cases and their differences from input parameters specified in Table 5.1 are listed in Table 5.2.

In this chapter, the results for the following four cases are discussed in detail: a homogeneous case (Case 1); random porosity (different σ) with uniform mineral (Case 2 ~ 5); correlated porosity field with uniform mineral (Case 6 ~ 9); random mineral with homogeneous porosity (Case 10); correlated mineral with homogeneous porosity field (Case 11); both porosity and minerals are randomly distributed (Case 12); large original content of fast reacting mineral (Case 13); and large acid concentration (Case 14).

Table 5.1: Parameters used in simulation

Core length (inch)	2	Injected HCl concentration (wt%)	6
Core diameter (inch)	1	Injected HF concentration (wt%)	6
Average porosity	0.08	Acid viscosity (mPa-s)	0.89
Injection rate (ml/hr)	300	Density of M3 (kg/m^3)	740
Dissolving power (HF-M1) (Mass of M1 dissolved/mass of HF reacted)	0.486	Dissolving power (HF-M3) (Mass of M3 dissolved/mass of HF reacted)	0.8
Dissolving power (HF-M2) (Mass of M2 dissolved/mass of HF reacted)	0.5	Dissolving power (H_2SiF_6-M1) (Mass of M1 dissolved/mass of H_2SiF_6 reacted)	2.47
Specific surface area of slow reacting mineral (m^2/m^3)	300000	Specific surface area of silica gel (m^2/m^3)	3.30E+05
Temperature (K)	368	Density of acid (kg/m^3)	1075
Density of M2 (kg/m^3)	2650	Initial Average volume fraction of M1	0.04
Density of M1 (kg/m^3)	2600	Initial Average volume fraction of M2	0.95
Specific surface area of fast reacting mineral (m^2/m^3)	235000	Initial Average volume fraction of carbonate	0.01

Table 5.2: Summary of simulation cases

Cases	Description
Case 1	Homogeneous porosity and minerals. Basic parameters as Table 5-1
Case 2	Homogeneous minerals, σ of porosity is 0.01
Case 3	Homogeneous minerals, σ of porosity is 0.03
Case 4	Homogeneous minerals, σ of porosity is 0.05
Case 5	Homogeneous minerals, σ of porosity is 0.07
Case 6	λ_x of porosity equals to 20 inch
Case 7	λ_x of porosity equals to 10 inch
Case 8	λ_x of porosity equals to 4 inch
Case 9	λ_x of porosity equals to 2 inch
Case 10	Random minerals, homogeneous porosity
Case 11	Correlated minerals and homogeneous porosity
Case 12	Heterogeneous porosity and heterogeneous minerals
Case 13	Large content of fast reacting mineral
Case 14	Large HF/HCl concentration

5.1 Influence of Heterogeneous and/or Correlated Distribution of Rock Properties

5.1.1 HOMOGENEOUS POROSITY AND MINERAL DISTRIBUTION

In order to compare with the predictions of standard acidizing simulators, a base case, Case 1, is simulated in which the initial porosity, permeability, and mineral compositions were assumed constant throughout the core. For this condition, the problem simplifies to one-dimensional flow in the *x* direction. Table 5.1 listed all the required input parameter in this simulation. The rate constants and dissolving power used here are determined based on the Damkohler number da Motta adopted to fit Lindsay's test data [da Motta et al., 1992]. However, if possible, it is better to determine these values from particular tests.

Figure 5.1 illustrates the pressure response for this homogeneous core acid flooding. During the whole process of acid flooding simulation, the pressure drop decreases gradually.

A convenient way to visualize the effect of the acid on the rock matrix is to plot the change in porosity ($\Delta\phi$) caused by acid dissolution and/or precipitation of reaction products. Figures 5.2 - 5.5 present 3D images of $\Delta\phi$ after 5, 15, 25, and 35 pore volumes (PV) of acid injection, respectively. In these images, the visible face of the core on the left side of the image is the inlet face of the core. We see that for this

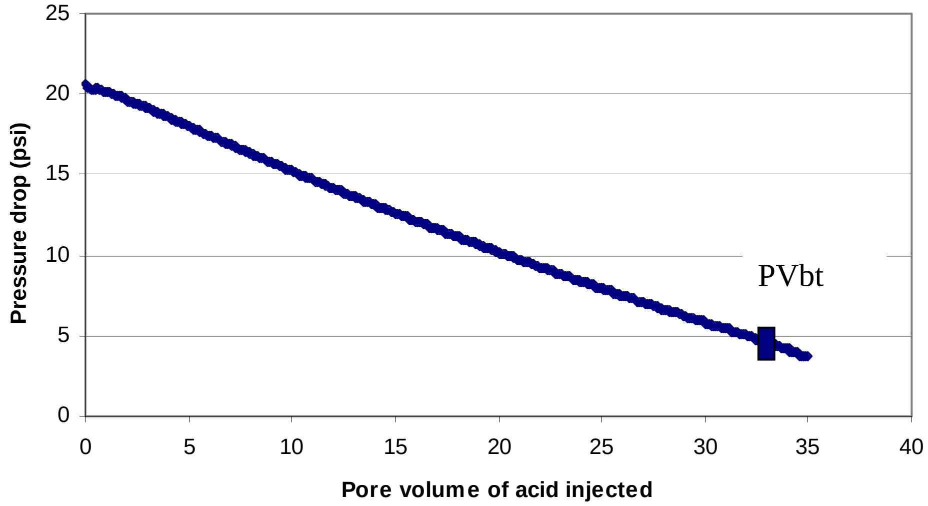

Figure 5.1: Pressure response during acid core flooding in simulation. (PVbt is the pore volume at which acid breaks through)

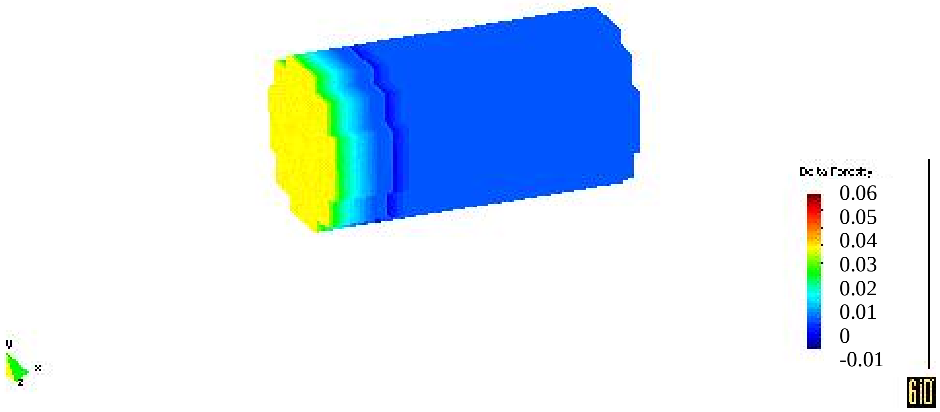

Figure 5.2: Δϕ distribution for the homogeneous case after 5 PV of acid injection.

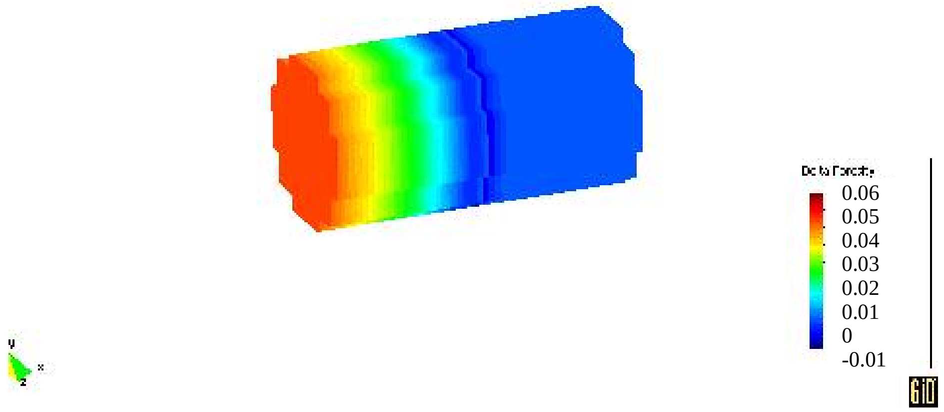

Figure 5.3: $\Delta\phi$ distribution for the homogeneous case after 15 PV of acid injection.

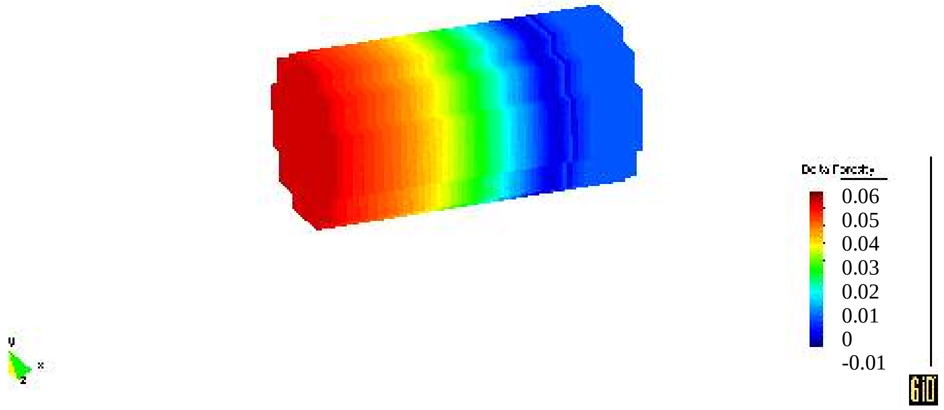

Figure 5.4: $\Delta\phi$ distribution for the homogeneous case after 25 PV of acid injection.

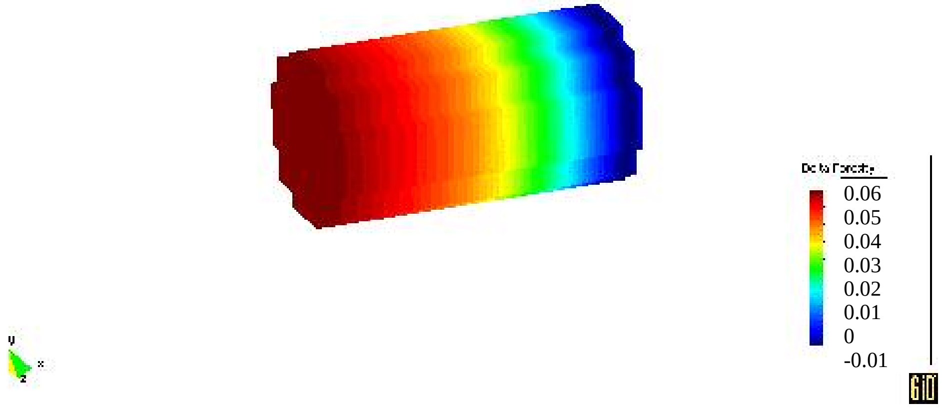

Figure 5.5: $\Delta\phi$ distribution for the homogeneous case after 35 PV of acid injection.

homogeneous case, the acid is uniformly altering the porosity of the core, with the region of increased porosity gradually moving through the core. Also notice that a zone of precipitated reaction products, $Si(OH)_4$, is being created ahead of the live acid, as indicated by the negative values of net porosity towards the exit end of the core.

The acid front uniformly moves in the core. By the time 35 PV of acid have been injected into the core, live acid is being produced from the core, as is shown in a HF concentration profile in Figure 5.6. To compare the amount of acid needed to penetrate live acid through the core, we define the pore volume of acid to breakthrough (PVbt) as being the volume injected in pore volumes at the time that the acid effluent concentration reached 10% of the injected concentration. For the homogeneous case, the pore volume of breakthrough was about 34.

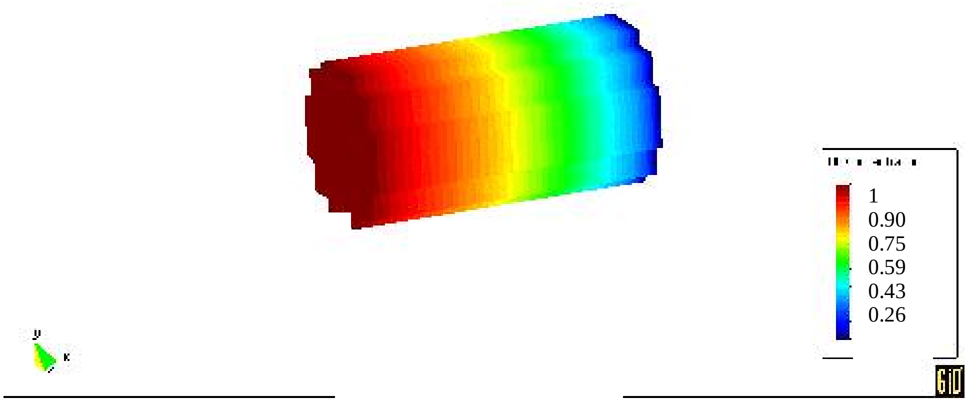

Figure 5.6: HF dimensionless concentration at 35 PV for the homogeneous case.

From the HF distribution, we can also see that the acid front spreads over a zone, which is about one half of the core length at 35 PV of acid injection. This verifies that chemical reaction caused much more spread of acid front than dispersion. So the assumption of no dispersion is valid in this problem.

Figures 5.7 – 5.10 illustrate the permeability distribution at different stages for this homogeneous case. Permeability uniformly decreases down to the exit end of the core. No preferential flow path is created in this case.

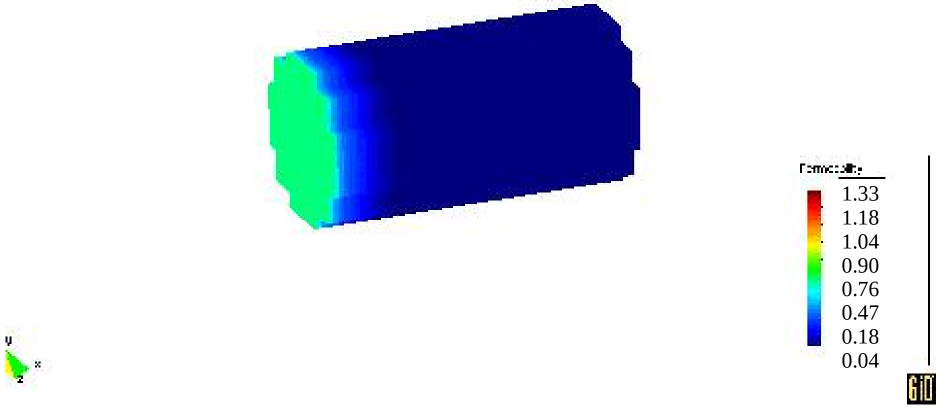

Figure 5.7: Permeability (Darcy) distribution for the homogeneous case after 5 PV of acid injection.

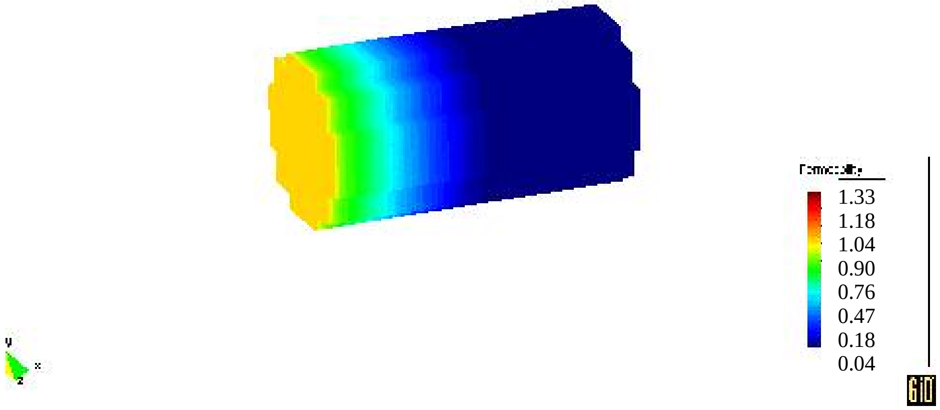

Figure 5.8: Permeability (Darcy) distribution for the homogeneous case after 15 PV of acid injection.

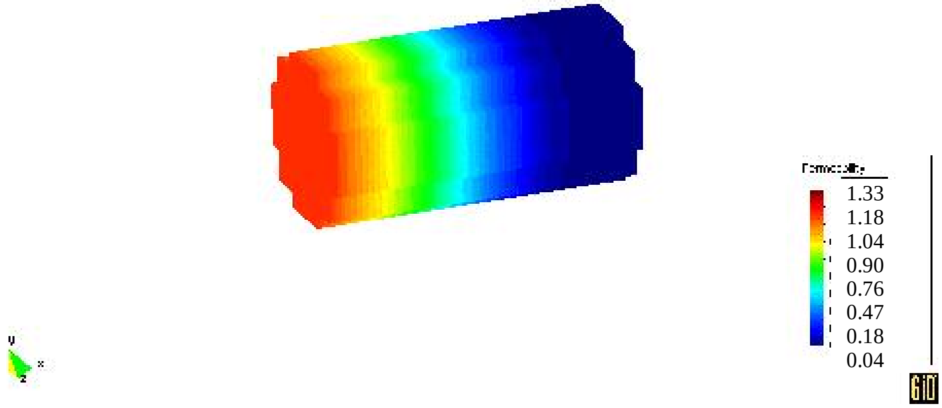

Figure 5.9: Permeability (Darcy) distribution for the homogeneous case after 25 PV of acid injection.

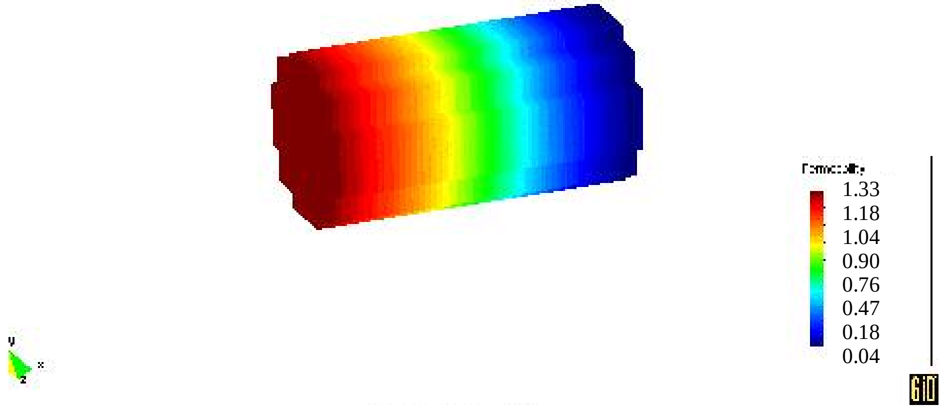

Figure 5.10: Permeability (Darcy) distribution for the homogeneous case after 35 PV of acid injection.

5.1.2 HETEROGENEOUS POROSITY AND HOMOGENEOUS MINERALS

Cases 2 - 5 are simulated to study the effect of randomly distributed porosity heterogeneity on sandstone acidizing. Different standard deviations (σ) of 0.01, 0.03, 0.05, and 0.07 are used in Cases 2 – 5, respectively. For all of these four cases, the mineral distribution is assumed to be homogenous and all other parameters are kept the same as Case 1, the homogeneous case. The only difference in these cases is the standard deviation of porosity distribution.

To compare with the homogeneous case, the porosity change distribution of Case 4 after 5, 15, 25, and 35 PV of acid injection are plotted in Figures 5.11 - 5.14. These plots only show grid blocks with $\Delta\phi$ higher than 0.02. This is because the $\Delta\phi$ plot without cutoff cannot show the non-uniform HF penetration very well (Figure. 5.15). Compared with Case 1, it is clear that acid has penetrated further through this heterogeneous core than for the corresponding homogeneous case with same volume of acid injection.

The dimensionless HF concentration distributions for this case (Figures 5.16 - 5.19) also show that live acid has penetrated much farther in the heterogeneous case than in the homogeneous case. Figure 5.17 shows that the acid front almost reached the end of the core in parts of the core after 15 PV of acid was injected, while in the homogeneous case, acid had penetrated only about half way through the core after 15 PV of acid injection. In the heterogeneous core, the acid finds its way through the more permeable pathways, requiring less acid to propagate a given distance.

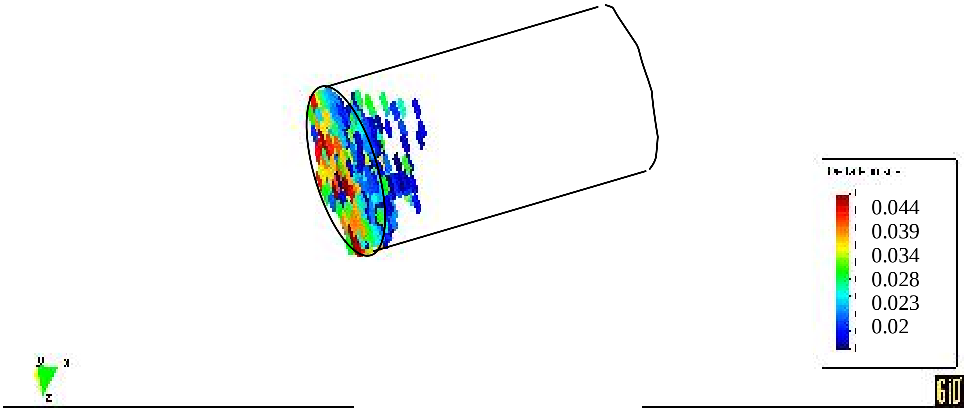

Figure 5.11: Δϕ distribution (Δϕ>0.02) for heterogeneous porosity (σ=0.05) and homogeneous minerals case (5 PV).

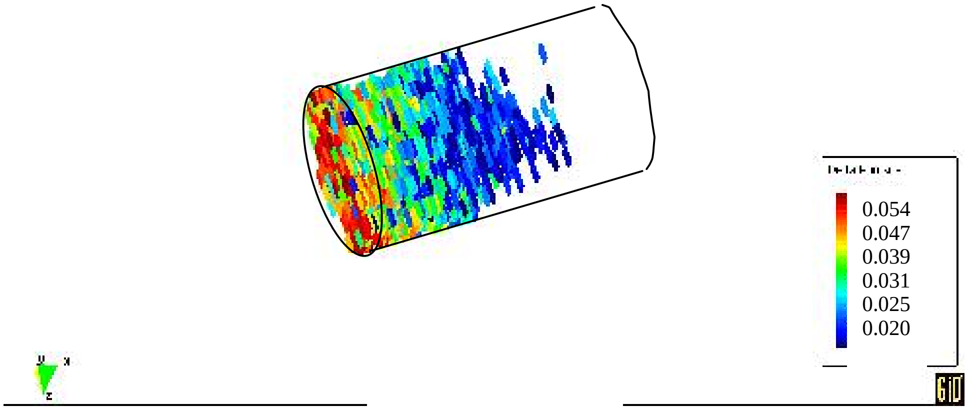

Figure 5.12: Δϕ distribution (Δϕ>0.02) for heterogeneous porosity (σ=0.05) and homogeneous minerals case (15 PV).

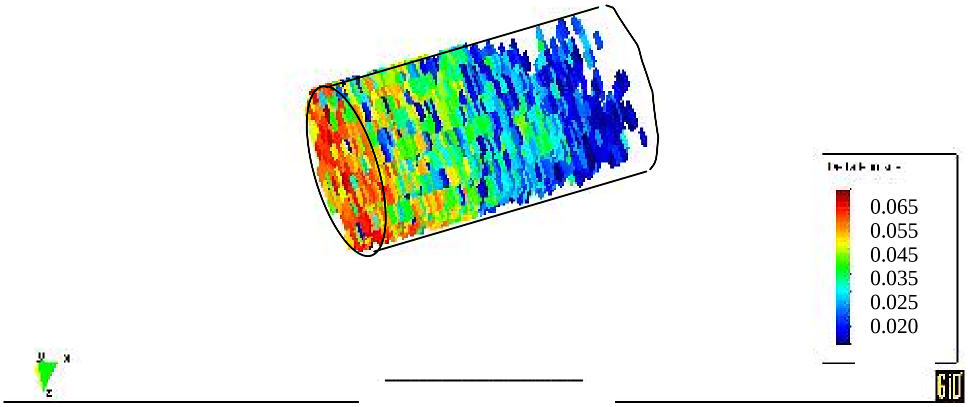

Figure 5.13: Δϕ distribution (Δϕ>0.02) for heterogeneous porosity (σ=0.05) and homogeneous minerals case (25 PV).

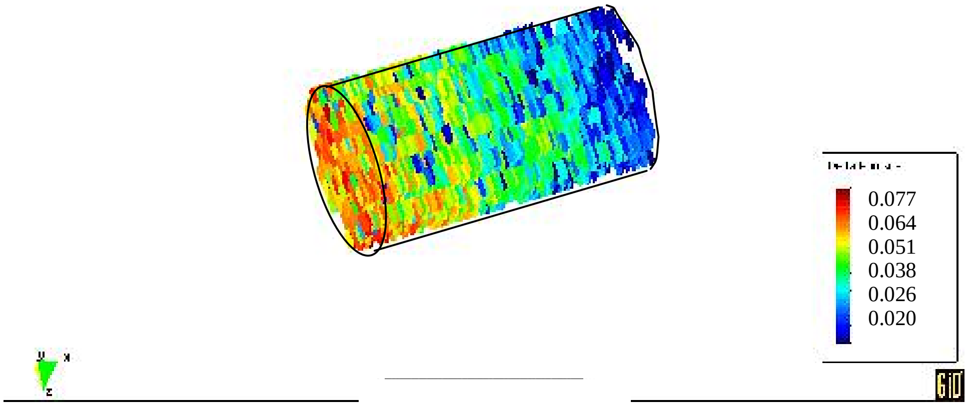

Figure 5.14: Δϕ distribution (Δϕ>0.02) for heterogeneous porosity (σ=0.05) and homogeneous minerals case (35 PV).

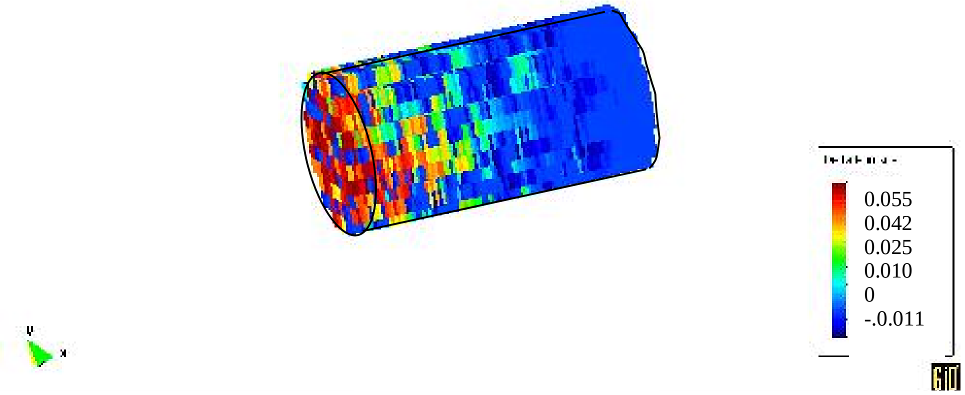

Figure 5.15: Δϕ distribution (without cutoff) for heterogeneous porosity (σ=0.05) and homogeneous minerals case (15 PV).

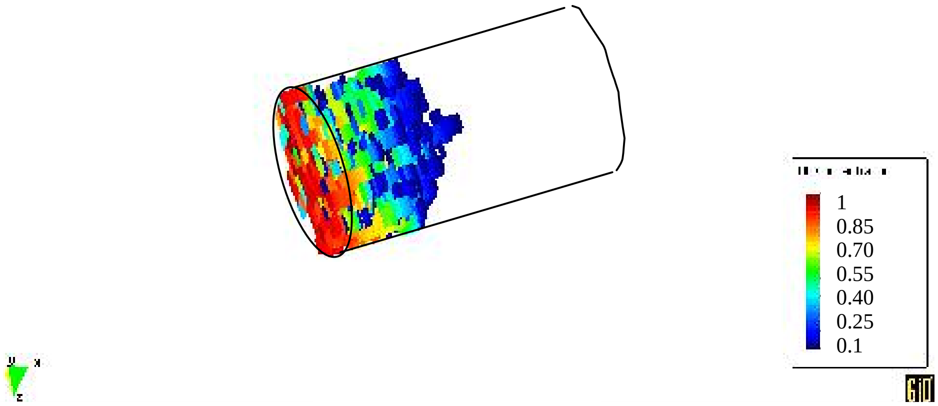

Figure 5.16: Dimensionless HF concentration distribution for heterogeneous porosity (σ=0.05) and homogeneous minerals case (5 PV).

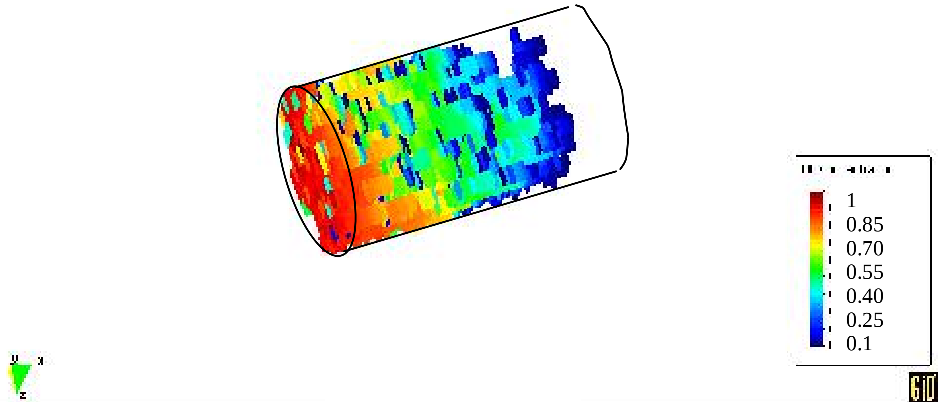

Figure 5.17: Dimensionless HF concentration distribution for heterogeneous porosity (σ=0.05) and homogeneous minerals case (15 PV).

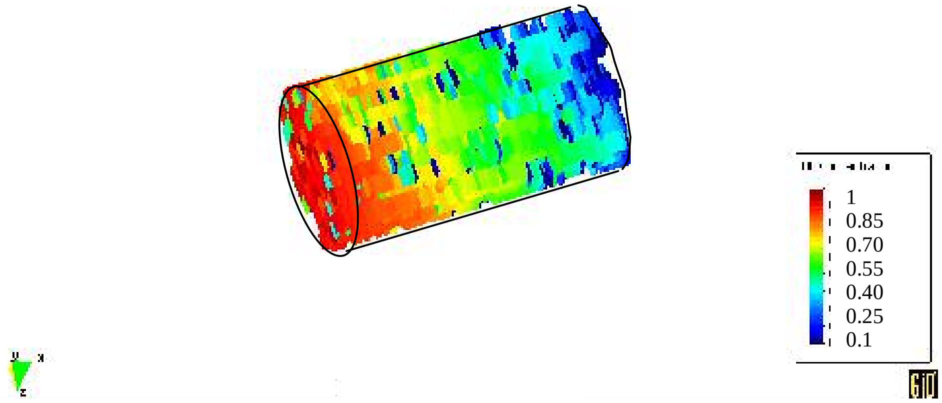

Figure 5.18: Dimensionless HF concentration distribution for heterogeneous porosity (σ=0.05) and homogeneous minerals case (25 PV).

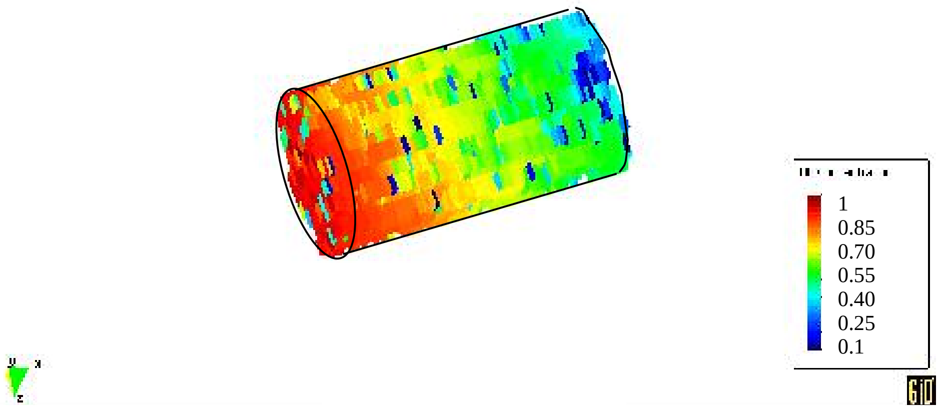

Figure 5.19: Dimensionless HF concentration distribution for heterogeneous porosity (σ=0.05) and homogeneous minerals case (35 PV).

The non-uniform flow of acid in heterogeneous core is also demonstrated by the fast reacting mineral distribution after some time of injection. Because the initial fast reacting mineral content is homogeneous, the dimensionless mineral content will be 1 or close to 1 in some places behind the acid front if the acid bypassed that area. Figures 5.20 - 5.23 illustrate the fast reacting mineral distribution higher than 0.1 after 15 PV acid injection. We can see that for cases with higher standard deviation than 0.05, even at the inlet, there are some places where the dimensionless concentration of fast reacting mineral is close to 1 after 15 PV of acid injection, while in Case 2 (σ = 0.01), all of the fast reacting mineral has been removed at the inlet. This supports the hypothesis that acid propagates through some preferred paths and creates channels

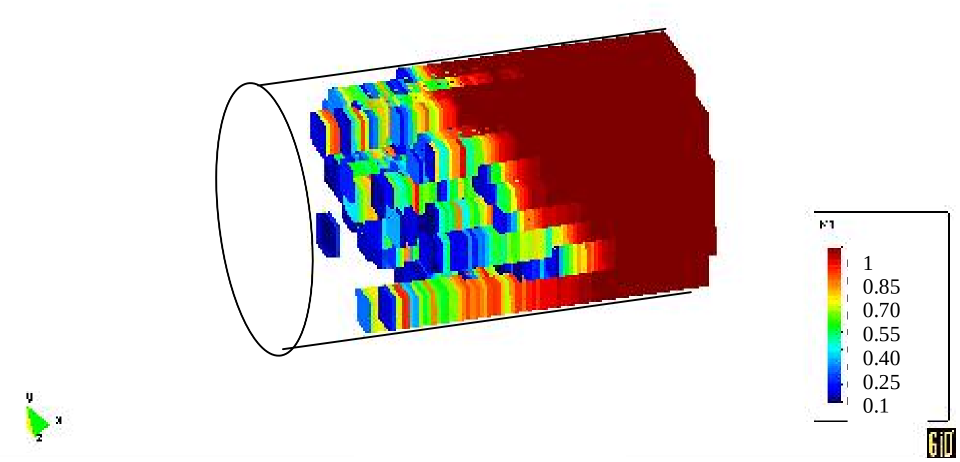

Figure 5.20: Distribution of dimensionless concentration of fast reacting mineral after 15 PV of acid injection. (σ=0.01).

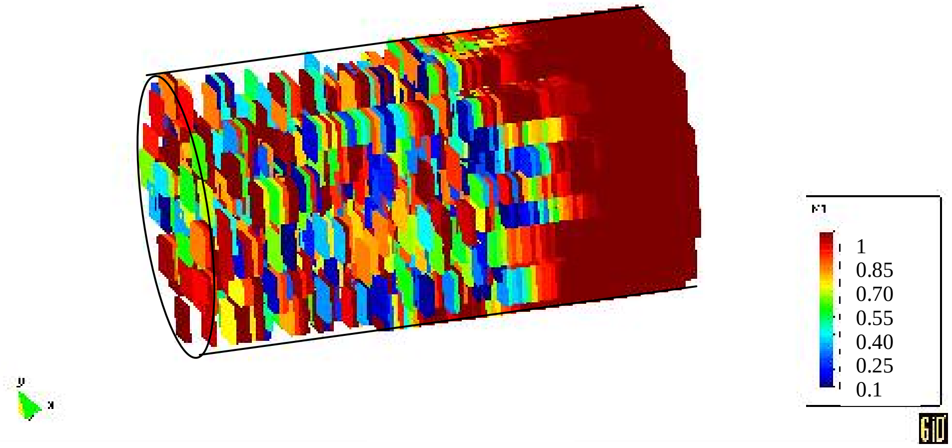

Figure 5.21: Distribution of dimensionless concentration of fast reacting mineral after 15 PV of acid injection. (σ=0.03).

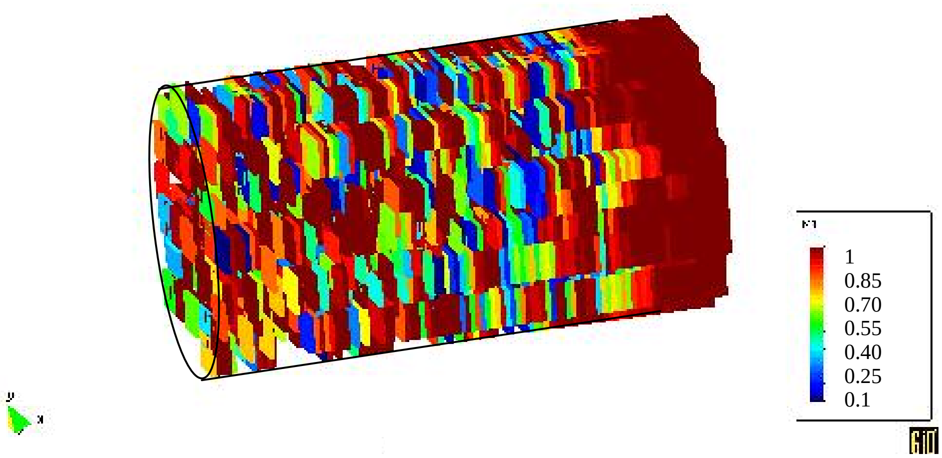

Figure 5.22: Distribution of dimensionless concentration of fast reacting mineral after 15 PV of acid injection. (σ=0.05).

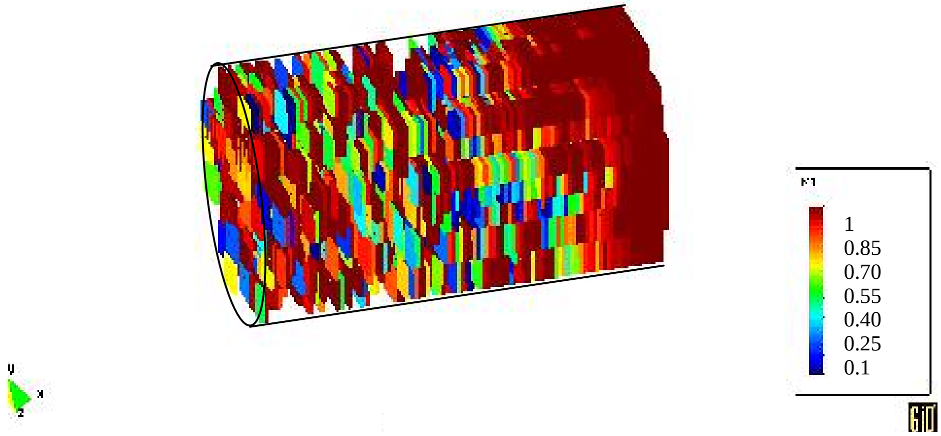

Figure 5.23: Distribution of dimensionless concentration of fast reacting mineral after 15 PV of acid injection. (σ=0.07).

in the core when the porosity distribution is heterogeneous. Case 2 shows more uniform dissolution of the fast-reacting minerals at the inlet than the other three cases. With the increase of standard deviation, more fast-reacting mineral is left undissolved behind the acid front while the acid penetrates further in the core.

The velocity profile is a direct indicator of acid flow pattern in sandstone cores. Figure 5.20 shows the distribution of dimensionless velocity higher than 4 in Case 5, whose standard deviation is 0.05. Several main flowing paths have been established after 35 PV of acid injection and flow concentrated to some particular parts of the core.

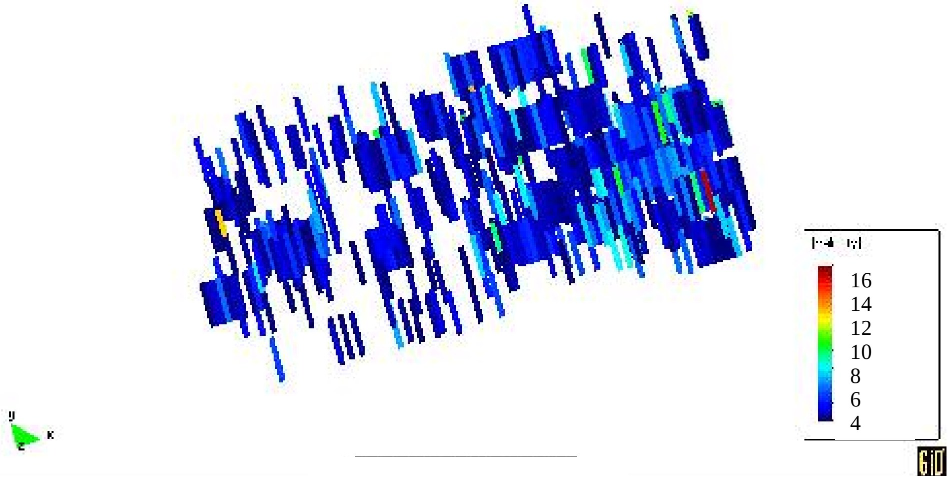

Figure 5.24: Dimensionless velocity distribution (higher than 4) of acid in the core after 35-PV of acid injection (σ=0.05).

The permeability responses for four random porosity fields with different standard deviations are compared with the response of a homogeneous core (σ = 0) in Figure 5.25. The overall mean permeability increases more rapidly and reaches a higher value in the cases with higher standard deviation of the porosity distribution.

Another measure of the efficiency of acidizing is the pore volume to breakthrough. Figure 5.26 shows the amount of acid needed to propagate live acid through the core decreased as the standard deviation increased. The acid breaks through in the homogeneous case more than 10 PV later than in heterogeneous sandstone core. Generally, the pore volume of acid necessary to break through decreases with increasing standard deviation, which indicates that heterogeneity of

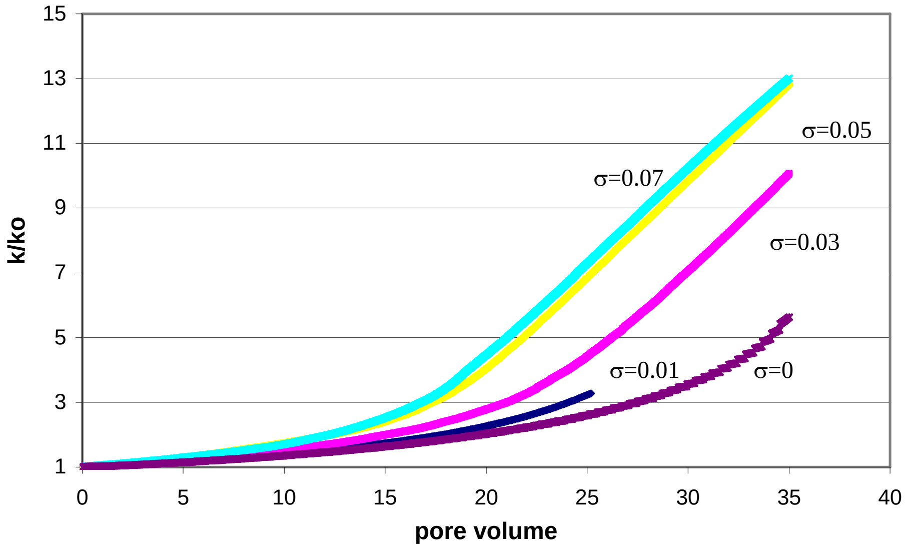

Figure 5.25: Permeability evolution for random porosity cases and homogeneous porosity case.

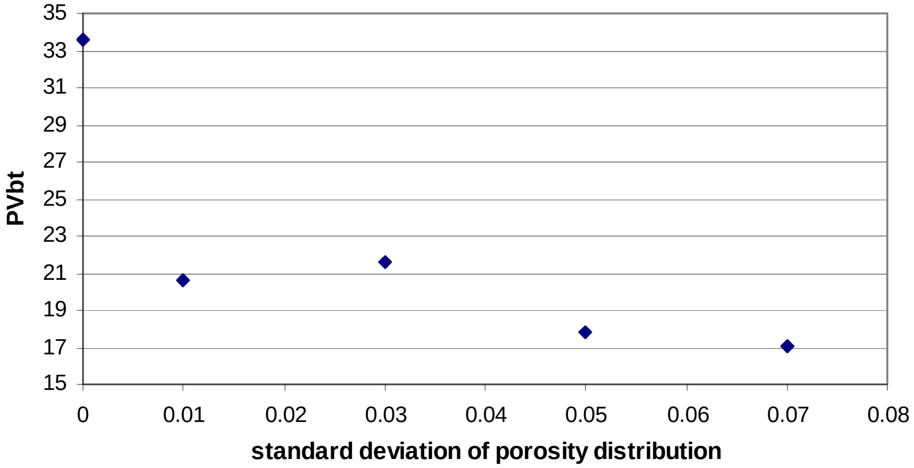

Figure 5.26: Acid breakthrough volume for random porosity cases and homogeneous porosity case.

porosity are helpful for creating channels and that acid propagates further in more heterogeneous porosity fields. In general, a high degree of heterogeneity of porosity/permeability increases the distance to which a given volume of acid can propagate in sandstone acidizing.

5.1.3 CORRELATED POROSITY DISTRIBUTION AND HOMOGENEOUS MINERAL DISTRIBUTION

To test the influence of correlation strength on acid flow pattern and dissolution, we ran four cases (Cases 6 ~ 9) with different correlation scale parameters in the main flowing direction. Figures 5.27 and 5.28 are the initial distributions of porosity for Case 6 and Case 9. Figure 5.27 shows the porosity profile with a higher correlation scale parameter in the *x* direction (20 inches). Figure 5.24 is the porosity distribution generated by setting a lower correlation scale parameter in the *x* direction (2 inches). Different from the uncorrelated random distribution cases, the layers with different porosity are very clear in the figures, and the differences between these two cases are also apparent.

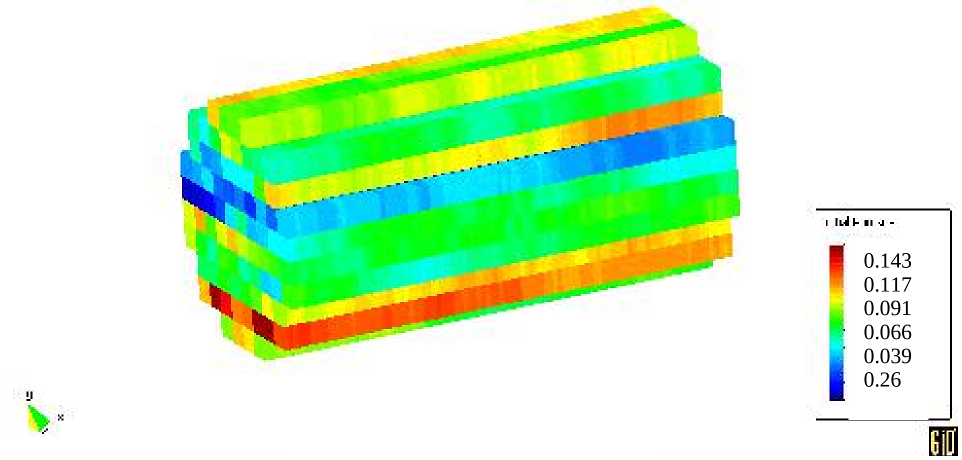

Figure 5.27: Initial porosity distribution in a core. (Case 6: λ_x/L=10, λ_y/L=0.025, λ_z/L=0.5).

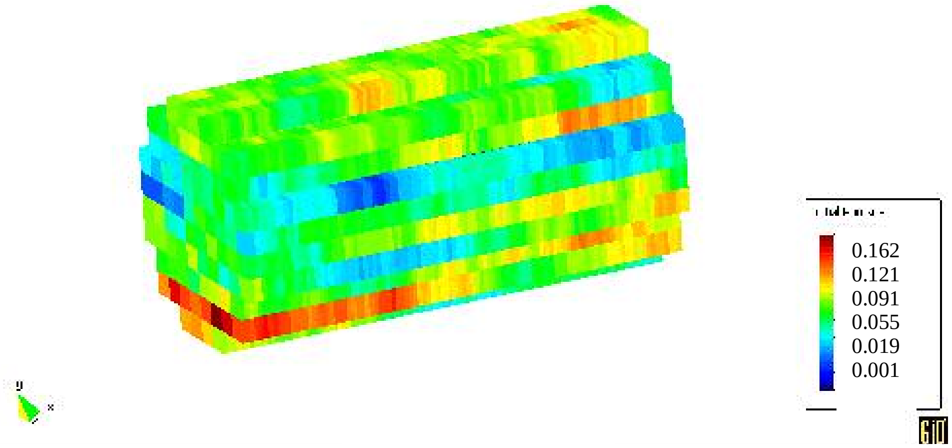

Figure 5.28: Initial porosity distribution in a core. (Case 9: λ_x/L=1, λ_y/L=0.025, λ_z/L=0.5).

Figure 5.29 shows the permeability responses during the acid flooding for the five cases with different correlation scale parameters. Because the correlation scale parameters for all of four correlated cases are higher than or equal to the core length, the permeability increases in these four cases are quite similar. However, compared to the uncorrelated case, permeability increase much faster in the four correlated cases at the earlier stage of acid injection. So, with smaller volume of acid injection, the stimulation efficiency in correlated porosity fields is much higher than in uncorrelated ones.

Figure 5.30 shows that the larger the correlation scale parameter in the axial direction, the smaller the PVbt is. For the highly layered core (high correlation scale parameter), Case 6, the pore volumes to breakthrough was 2, compared with 34 for the homogeneous case. This means that acid can propagate much farther in a striated sandstone with small high-permeability streaks than is predicted by a standard model of sandstone acidizing.

Figures 5.31 - 5.34 demonstrate the net porosity change above 0.02 for the layered porosity/permeability field (Case 6) at different stages of injection. Compared with the original porosity distribution (Figure 5.27), we see that the high permeability layer in the lower part of the core is preferentially attacked by the acid, allowing the acid to rapidly progress through the core. By the time that 35 PV of acid were injected, the porosity increase in the high permeability streak is as high at the exit side of the core as at the face of the core in the homogeneous case. This is because of the large throughput of acid in the high permeability streak. Several other high permeability streaks have also been stimulated significantly in this correlated porosity field.

The permeability profile after 5 PV of acid injection in Case 6 (Figure 5.35) also shows that porosity correlation in axial direction increases the rate of acid propagation. After 5 PV of acid injection, high permeability path way is established through the high porosity streak. In this case the acid pore volumes to breakthrough was about 2.

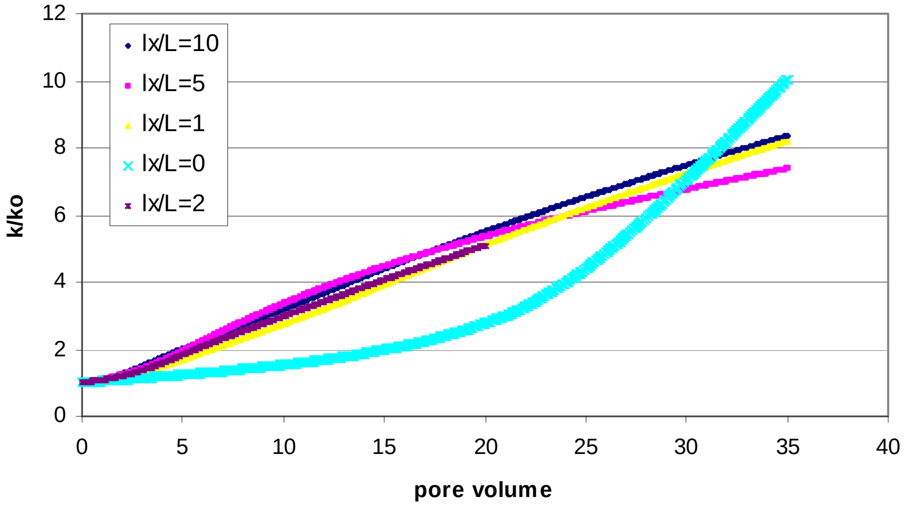

Figure 5.29: Permeability evolution for correlated porosity cases and completely random porosity case.

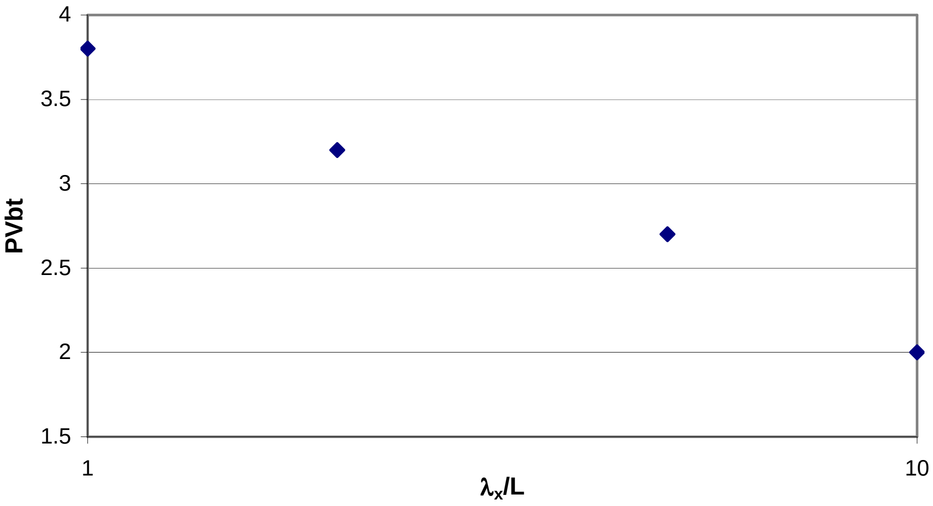

Figure 5.30: Acid breakthrough volume for correlated porosity cases.

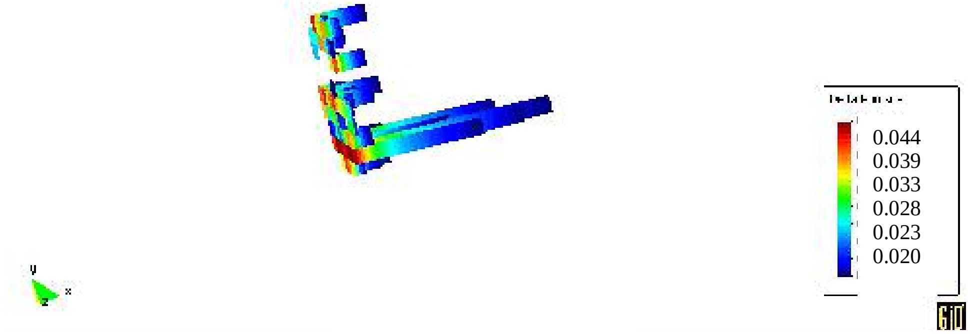

Figure 5.31: $\Delta\phi$ for correlated porosity case after 5 PV of acid injection in Case 6 ($\Delta\phi>0.02$) ($\lambda_x/L=10$, $\lambda_y/L=0.025$, $\lambda_z/L=0.5$).

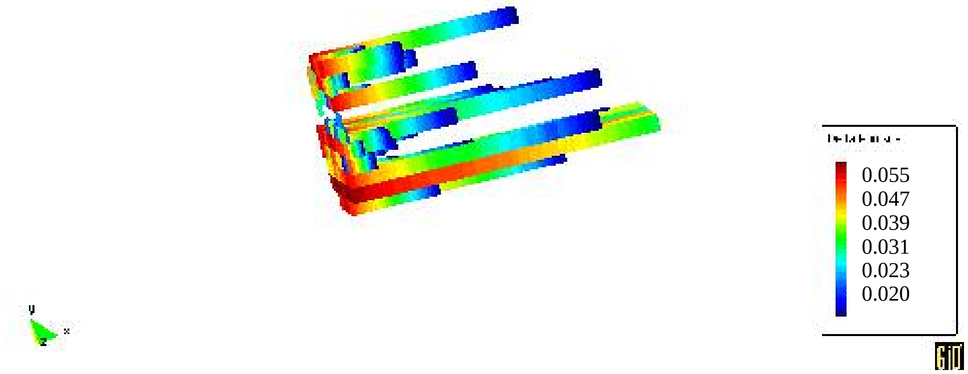

Figure 5.32: $\Delta\phi$ for correlated porosity case after 15 PV of acid injection in Case 6 ($\Delta\phi>0.02$) ($\lambda_x/L=10$, $\lambda_y/L=0.025$, $\lambda_z/L=0.5$).

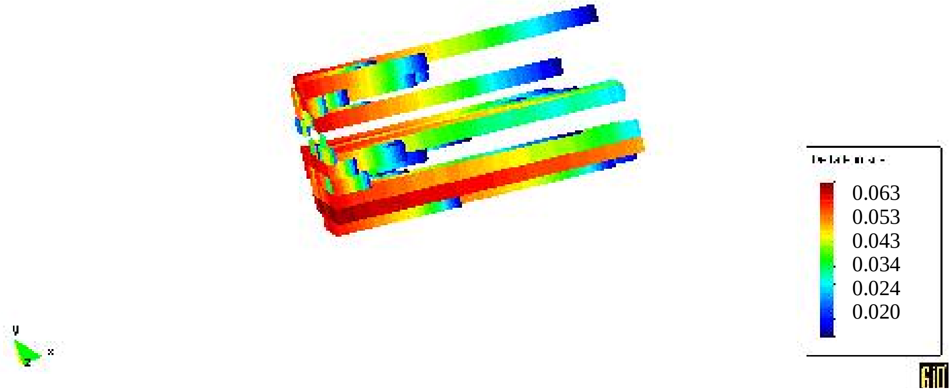

Figure 5.33: $\Delta\phi$ for correlated porosity case after 25 PV of acid injection in Case 6 ($\Delta\phi$>0.02) (λ_x/L=10, λ_y/L=0.025, λ_z/L=0.5).

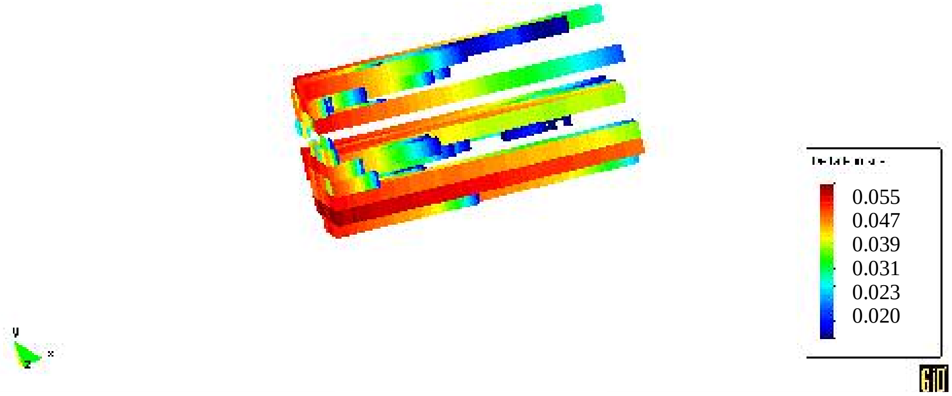

Figure 5.34: $\Delta\phi$ for correlated porosity case after 35 PV of acid injection in Case 6 ($\Delta\phi$>0.02) (λ_x/L=10, λ_y/L=0.025, λ_z/L=0.5).

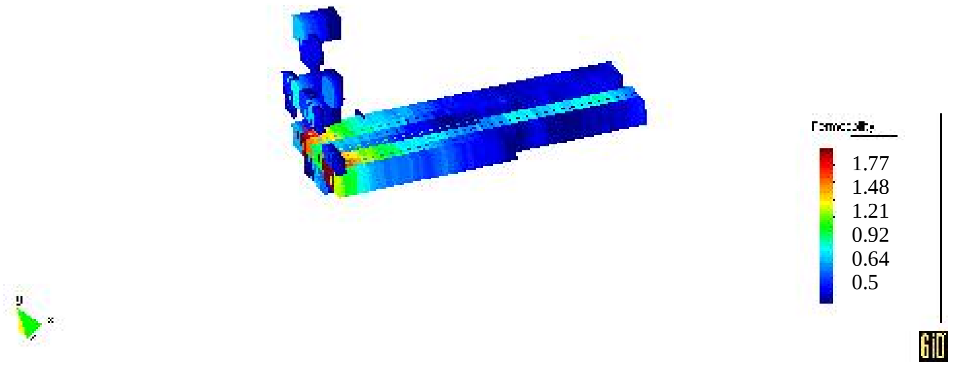

Figure 5.35: Permeability (Darcy) distribution after 5 PV of acid injection (λ_x/L=10, λ_y/L=0.025, λ_z/L=0.5).

5.1.4 HETEROGENEOUS MINERAL AND HOMOGENEOUS POROSITY

To have a better understanding of how the fast mineral distribution affects acidizing, based on the given average volume fraction of fast reacting mineral, 0.04, a heterogeneous distribution of fast reacting mineral with uniform probability between the given minimum and maximum content was generated by the simulator (Figure 5.36) (Case 10). The porosity is assumed to be homogeneous, with a value of 0.08. We simulated at an injection rate of 5ml/min and a temperature of 95°C.

Figures 5.37 and 5.38 demonstrate the dimensionless HF concentration distribution after 5 PV and 25 PV of acid injection, respectively. Compared with the simulation results of the heterogeneous porosity cases, the HF concentration distribution in this case is more uniform. Though there are still some flow paths in the core that show higher dimensionless velocity than other area (Figure 5.39), the absolute velocity range is from 1.5 to 3 for this case. Compared to the heterogeneous porosity case with dimensionless velocity range of 4 - 17, the velocity distribution is quite uniform with heterogeneous minerals and homogeneous porosity. When porosity is heterogeneous and fast reacting mineral is homogeneous, bigger pores take more acid and therefore more minerals can be dissolved, which can result in flowing channels in the core. However, when porosity is homogeneous and fast reacting mineral is heterogeneous, each pore takes the same amount of acid, but in the pores with less fast reacting mineral, less acid is consumed and the rest will propagate

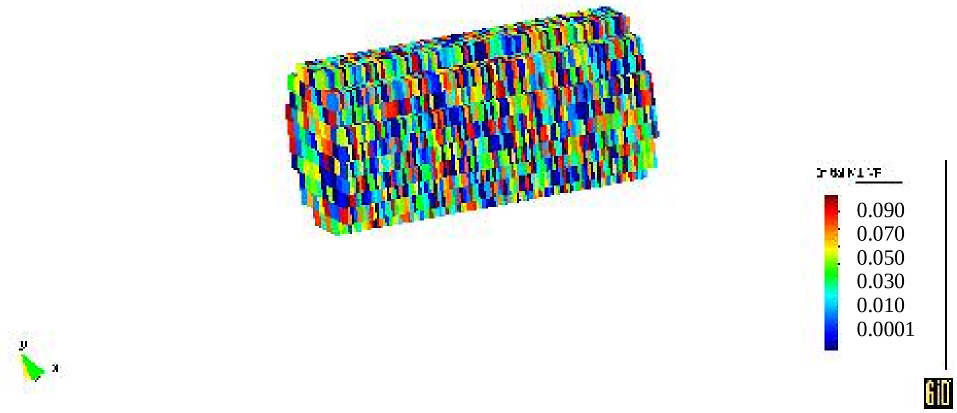

Figure 5.36: Initial distribution of fast reacting mineral (volume fraction).

(Average: 0.04)

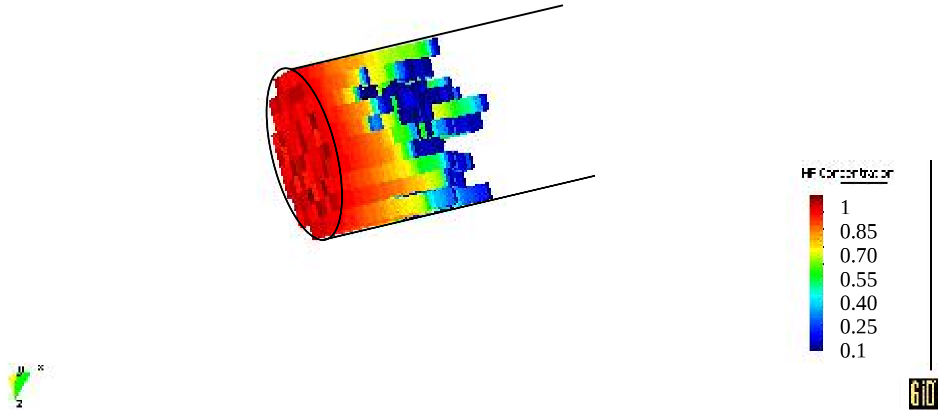

Figure 5.37: HF concentration (>0.1) distribution after 5 PV of acid injection.

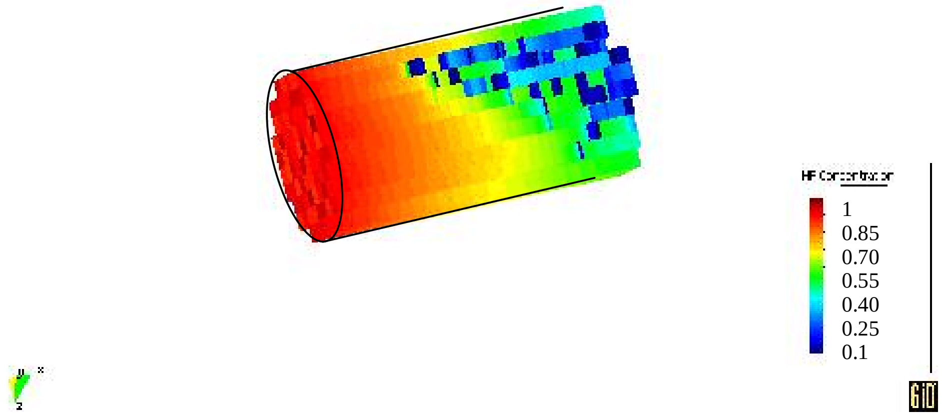

Figure 5.38: HF concentration (>0.1) after 25 PV of acid injection.

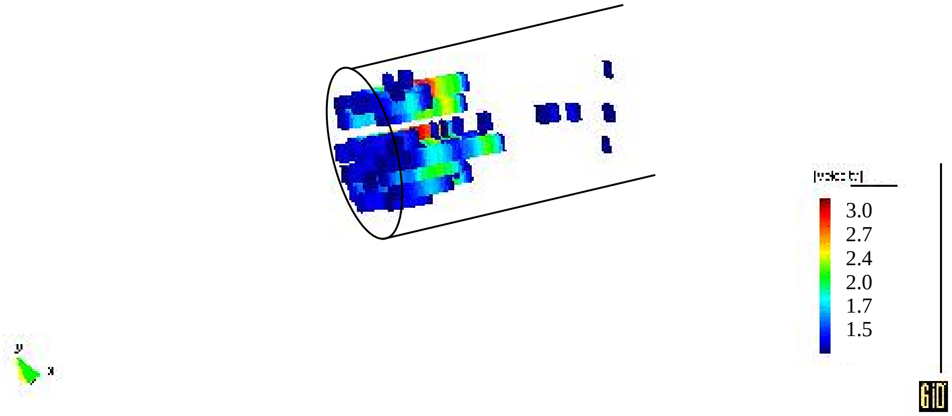

Figure 5.39: Dimensionless velocity distribution (>1.5) after 5 PV of acid injection.

further. In pores with more fast reacting mineral, not only is there HF consumed more rapidly, but also the by-product, H_2SiF_6, reacts with the fast reacting mineral and precipitates silica gel, which decreases the permeability of the pore. Generally the heterogeneous minerals have less effect on acid flow pattern during acidizing.

5.1.5 CORRELATED MINERAL DISTRIBUTION AND HOMOGENEOUS POROSITY DISTRIBUTION

It has been addressed in the previous part that porosity correlation in the main acid flowing direction is helpful for generating flowing channels in sandstone cores. In the next section, a simulation case, Case 11, is designed to test whether streaks in minerals, for example, thin clay layers, would affect the acid propagation. We maintained a constant porosity field to isolate the effect of minerals.

Keeping the other parameters the same as the previous case, the simulator generated a correlated mineral initial distribution instead of a completely random distribution. The generated correlated mineral distribution is demonstrated in Figure 5.40.

Figures 5.41 and 5.42 represent the permeability profiles after 5 PV and 35 PV of acid injection, respectively. In the layers with lower initial fast reacting mineral content, HF propagates further than in layers containing more fast reacting mineral. However, permeability is higher in layer with more fast reacting minerals than in others at the inlet of the core. This is because that more space can be created in layers with larger content of fast-reacting minerals and increase more permeability if enough acid is provided. Also because that more acid is consumed in layers with more fast-reacting minerals to dissolve more minerals at the inlet, acid penetrates shorter in these layers than those with less fast-reacting minerals.

Another possible reason is that precipitate produced in secondary and tertiary reaction blocked the regions with more fast-reacting mineral and not very much acid can flow into those regions. In layers with lower content of fast-reacting mineral, more HF can be consumed to dissolve the precipitate produced there and create higher permeability. As a result, the layers with low content of fast reacting mineral will accept more and more acid during the treatment. Figures 5.43 and 5.44 show the distribution of precipitate after 5 and 35 PV acid injection. The precipitation front

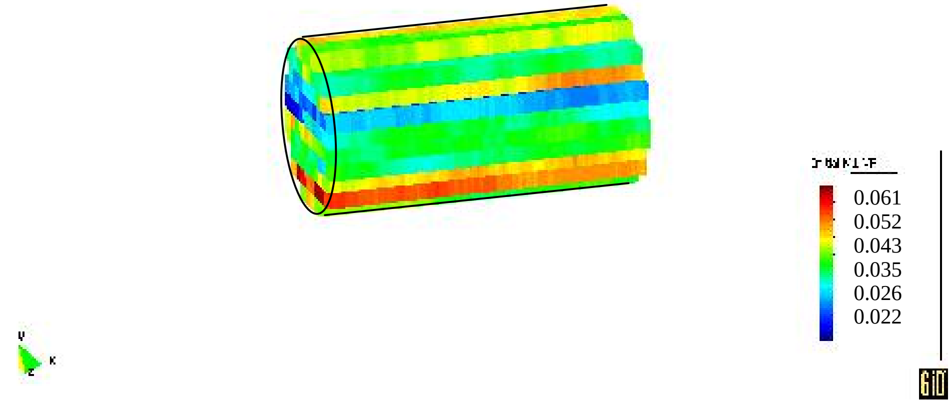

Figure 5.40: Initial fast reacting mineral distribution (λ_x/L=10, λ_y/L=0.025, λ_z/L=0.5).

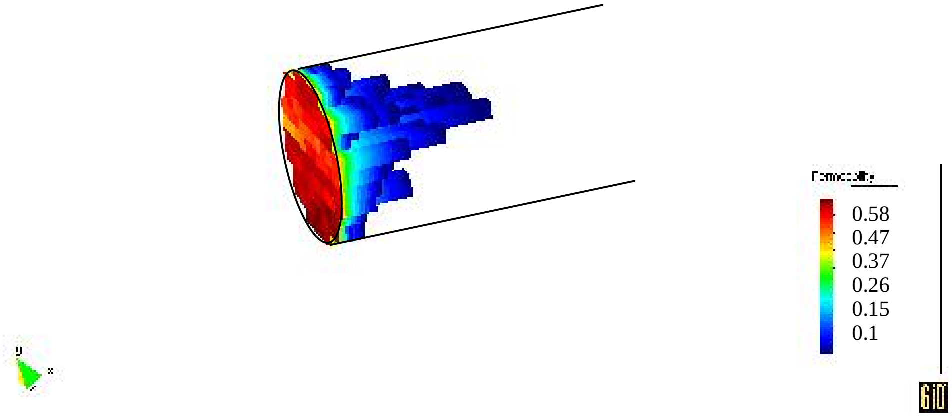

Figure 5.41: Permeability (Darcy) distribution after 5 PV of acid injection (λ_x/L=10, λ_y/L=0.025, λ_z/L=0.5).

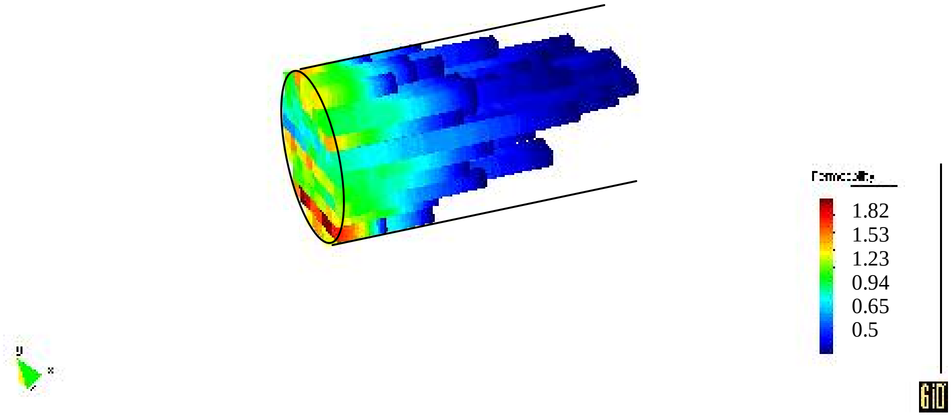

Figure 5.42: Permeability (Darcy) distribution after 35 PV of acid injection (λ_x/L=10, λ_y/L=0.025, λ_z/L=0.5).

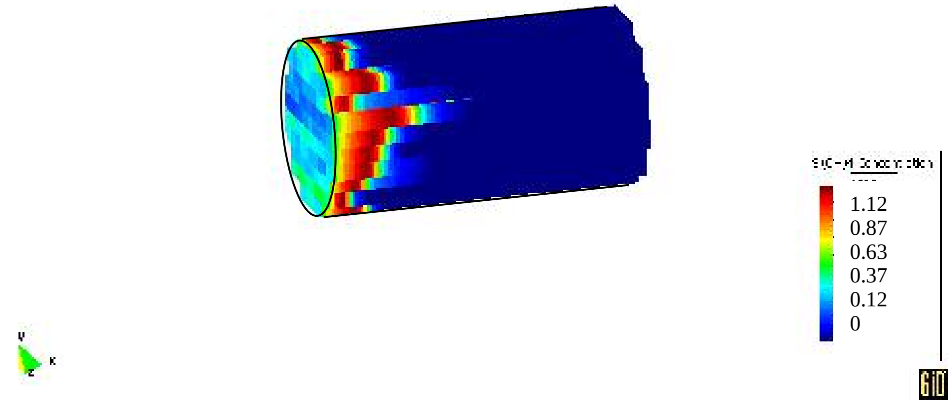

Figure 5.43: Precipitate distribution after 5 PV of acid injection.

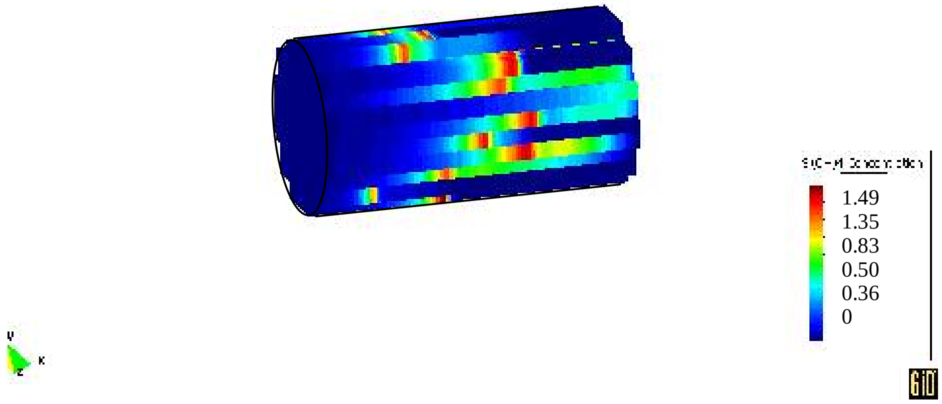

Figure 5.44: Precipitate distribution after 35 PV of acid injection.

extends much.further in lower fast-reacting mineral zones than in higher fast-reacting mineral ones. For example, the precipitate in the highest fast-reacting mineral layer (compare with Figure 5.40) moved very little after 5 PV of acid injection

Though acid flow in this case is not uniform and some flow paths are created after some time, it is not so efficient as the correlated porosity cases. In this case, HF breaks through at 9.1 PV compared with break through at 2 PV in the correlated porosity case. Figure 5.45 compares the pressure responses during acidizing for the correlated porosity case and the correlated minerals case. Apparently, the pressure drops more rapidly in the correlated porosity case than in correlated minerals case.

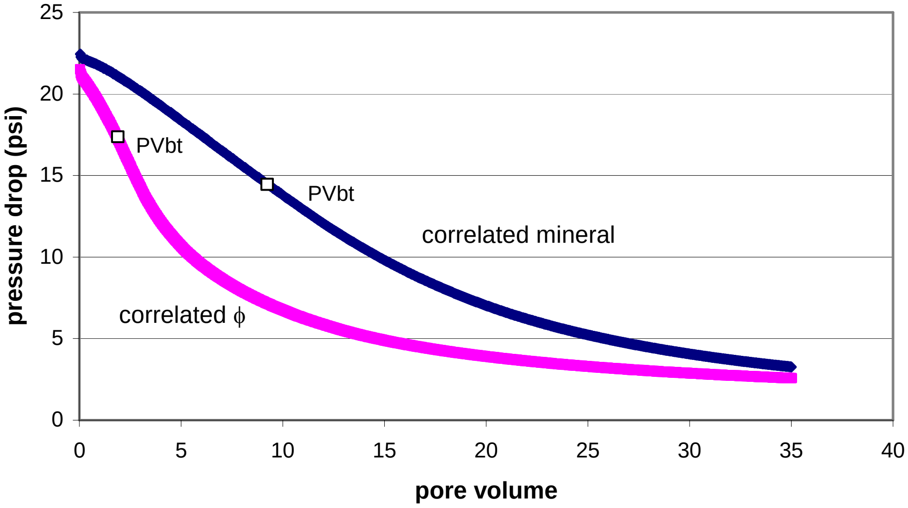

Figure 5.45: Pressure response to acidizing for the correlated porosity case and the correlated minerals case.

5.1.6 HETEROGENEOUS POROSITY AND MINERALS

To find the major factors that influence acid flowing pattern in cores, the heterogeneity of porosity and minerals are simulated separately in the previous sections. In the real world, however, both the porosity and minerals are heterogeneous. In this section, a case with both heterogeneous porosity and heterogeneous minerals, Case 12, is simulated. All other parameters are kept the same as Case 1 except a randomly distributed initial porosity and randomly distributed mineral profiles are generated at the beginning of the simulation.

The dimensionless HF concentration and velocity distributions at different stages during acid flooding are selected to illustrate the acid propagation in the core. Figures 5.46 - 5.49 show the dimensionless HF concentration distribution at 5, 15, 25, and 35 PV of acid injections. For all four plots, the maximum dimensionless HF

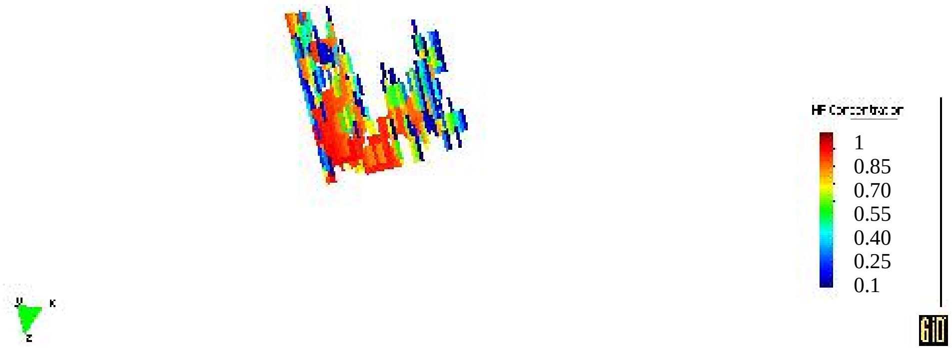

Figure 5.46: Dimensionless HF concentration distribution (5PV).

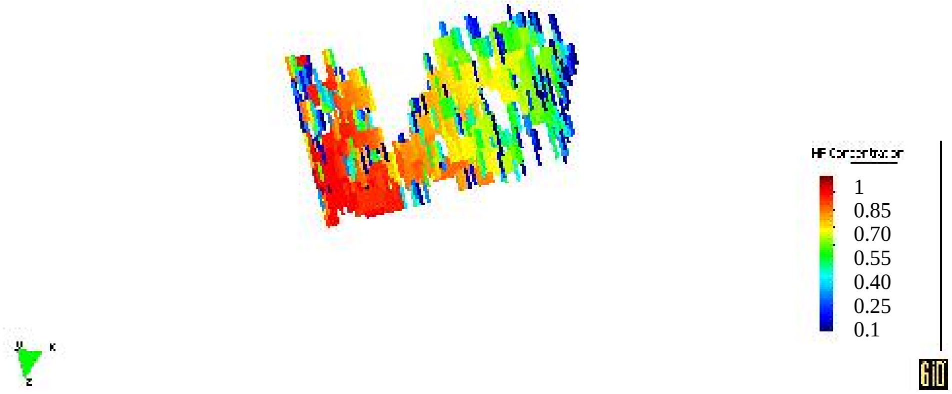

Figure 5.47: Dimensionless HF concentration distribution (15PV).

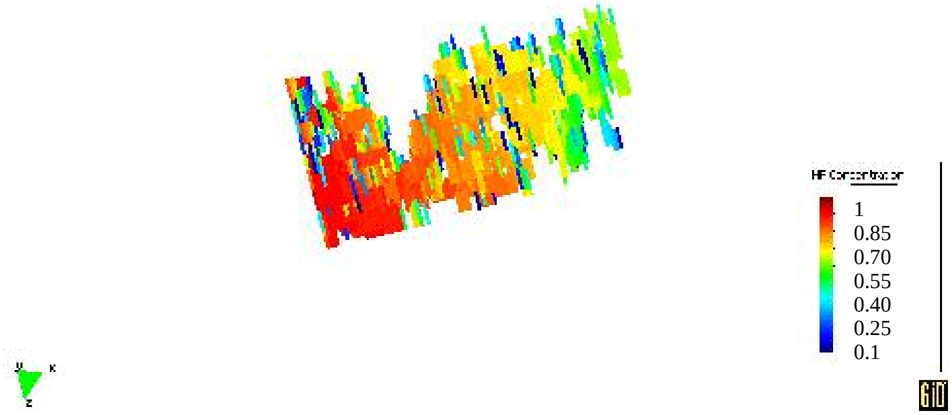

Figure 5.48: Dimensionless HF concentration distribution (25PV).

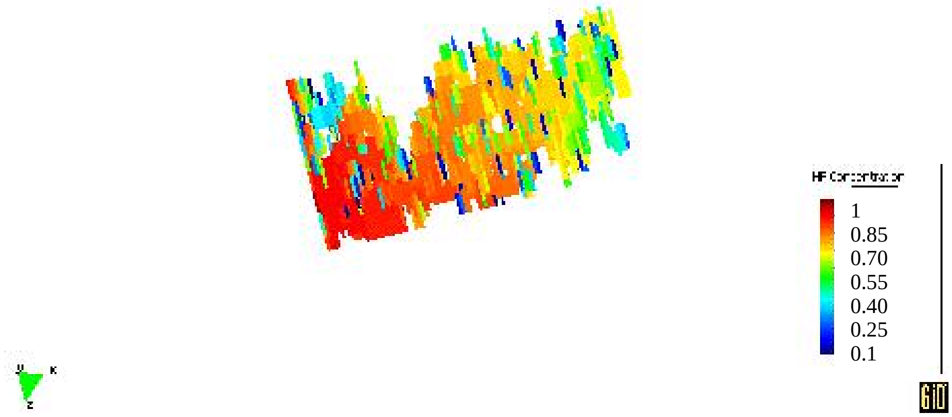

Figure 5.49: Dimensionless HF concentration distribution (35PV).

concentration is set as 1.1 and the minimum is set to 0.1. All grid blocks with HF concentration lower than 0.1 are cut off automatically. The acid flow paths are apparent.

In addition to the HF concentration, the development of acid flow channels during core flooding simulation can be visualized more clearly by the velocity distribution at different times. Figures 5.50 - 5.53 show the velocity distributions at the four stages during the simulation, 5 PV, 15 PV, 25 PV, and 35 PV. In these four plots, the minimum dimensionless velocity is set to 1 and there is no maximum limit. So only those grid blocks in which dimensionless velocity is higher than 1 is shown in the graph. The results suggest that in heterogeneous core, it is possible to create flow channels instead of uniform acid propagation in the core.

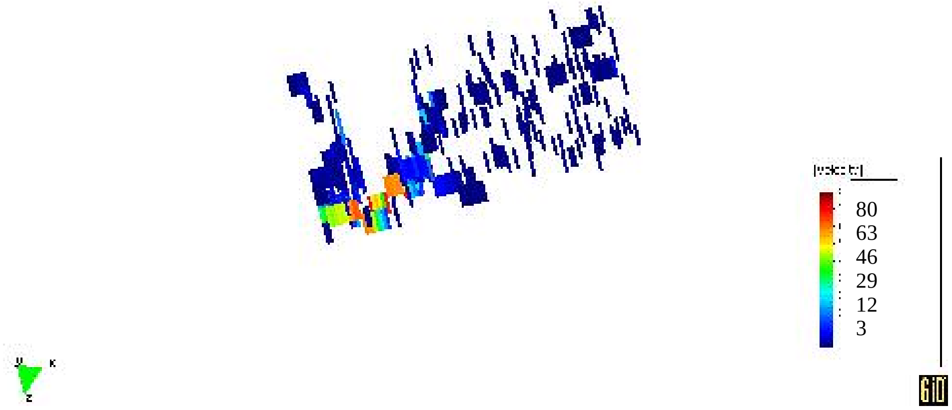

Figure 5.50: Dimensionless velocity distribution (5PV).

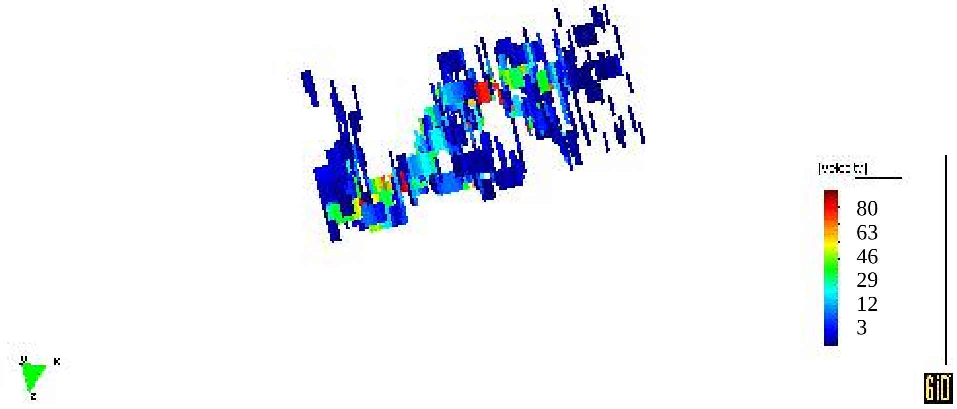

Figure 5.51: Dimensionless velocity distribution (15PV).

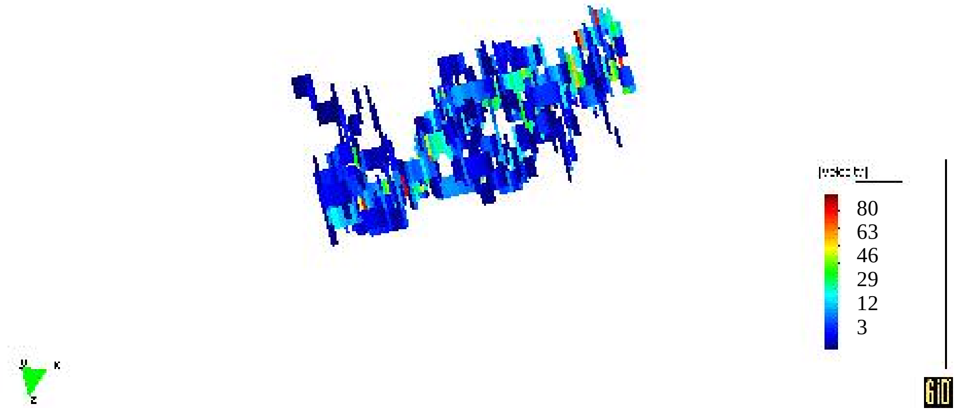

Figure 5.52: Dimensionless velocity distribution (25PV).

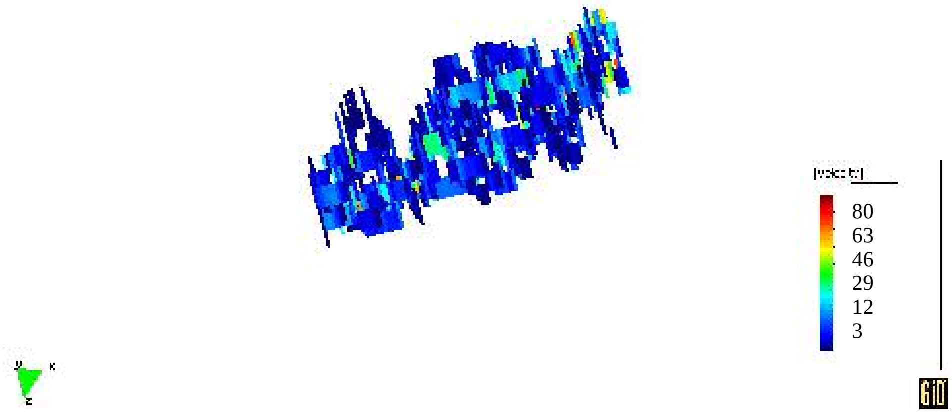

Figure 5.53: Dimensionless velocity distribution (35PV).

5.2 Effect of Fast Reacting Mineral Content on Matrix Flow Pattern

To test the effect of fast reacting mineral content, a core with the average volume fraction of 0.2 of fast reacting mineral was studied in Case 13. The initial fast reacting mineral is completely randomly distributed.

The porosity change during the acid flooding is demonstrated in Figures 5.54 - 5.57. Since homogeneous porosity is assumed in this case, the porosity distributions also show where the acid flows through and where it is consumed to remove the fast reacting mineral. Figure 5.54 shows that after 5 PV of acid injection, HF propagated only a short distance from the inlet. This is because the high content of fast reacting mineral present in the core consumed most of the HF injected. It apparently shows face dissolution at the inlet. However, it has illustrated the tendency of channeling after only 15 PV. The HF front has passed half of the core by this time. Some part of the core behind the HF front has porosity increase less than 0.01. This tendency is more clearly demonstrated at 25 PV and 35 PV of acid injection. It indicates that HF flows through the created paths and bypasses the other area of the core after 5 PV of acid injection. The permeability profiles in Figures 5.58 - 5.61 also support this conclusion. These four plots represent the permeability higher than 10 Darcy at different simulation stages. They suggest high permeability region is created in the center part of the core.

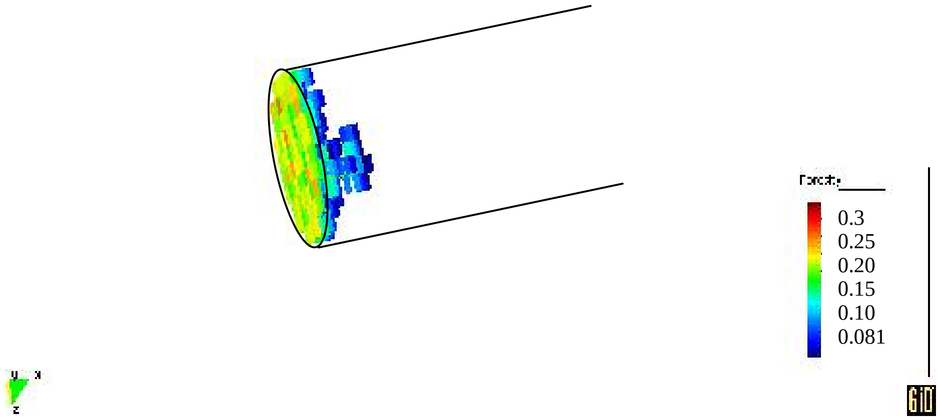

Figure 5.54: Porosity (ϕ>0.08) distribution (5 PV).

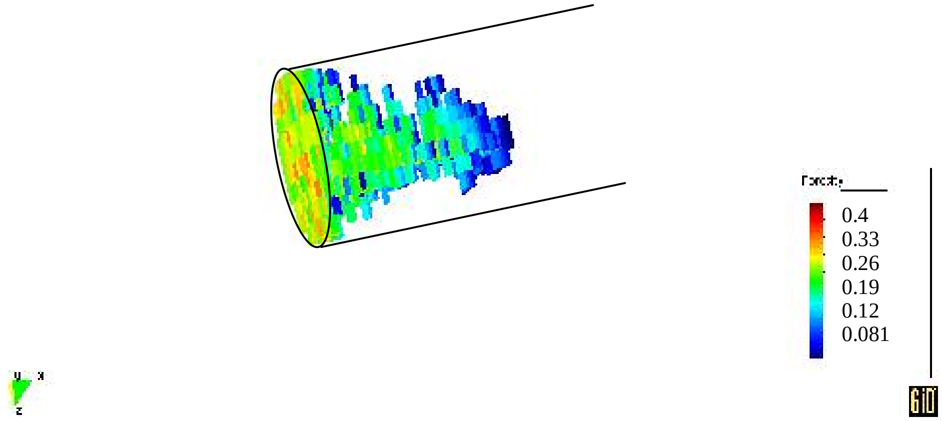

Figure 5.55: Porosity (ϕ>0.08) distribution (15 PV).

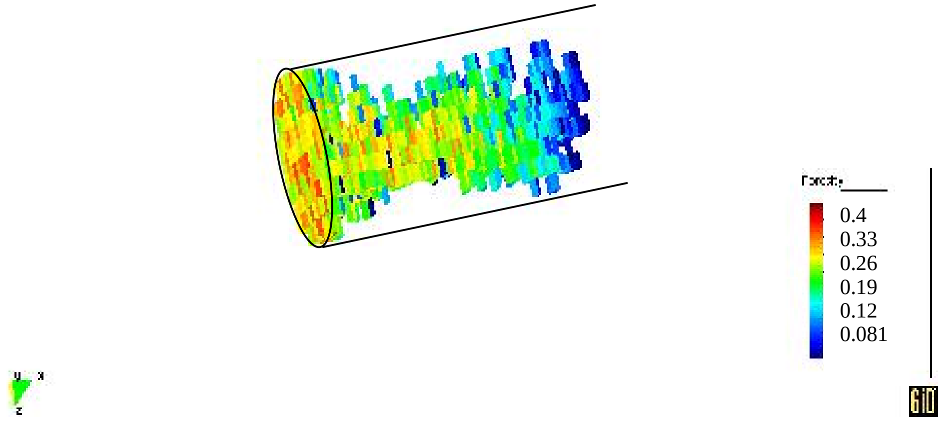

Figure 5.56: Porosity (ϕ>0.08) distribution (25 PV).

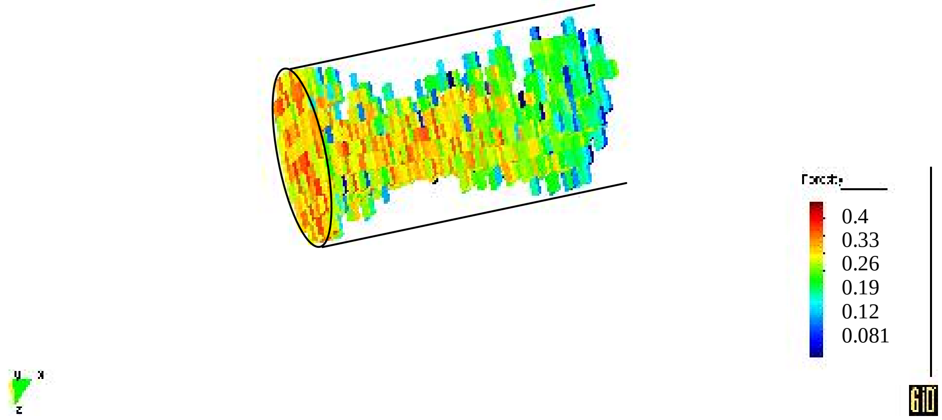

Figure 5.57: Porosity (ϕ>0.08) distribution (35 PV).

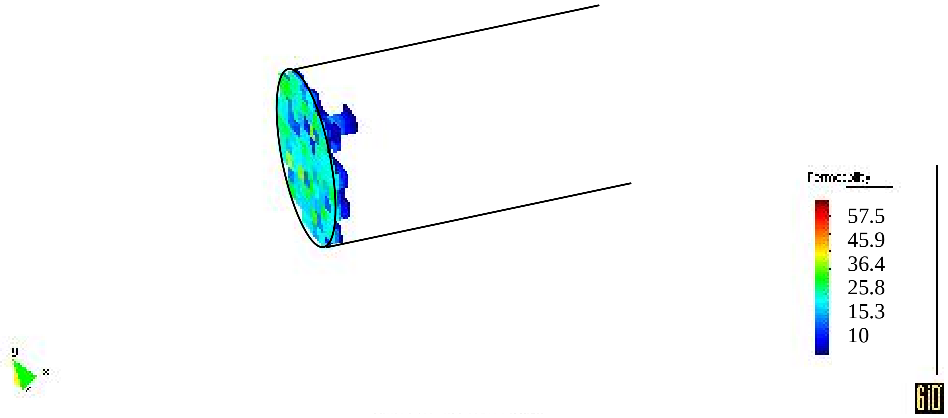

Figure 5.58: Permeability distribution (5 PV).

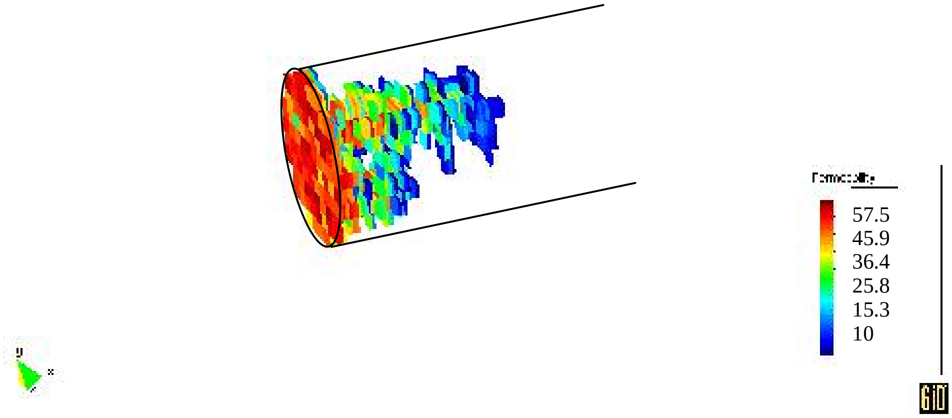

Figure 5.59: Permeability distribution (15 PV).

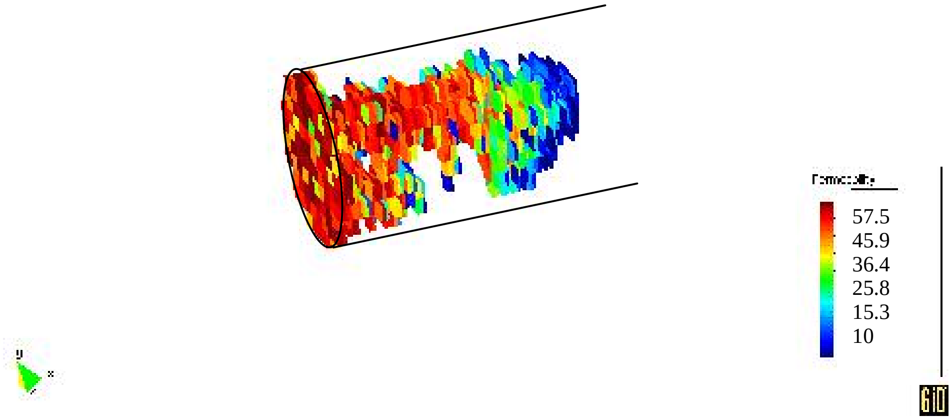

Figure 5.60: Permeability distribution (25 PV).

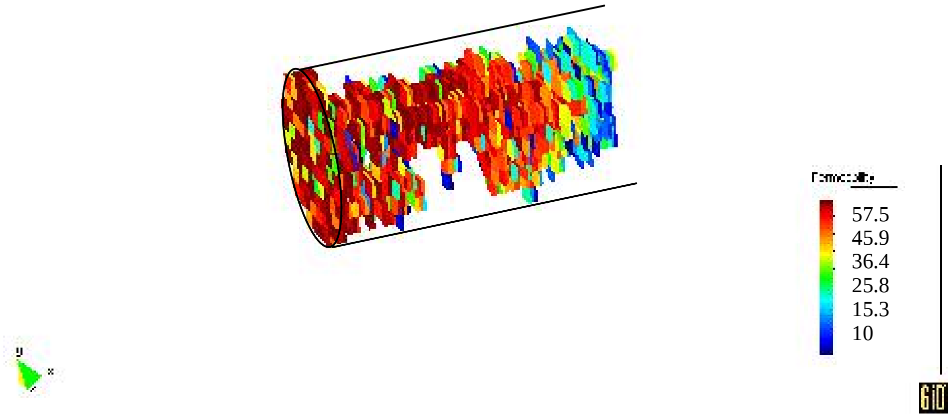

Figure 5.61: Permeability distribution (35 PV).

5.3 Effect of Acid Concentration on Matrix Flow Pattern

Application of larger HF concentration has been found to have better stimulation results in some applications by achieving much deeper acid penetration depth [Kalfayan and Metcalf, 2000]. Another simulation case, Case 14, was designed to test the effect of acid concentration on sandstone acidizing. In this case, we kept other parameters the same as listed in Table 5.1, using a porosity standard deviation of 0.03 and homogeneous minerals, but with an increase of both HF and HCl concentrations to 12% by weight. The pressure drop response to the pore volume of acid injected is compared in Figure 5.62 with Case 3, in which 6% by weight of HF and HCl were used. It is clear that the pressure drop decreases much more rapidly in the case with larger concentration of HF and HCl and acid breaks through 10 PV earlier than when 6wt%/6wt% HF/HCl acid is used.

Figure 5.63 compares the HF front penetration after 5 PV of acid injection in Case 3 and Case 14. It shows that the acid concentration does not change the matrix flow pattern very much. In both cases, there is no clear preference of flow path even though the acid does not show uniform penetration. The deeper penetration of the HF front in the higher acid concentration case is mainly due to higher acid strength instead of flow channel generation.

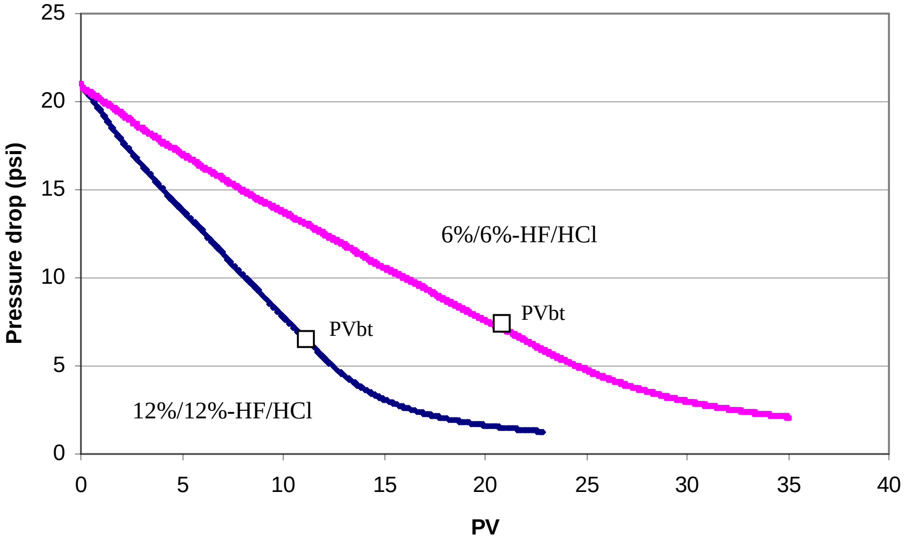

Figure 5.62: Pressure drop response during core acid flooding.

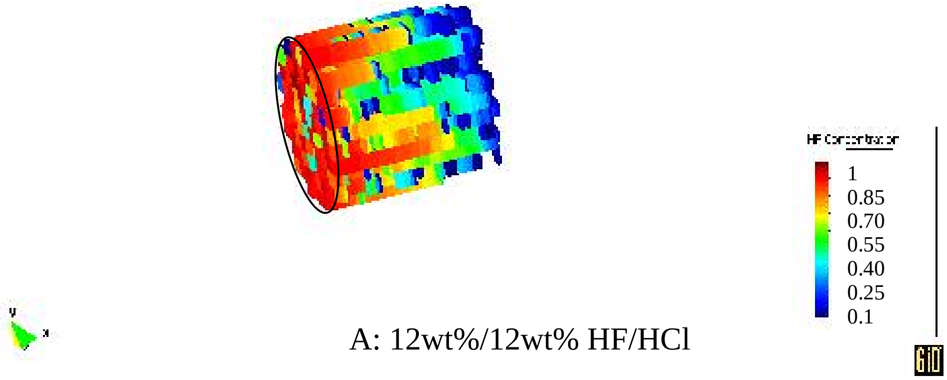

A: 12wt%/12wt% HF/HCl

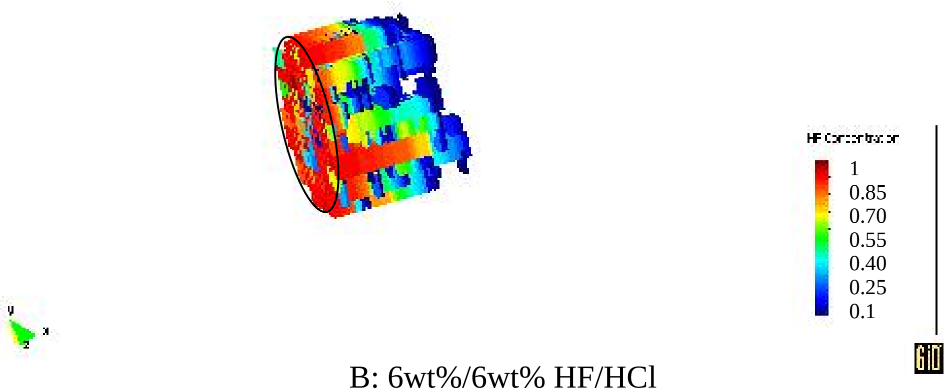

B: 6wt%/6wt% HF/HCl

Figure 5.63: HF distribution after 5 PV of acid injection.

CHAPTER 6 SUMMARY AND CONCLUSIONS

A fully three-dimensional simulator of sandstone acidizing has been developed to study the effect of fine-scale heterogeneity in the matrix. Using standard geostatistical methods, heterogeneous distributions of porosity, permeability, and mineral composition were generated as the initial condition of the rock. The matrix properties can be randomly distributed or can be correlated in any principle direction. The model has been used to simulate sandstone acid core flooding conditions. A one-inch diameter by two-inch long core was represented by 8000 grid blocks, each having potentially different initial properties. With grain diameter being 0.1 mm, there are more than 6000 sand grains in each grid block. So it meets continuity requirement to establish mass conservation equations.

The results from this model show that the presence of small-scale heterogeneities in sandstone has a dramatic impact on acidizing. Flow field heterogeneities cause acid to penetrate much further into the formation than would occur if the rock were homogeneous, as is assumed by standard models. The higher the standard deviation of the distribution, the deeper the acid penetrates.

When the porosity field is highly correlated in the axial direction, which represents a laminated structure, acid penetrates very rapidly into the matrix along the high permeability streaks. For this type of sandstone, the predicted time for acid to breakthrough in a core flood was as much as 17 times shorter than that predicted by a homogeneous model. In some cases, enough mineral is removed along the high permeability pathways that rock competence could not be retained, and distinct channels would likely form.

Compared to porosity heterogeneity, mineral heterogeneity has less impact on acid flow patterns. Although it also shows heterogeneous acid penetration, the HF concentration distribution behind the HF front is more uniform than what occurred in heterogeneous porosity cases. With same correlation strengths, the predicted acid breakthrough time is 2 PV when the porosity field is highly correlated in the axial direction, while when the mineral is correlated and porosity is uniform, the acid pore volume at breakthrough is 9.

When a core has both heterogeneous porosity and heterogeneous minerals, which is true with real rocks, simulation results show that it is possible to create high permeability channels inside the core. Most acid flows through those channels and bypasses other areas of the core.

The high content of fast reacting mineral increases the potential to create channels along the core. The porosity change in the core illustrated the impact of fast reacting mineral content on acid flow patterns. When the average volume fraction of fast reacting mineral is increased from 0.04 to 0.2, instead of completely random penetration as occurred in the lower content case, following face dissolution at the inlet, acid starts to concentrate in some areas of the core and generates high permeability pathways along the core.

Results show that the injected acid concentration has little effect on acid flow patterns. When higher concentration HF/HCl is used, the faster acid penetration is caused by the higher reaction strength instead of channel generation.

Overall, this model has shown that acid penetration in sandstones is likely to be much greater than is predicted by traditional models because of the flow field heterogeneities that commonly exist in sandstones.

APPENDIX A THE INTERFACE PROGRAM

Based on the mathematical model discussed in Chapter 2, a numerical simulation model is developed in C++ to simulate acid flow in cores. Its interface, implementation, output files, and post process of output data will be presented in this chapter.

A.1 Interface

Figure A.1 shows the input panel of the graphic interface of this simulator. The input data required to run the program are all collected on this panel. A total of seven sub-panels are included in this panel, namely Core information, Kinetic parameters, Simulation parameters, Porosity distribution, Mineral distribution, Mass dissolving power, and Mineral information. When running this simulator, a set of default data is provided. However, users can change any input to simulate their particular cases.

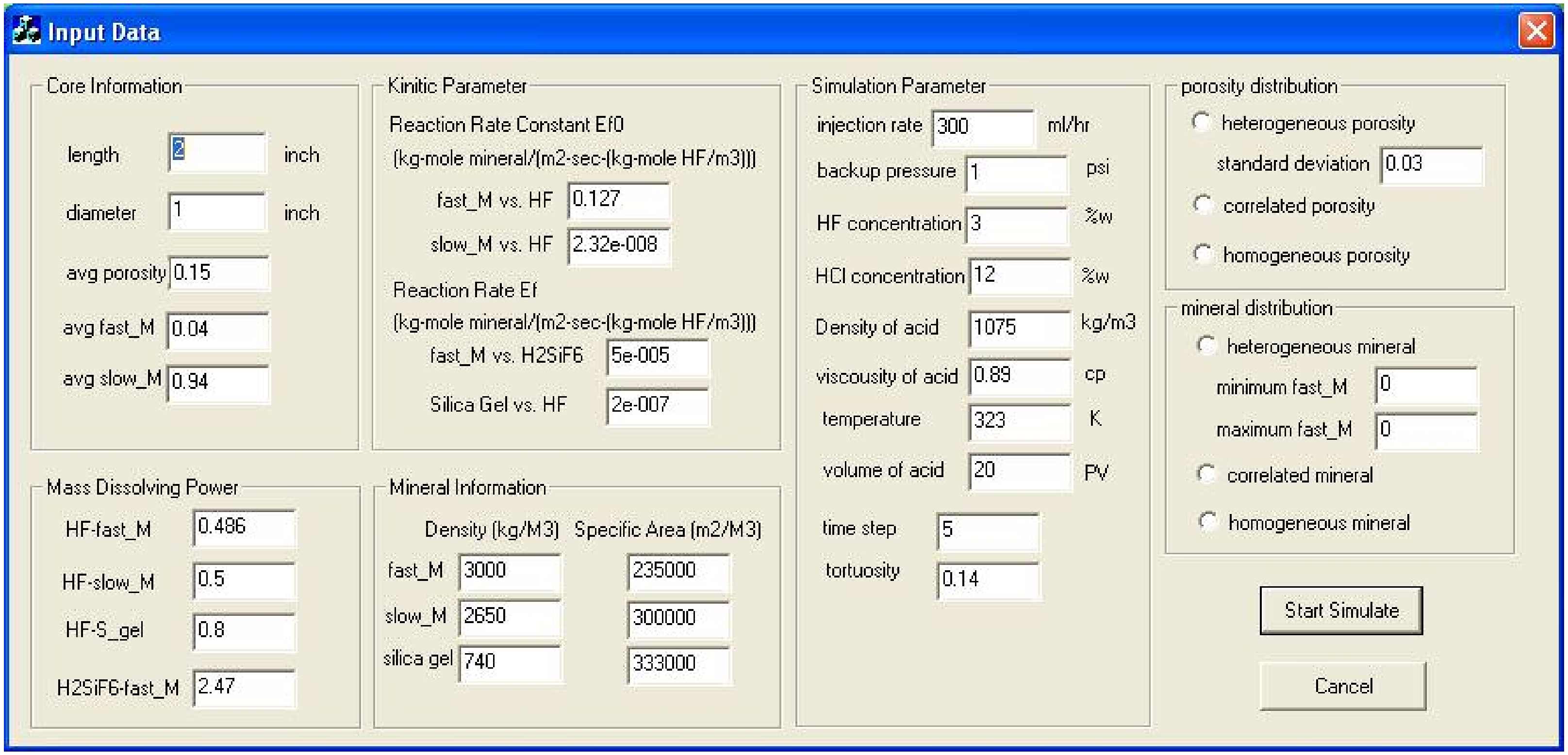

Core Information

length 2 inch
diameter 1 inch
avg porosity 0.15
avg fast_M 0.04
avg slow_M 0.94

Kinitic Parameter

Reaction Rate Constant Ef0
(kg-mole mineral/(m2-sec-(kg-mole HF/m3)))
fast_M vs. HF 0.127
slow_M vs. HF 2.32e-008
Reaction Rate Ef
(kg-mole mineral/(m2-sec-(kg-mole HF/m3)))
fast_M vs. H2SiF6 5e-005
Silica Gel vs. HF 2e-007

Simulation Parameter

injection rate 300 ml/hr
backup pressure 1 psi
HF concentration 3 %w
HCl concentration 12 %w
Density of acid 1075 kg/m3
viscousity of acid 0.89 cp
temperature 323 K
volume of acid 20 PV
time step 5
tortuosity 0.14

porosity distribution

○ heterogeneous porosity
standard deviation 0.03
○ correlated porosity
○ homogeneous porosity

mineral distribution

○ heterogeneous mineral
minimum fast_M 0
maximum fast_M 0
○ correlated mineral
○ homogeneous mineral

Mass Dissolving Power

HF-fast_M 0.486
HF-slow_M 0.5
HF-S_gel 0.8
H2SiF6-fast_M 2.47

Mineral Information

	Density (kg/M3)	Specific Area (m2/M3)
fast_M	3000	235000
slow_M	2650	300000
silica gel	740	333000

Figure A.1: The input panel of the simulator

A.1.1 CORE INFORMATION

In the sub-panel of Core Information, the information about the core is required, which include the length and diameter of the core, the average porosity, and the average volume fractions of fast-reacting mineral and slow-reacting mineral. The length and diameter of the core can be easily obtained from the core dimension. It is not hard either to determine the average porosity (the mean of porosity) and average mineral content (the mean of mineral volume fraction). There are three groups of minerals in the model, fast-reacting mineral, slow-reacting mineral, and carbonates. Since the sum of the total volume fraction cannot be greater than 1, only two of the there minerals are required in the input panel. The fast reacting mineral and slow reacting mineral are input by users. The volume fraction of carbonate is calculated in the program by subtracting the input averages of fast and slow reacting mineral from 1.

A.1.2 KINETIC PARAMETERS

In this work, four main reactions are considered. Accordingly, four reaction rates are required in the simulation. The first two reactions are better understood and their rate constants usually can be found in literatures and their relationship as a function of temperature has been established [Economides et al., 1994]. The default reaction rate constants (E_{f0}) of the reaction between fast-reacting mineral and HF, fast_M vs. HF, and for the reaction between slow-reacting mineral and HF, slow_M vs. HF are given as shown in Figure A.1. However, for the last two reactions, not very much work has been done. Even though some authors put effort on secondary and tertiary reaction rate investigation and concluded some rate laws corresponding to temperature change [Gdanski, 1996, 1997], no satisfied exact correlations between those reaction rates and temperature have been found. The user may determine them in particular conditions by some experimental results. Therefore the reaction rates for the last two reactions, fast_M vs. H2SiF6 being the reaction rate constant between fast-reacting mineral and H_2SiF_6 and Silica Gel vs. HF being the reaction constant between the precipitate and HF, are required to input by the user instead of hard coded in the program. The default values were determined from da Motta's simulation [da Motta et al., 1993].

A.1.3 SIMULATION PARAMETERS

In the group of simulation parameters, the user is required to input the injection rate in ml/hr, the back pressure in atmosphere, HF concentration in percent by weight (%wt), HCl concentration in percent by weight, density of acid in kg/m^3, viscosity of acid in cp, temperature in Kelvin, the total pore volume of acid injected (volume of acid), up to which the simulation will stop, time interval between each time step (time step), and tortuosity. Only the last three need to be clarified here. Time step here is an important parameter because it affects the stability of the simulation. It is actually the time interval between two time steps. If it is too high, the program will get unstable and does not converge. The stability also depends on the injection rate. When injection rate is higher than 600ml/hr, the time step should be lower, and vice versa. It was found that the default value, 5 second, is suitable for most injection rate ranged from 2~20 ml/min. Another parameter the user needs to pay attention to is the turtuosity. It is actually a parameter used in the permeability calculation model, which will be introduced later in this chapter. For this simulator, the porosity is initialized and then permeability is calculated. Among the numerous factors accounted in the model, turtuosity may be the most uncertain one. So when we generate the initial porosity distribution, the turtuosity is adjusted to get particular overall permeability of the given core. The default value, 0.14, is the tortuosity used in our calculation. For other cases, it should be adjusted to get the correct original permeability for a particular porosity field.

A.1.4 POROSITY DISTRIBUTION

As stated in Chapter 3, this simulator can be used to generate homogeneous initial porosity, heterogeneous initial porosity, and correlated initial porosity. If the heterogeneous option is selected to run the simulator, the standard deviation is required and the porosity distribution is generated by the average porosity (mean) and the standard deviation. If the correlated porosity option is chosen, a text file named pore.txt containing the initial porosity for each grid block should exist in the same folder as the program. The construction of this file has been discussed in chapter 3. When homogeneous porosity is selected, nothing is required except the average porosity in the first input sub-panel.

A.1.5 MINERAL DISTRIBUTION

For the correlated mineral and homogeneous mineral options, the requirements are the same as the porosity distribution. However, when the heterogeneous option is selected, two parameters other than standard deviation are required. Instead of normal distribution, it is assumed that mineral distribution follows the uniform distribution between a minimum value and a maximum value. So, if heterogeneous mineral is chosen, users need to input the minimum and the maximum values of the fast reacting mineral volume fraction. By assuming carbonate is homogeneously distributed, the volume fraction of slow reacting mineral for each grid block equals to one minus the volume fraction of generated fast reacting mineral and the constant carbonate volume fraction.

A.1.6 MASS DISSOLVING POWER

The mass dissolving powers for these four reactions are input here. Default values are available. But for given conditions, it is better to determine their values by tests. HF-fast_M represents the dissolving power of HF reacting with fast-reacting mineral (kg mole fast-reacting mineral/kg mole HF), HF-slow_M is the dissolving power of HF reacting with slow-reacting mineral (kg mole slow-reacting mineral/kg mole HF), HF-S_gel denotes the dissolving power of HF reacting with silica gel(kg mole silica gel/kg mole HF), and H2SiF6-fast_M is the dissolving power of H_2SiF_6 reacting with fast-reacting mineral (kg mole fast-reacting mineral/kg mole H_2SiF_6).

A.1.7 MINERAL INFORMATION

This sub-panel includes densities and specific areas for the three involved minerals.

A.1.8 COMMAND BUTTONS

In addition to those sub-panels, there are two buttons in the user interface. After input all necessary data, clicking on the “Start Simulation” button will start the simulation of the core acid flooding. If the “Cancel” button is clicked during the simulation, the simulator will stop.

A.2 Output

The simulator generates several text files for the simulation results. Text file named *result.txt* records the pressure at each time step and also the breakthrough time. Therefore, it can be used to illustrate the pressure response and average permeability response during the acid injection. The text file called *exit_conc.txt* records the HF concentration in effluent at each time step during the acid injection. At every five PV, a text file will be generated, which contains the coordinates for each grid block and their corresponding pressure, porosity, permeability, dimensionless velocity in three directions, dimensionless volume fractions of fast reacting mineral, slow reacting mineral, and silica gel, dimensionless HF concentration, and dimensionless H_2SiF_6 concentration. According to the sequence of the output, they are named as *result1.txt*, *result2.txt*, and so on. *result1.txt*, for example, stores all the information about the simulation after 5 PV of acid injection.

A.3 3D Visualization of Simulation Results

In addition to the Excel plots showing the pressure response and the dimensionless HF concentration in the effluent during simulation, 3D plots are created to demonstrate the distributions of permeability, porosity, pressure, HF concentration, H_2SiF_6 concentration, the fast reacting mineral, the slow reacting mineral, and the precipitate content in the core at different stages in the course of core acid flooding. After the simulation, the output results are post-processed by UT3DVIS, and 3D plots can be generated by GID software. Xie discussed the 3D visualization of the simulation results in detail [Xie, 2004].

APPENDIX B VALIDATION OF THE MODEL

To verify this model, we compared the simulation results of a core flooding, core 1122 (2-inch length, 1.5-inch diameter), with the experiment results [Thomas et al., 2002]. This core was highly laminated. Its petrophysical and operational parameters are given in Table B.1.

Table B.1: Parameters for coreflood test of core 1122

Temperature (^oC)	150
Injected acid concentration HCl/HF (wt %)	12/3
Preflush	10% Acetic acid
Injection rate (mL/min)	4
Permeability (md)	0.42
Mineral composition	98% Quartz, 0.8%Ilite, 0.3% Chlorite, 0.5% Siderite
Heterogeneity	Highly laminated in x-y direction
PV injected	10
Initial ΔP (psi)	260
Observation	Channels in high permeable layers; one dominant wormhole; mainly quartz remaining, but many sections remained unacidized.

The pressure response for this test is shown in Figure B.1. We can see from the figure that a rapid decrease in differential pressure from 260 psi to approximately 2 psi occurred after about 2 pore volume of acid injection and mud acid broke through at about 2 pore volume of acid injection. And post-treatment thin section examination suggested that channels were created in the core.

To simulate this coreflood test, we generated a porosity realization with very strong correlation in x direction to represent the highly laminated core. All of other parameters involved are the same as the test. The pressure response predicted by this

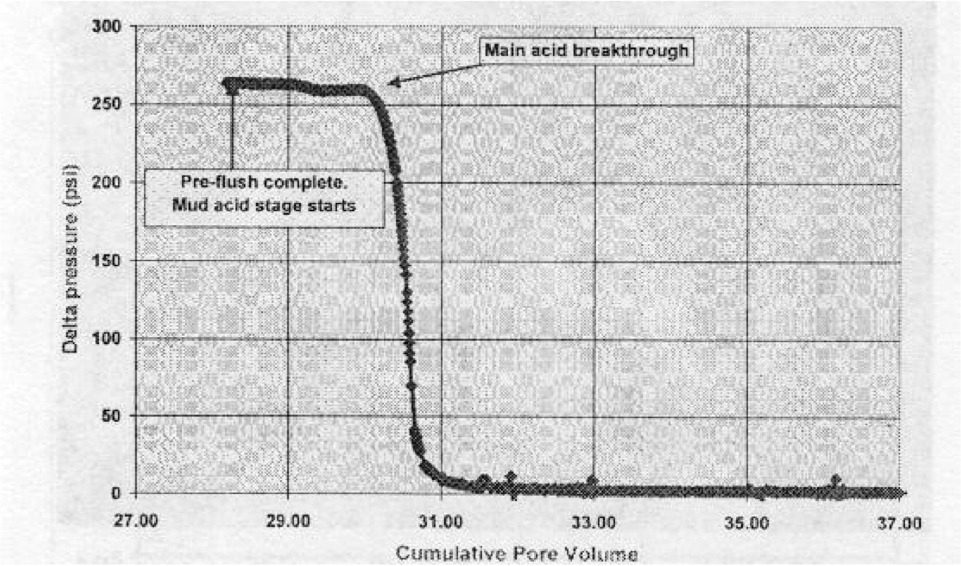

Figure B.1: Differential pressure plot of core 1122 during treatment with 12wt% HCl – 3 wt% HF [Thomas et al., 2002]

model is shown in Figure B.2. To compare with the test result, this height and width of this figure are adjusted. Even though the pressure in simulation showed more gradually decreasing than in the test, it reached almost the same value after acid breakthrough. Before acid breakthrough, pressure decreases very rapidly. And the predicted breakthrough pore volume by this model is 3.6 PV, which is close to the test results.

A 3D plot of permeability distribution after 3 PV of acid injection is demonstrated in Figure B.3. By cutting off all grid blocks with permeability lower than 350 md, Figure B.4 clearly show the high permeability channels established inside the core.

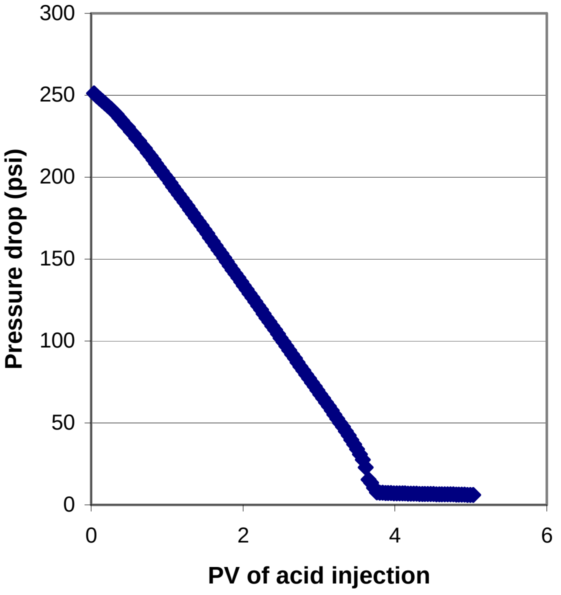

Figure B.2: Pressure response during simulation of core 1122 test.

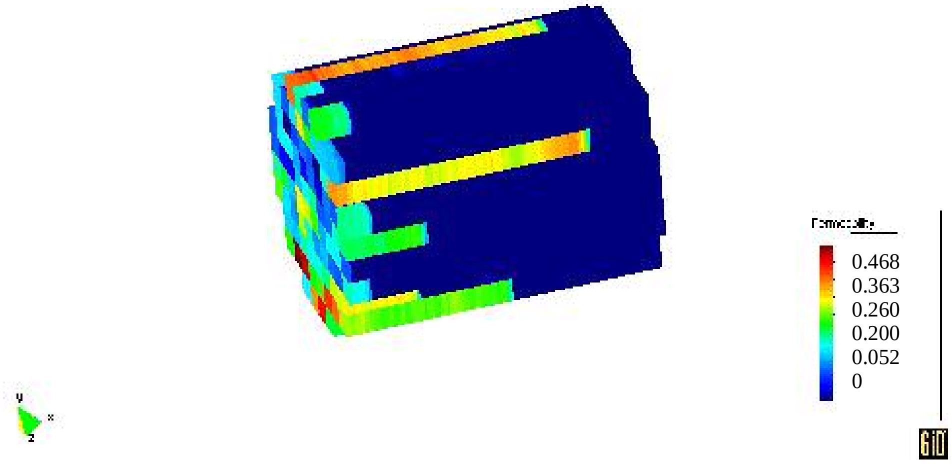

Figure B.3: Permeability (Darcy) distribution after 3 PV of acid injection.

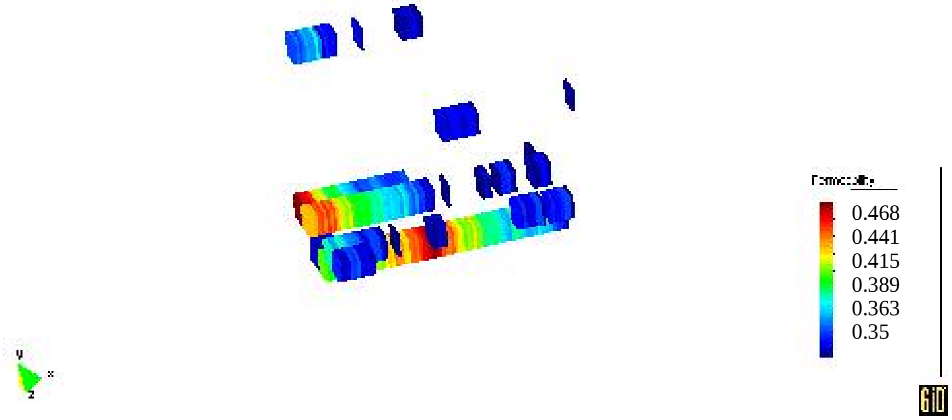

Figure B.4: Permeability (>340md) distribution after 3 PV of acid injection.

APPENDIX C NOMENCLATURE

C	Concentration
$\overline{D}_p$	Mean particle diameter
e	Error limit
$E_{f,i,j}$	Reaction rate constant between acid i and mineral j
h	Lag
k	Permeability
K	Dispersion coefficient of component
L	Core length
MW	Molecular weight
N	Flux (Chapter 2)
N	Number of grid blocks (Chapter 3)
N_{Ac}	Acid capacity number
$N_{a,j}$	The number of acids reacting with mineral j
N_{Da}	Damkohler number
N_m	The number of minerals reacting with acid i
N_p	The number of phases
P	Pressure
P_{out}	Back pressure
$PVbt$	Breakthrough pore volume

q	Injection rate for a grid block
Q	Injection rate
Q_c	Constant injection rate
r	Surface area-specific reaction rate
r_c	Core radius
R	Sources (Section 2.1.3.1)
R	Rate of appearance in the solution (Section 2.1.3.2)
S	Surface area in a unit of bulk volume
S_j^*	Specific surface area
St	Saturation
t	Time
u	Velocity
V	Mineral volume fraction
W	Overall mass in the control volume

α	Reaction order
$\beta_{i,j}$	Dissolving power of mineral *j* by acid *i*
Δ	Prefix for difference
ϕ	Porosity
γ	Gravity ratio
λ	Correlation scale parameter
μ	Viscosity

ρ	Density
ν	Stoichiometric coefficients
Λ	Dimensionless mineral composition
σ	Standard deviation
ω	Mass fraction

Subscripts

D	Dimensionless
i	Component index (Chapter 2)
i	Index of grid block in x direction (Chapter 3)
j	Phase index (Chapter 2)
j	Index of grid block in y direction (Chapter 3)
k	Index of grid block in z direction

Superscripts

0	Original value
n	Time step

REFERENCES

Brannon, D.H., Netters, C.K., and Grimmer, P.J.: "Matrix Acidizing Design and Quality-Control Techniques Prove Successful in Main Pass Area Sandstone," *Journal of Petroleum Technology* (Aug. 1987) 931-942

Bryant, S.L: "An Improved Model of Mud Acid/Sandstone Chemistry," paper SPE 22855 presented at the 1991 Annual Technical Conference and Exhibition of the Society of Petroleum Engineers held in Dallas, TX, Oct. 6-9

Dagpunar, J.: *Principles of Random Variate Generation*, Clarendon Press, Oxiford, 1988

da Motta, E.P, Plavnik, B., Schechter, R.S., and Hill, A.D.: "Accounting for Silica Precipitation in the Design of Sandstone Acidizing," *SPE Production Engineering* (May 1993) 138-144

da Motta, E.P, Plavnik, B., Schechter, R.S., and Hill, A.D.: "The Relationship Between Reservoir Mineralogy and Optimum Sandstone Acid Treatment," paper SPE 23802 presented at the 1992 SPE International Symposium on Formation Damage Control held in Lafayette, LA, Feb. 26-27

Economides, M.J., Hill, A.D. and Ehlig-Economides, C.E.: *Petroleum Production Systems*, Prentice-Hall, Upper Saddle River, NJ, 1994

Gdanski, R.: "Kinetics of Tertiary Reaction of HF on Alumina-Silicates," paper SPE 31076 presented at the 1996 International Symposium on Formation Damage Control held in Lafayette, LA, Feb. 14-15

Gdanski, R.: "Kinetics of Secondary Reaction of HF on Alumina-Silicates," paper SPE 37214 presented at the 1997 International Symposium on Formation Damage Control held in Houston, TX, Feb. 18-21

Hardy, H.H. and Beier, R.A.: *Fractals in Reservoir Engineering,* World Scientific Publishing Co. Pte. Ltd, 1994

Hekim, Y., Fogler, H.S., and McCune, C.C.: "The Radial Movement of Permeability Fronts and Multiple Reaction Zones in Porous Media," *SPE Journal* (Feb. 1982) 99-107

Hill, A.D, Lindsay, D.M., Silberberg, I.H., and Schechter, R.S.: "Theoretical and Experimental Studies of Sandstone Acidizing," *SPE Journal* (Feb. 1981) 30-42

Jennings, J.W.: *Fast Fourier Tranform Simulator*, Personal Communication, The University of Texas – Austin, 2003

Jennings, J.W.: "Geostatistical Analysis of Permeability Data and Modeling of Fluid-Flow Effects om Carbonate Outcrops," *SPE Reservoir Evaluation and Engineering*, v. 3, no. 4, (Aug. 2000) 292-303

Kalfayan, L.J. and Metcalf, A.S.: "Successful Sandstone Acid Design Case Histories: Exception to Conventional Wisdom," paper SPE 63178 presented at the 2000 SPE Annual Technical Conference and Exhibition held in Dallas, TX, Oct. 1-4

Labrid, J.C.: "Thermodynamic and Kinetic Aspects of Argillaceous Sandstone Acidizing," *SPE Journal* (April 1975) 117-128

Lake, L.W.: *Enhanced Oil Recovery*, Prentice Hall, Englewood Cliffs, NJ, 1989

Lake, L.W.: *Mineral Distribution*, Personal Communication, The University of Texas – Austin, 2002

Lindsay, D.M.: "An Experimental Study of Sandstone Acidization," report no. UT76-1 Texas Petroleum Research Committee, The University Of Texas At Austin, July 1976

McLeod, H.O. Jr.: "Matrix Acidizing," *Journal of Petroleum Technology* (Dec. 1984) 2055-2069

Panda, M.N., and Lake, L.W.: "A Physical Model of Cementation and Its Effects on Single-phase Permeability," AAPG Bulletin, v. 79, no. 3, 431- 443, 1995

Quinn, M.A., Lake, L.W., and Schechter, R.S.: "Designing Effective Sandstone Acidizing Treatments Through Geochemical Modeling," *SPE Production & Facilities* (Feb. 2000) 33-41

Schechter, R.S: *Oil Well Stimulation*, Prentice-Hall, Englewood Cliffs, NJ (1992)

Taha, R., Hill, A.D., and Sepehrnoori, K.: "Sandstone Acidizing Design With a Generalized Model," *SPE Production Engineering* (Feb. 1989) 49-55

[a]Thomas, R.L., Nasr-EI-Din, H.A., Mehta, S., Hilab, V., and Lynn, J.D.: "The Impact of HCl to HF Ratio on Hydrated Silica Formation During the Acidizing of a High Temperature Sandstone Gas Reservoir in Saudi Arabia," paper SPE 77370 presented at the 2002 Annual SPE Technical Conference and Exhibition held in San Antonio, TX, Sep. 29 - Oct. 2

[b]Thomas, R.L., Nasr-EI-Din, H.A. Lynn, J.D., Mehta, S., Muhareb, M., Ginest, N.: "Channel vs. Matrix Sandstone Acidizing of a HT/HP Reservoir in Saudi

Arabia," paper SPE 73702 presented at the 2002 SPE International Symposium on Formation Damage Control held in Lafayette, LA, Feb. 20-21

Walsh, M.P., Lake, L.W., and Schechter, R.S.: "A Description of Chemical Precipitation Mechanisms and Their Roles in Formation Damage During Stimulation by Hydrofluoric Acid," *Journal of Petroleum Technology* (Sep. 1982) 2097-2112

Wang, Y., Hill, A.D., and Schechter, R.S.: "The Optimum Injection Rate for Matrix Acidizing of Carbonate Formations," paper SPE 26578 presented at the 1993 SPE Annual Technical Conference and Exhibition held in Houston, TX, Oct. 3-6

Wehunt, C.D., van Arsdale, H., Warner, J.L., and Ali, S.A.: "Laboratory Acidizing of an Eolian Sandstone at 380F," paper SPE 25211 presented at the 1993 SPE International Symposium on Oilfield Chemistry held in New Orleans, LA, Mar. 2-5

Xie, T.: "A Parametric Study of Sandstone Acidizing Using a Fine-Scale Simulator," M.S. Thesis, the University of Texas at Austin, 2004

VITA

Chunlou Li was born in Rongcheng county, Hebei province of China on August 2, 1970, the daughter of Shanwei Li and Guirong Hu. After completing her study at Rongcheng No. 1 High School in 1989, she entered the Petroleum University (Hua Dong). In July 1993, she received the degree of Bachelor of Science in Petroleum Engineering. She was employed as an engineer at Cementing Company of Shengli Oil Field from July 1993 to August 1995. In September 1995, she transferred to Petroleum University (Hua Dong) and worked as a research assistant to July 1998. Since September 1998, she was studying at the Graduate School of the University of Texas at Austin and received the degree of Master of Science in Petroleum Engineering in August 2001. Then she was admitted to the Ph.D program of Department of Petroleum and Geosystem Engineering at the University of Texas at Austin.

Permanent address: Chenyangzhuang, Rongcheng,
Hebei 071700, China

This dissertation was typed by the author.